TECHNISCHE UNIVERSITÄT
MÜNCHEN

Physik-Department E62 - Dense and strange hadronic matter

Abschlussarbeit im Masterstudiengang Kern-, Teilchen- und Astrophysik

Constraints on the anti-deuteron inelastic interaction cross-sections using pp and p–Pb collisions in ALICE at LHC

Lucas Córdova Nyffenegger

2019

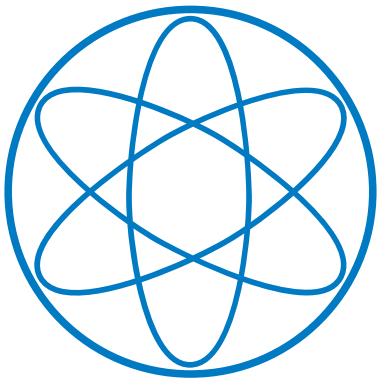

Themensteller:	Prof. Dr. Laura Fabbietti
Betreuer:	Dr. Ivan Vorobyev
Abgabe:	29. November 2019

Abstract

The search for low-energy cosmic anti-deuterons may reveal exotic processes such as dark-matter annihilation. The lack of experimental data at low energies, however, hampers precise predictions of the expected anti-deuteron fluxes near Earth, where both anti-deuteron nuclear inelastic cross-sections with matter and anti-deuteron production cross-sections are known very poorly by today.

In ultra-relativistic collisions of protons and lead ions at the CERN's Large Hadron Collider matter and anti-matter is produced in almost equal abundances, which allows us to study the production cross-sections of (anti-)deuterons with high precision. At the same time, the absorption of produced (anti-)deuterons in the detector material itself can be studied via comparison of raw reconstructed yields of particles and anti-particles.

This thesis presents the studies of the anti-deuteron absorption cross-sections in the ALICE detector material. The raw primary anti-deuteron and deuteron spectra are analysed in proton-proton and in proton-lead collisions at the energies of $\sqrt{s} = 13$ TeV and at $\sqrt{s_{\mathrm{NN}}} = 5.02$ TeV respectively. The resulting reconstructed anti-deuteron to deuteron ratio is compared to the one from detailed ALICE simulations using Geant toolkit for propagation of (anti-)particles through the detector material. First experimental constraints on the anti-deuteron nuclear inelastic cross-sections are extracted in the momentum range $1.4 < p < 4.0$ GeV/c based on the comparison between experimental results and simulations with varied inelastic anti-deuteron cross-sections.

Zusammenfassung

Die Suche nach niederenergetischen kosmischen Antideuteronen kann exotische Prozesse wie die Annihilation der Dunklen Materie aufdecken. Der Mangel an experimentellen Daten bei niedrigen Energien erschwert jedoch genaue Vorhersagen der erwarteten Antideuteron Flüsse in der Nähe der Erde, wo sowohl die inelastischen Antideuteron Wechselwirkungsquerschnitte mit Materie als auch die Antideuteron Erzeugungsquerschnitte bis heute sehr schlecht bekannt sind.
Bei ultrarelativistischen Kollisionen von Protonen und Bleiionen am Large Hadron Collider des CERN werden Materie und Antimaterie in nahezu gleichen Mengen erzeugt, wodurch die Erzeugungsquerschnitte von (Anti-)Deuteronen mit hoher Präzision untersucht werden können. Gleichzeitig kann die Absorption erzeugter (Anti-) Deuteronen im Detektormaterial durch Vergleich der rekonstruierten Rohausbeuten von Teilchen und Antiteilchen untersucht werden.
In dieser Arbeit wird die Untersuchung der Absorptionsquerschnitte von Antideuteron im ALICE-Detektormaterial vorgestellt. Die rohen primären Antideuteron und Deuteron Spektren werden in Proton-Proton- und Proton-Blei-Kollisionen bei Energien von $\sqrt{s} = 13$ TeV und $\sqrt{s_{\mathrm{NN}}} = 5.02$ TeV analysiert. Das Verhältnis von rekonstruierten Antideuteronen zu Deuteronen wird mit denen detaillierter ALICE-Simulationen verglichen, welche das Geant-Toolkit für die Propagation von (Anti-) Teilchen durch den Detektor verwenden. Die experimentellen Grenzen für die inelastischen Querschnitte des Antideuterons werden zum ersten mal im Impulsbereich $1{,}4 < p < 4{,}0$ GeV/c extrahiert und basieren auf dem Vergleich zwischen experimentellen Ergebnissen und Simulationen mit veränderten inelastischen Querschnitten des Antideuterons.

Contents

1. Introduction

Few years after Edwin Hubble established the relation between redshift and distance [1], Fritz Zwicky carried out measurements of the redshift of extragalactic nebulae with unexpected results [2]. In his publication he described that the measured relative velocities of individual galaxies in the Coma cluster show a high difference to the mean velocity of the entire cluster. This dispersion was found to be so high, that in order to keep the Coma system stable, the average mass density in this galaxy cluster would have to be much higher compared to calculations based on observations from luminous matter. In one of the scenarios this can be the consequence of a gravitational force induced by a non luminous *dark matter*.
A similar problem, where significant amount of mass is missing to describe an experimental result, was found by studying rotational curves of galaxies. The latter describes the dependence between the orbit speed of galaxy's stars and their distance from the galactic center. The orbit speed of a gravitationally bound system is expected to increase for rising radii r and, after reaching a maximum, decrease with $\sim 1/\sqrt{r}$ for higher radii. However, measured rotational velocities stay almost constant as the radius increases [3]. One hypothesis to describe this unexpected result could be, that there is more gravity than expected on the basis of the galaxy's observed light.
These two experiments did measurements in different scales, nevertheless, both conclude with same discrepancies between theory and experimental measurements which point towards the same origin. Even in the largest so far known scale, the observable Universe, experiments conclude the same: the measured anisotropy in μK scale of the cosmological microwave background is one prominent evidence [4]. These fluctuations show the density contrasts of the early Universe and the presence of dark matter could explain that these are the sources of the structure of today's Universe [5].
Observations, such as the previously described ones, lead to the conclusion that dark matter contributes to 26.8% of our Universe, whereas "normal" baryonic matter comprises only 4.9% [4]. Understanding the nature of dark matter is one of the major unsolved problems in physics. Experimental research has made many strides in order to discover astronomical dark matter in underground laboratories, in large-area surface telescopes as well as in space. So far, no evidence for a particular signal indicating dark matter detection could be provided.
One method to detect dark matter is the indirect detection, which is based on the search of light (anti-)nuclei cosmic rays from exotic sources. With hypotheses which go beyond the standard model, dark matter can decay or annihilate and form ordinary standard model particles, which result in production of electrons, positrons, (anti-)protons ($\bar{\text{p}}$ and p),

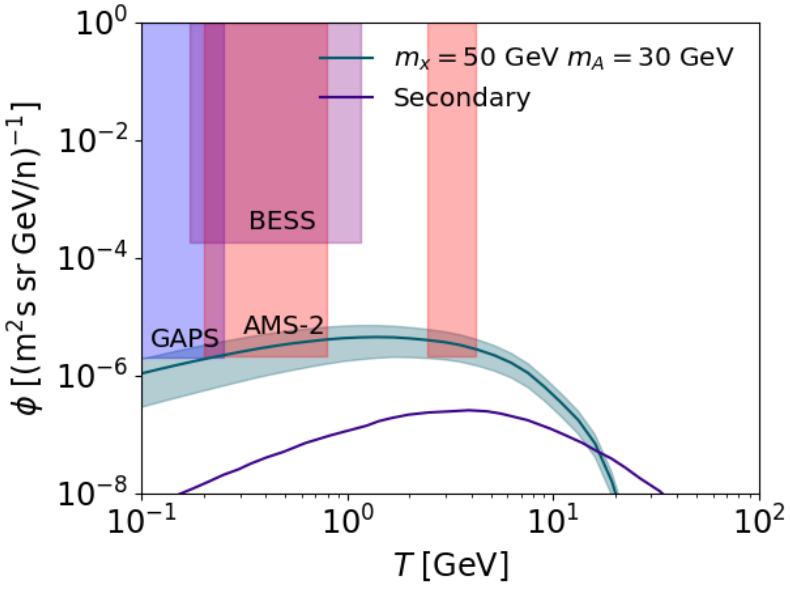

Figure 1.1.: Predicted anti-deuteron fluxes from one model as a function of the kinetic energy [6]. The anti-deuteron limits from BESS are shown, along with the projected sensitivities of AMS-02 after 5 years of operation and GAPS after three 35-day flights. The violet curve represents the background, which is at least two orders of magnitude below the predicted flux in the very low momentum region.

(anti-)deuterons ($\bar{\text{d}}$ and d) and others [7]. These stable (anti-)particles can be detected near Earth, the difficulty with $\bar{\text{p}}$, p and d from exotic sources is to distinguish them from conventional astrophysical production. However, for anti-deuterons the expected signal from possible exotic sources is expected to be significantly higher than the background from cosmic rays [6]. The signal might be within the reach of some experiments, such as GAPS [8] and AMS-02 [9], which are designed, among others, to detect dark matter with the indirect method. Such behaviour can be seen in Figure 1.1, where the predicted flux of anti-deuteron originating from dark matter annihilation or decay exceeds the background by some orders of magnitude, specially at low energies. In order to interpret correctly ongoing and future measurements, the main aspects which need to be known as much as possible are anti-deuteron production and annihilation cross-sections as well as their propagation through the interstellar medium. The propagation term can be well constrained from other astrophysical measurements of primary and secondary cosmic rays. Whereas the production cross-sections of anti-deuterons have been measured at RHIC and LHC energies as discussed below, the anti-deuteron annihilation cross-sections are still very poorly known by today, specially for low kinetic energies.

The constraint of the annihilation cross-section for anti-deuteron is the main topic of this work. As can be seen in Figure 1.2, there are measurements of (anti-)proton and deuteron inelastic cross-sections, also at low momenta. Regarding the cross-section of anti-deuteron,

experimental results for only two different momenta on few materials are available, at $p_{\bar{\mathrm{d}}} = 13.3$ GeV/c [10] and at $p_{\bar{\mathrm{d}}} = 25$ GeV/c [11], as can be seen in Figure 1.3.

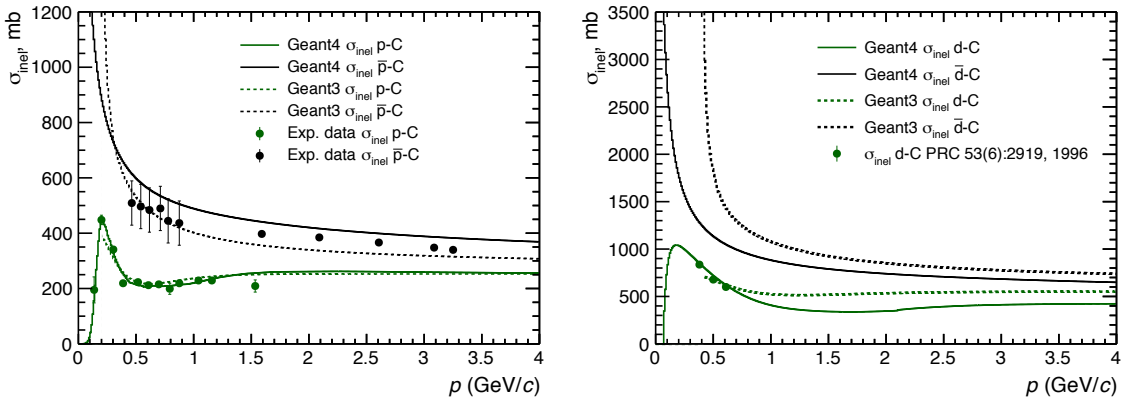

Figure 1.2.: Measured inelastic cross-sections of (anti-)protons (left) and deuterons (right) on a carbon target along with parameterizations used in Geant toolkit. Measurements for anti-deuteron do not exist in this momentum range.

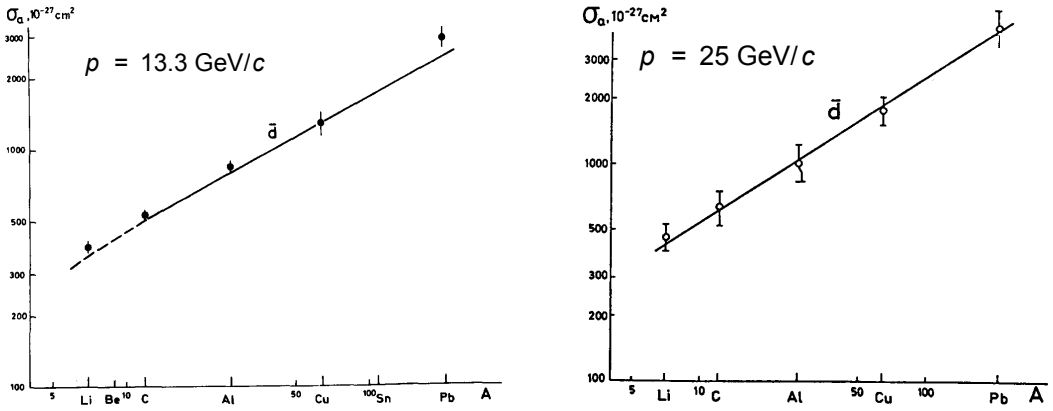

Figure 1.3.: Absorption cross-sections of anti-deuteron for different target materials at $p_{\bar{\mathrm{d}}} = 13.3$ GeV/c (left) [10] and at $p_{\bar{\mathrm{d}}} = 25$ GeV/c (right) [11] .

This thesis presents a method to constraint the anti-deuteron inelastic interaction cross-sections. First, in section 1.1 the production of anti-nuclei in collider experiments is introduced and the main idea of this project is outlined. Chapter 2 gives an overview of the ALICE experimental setup and describes the main components used in this work. The data analysis and evaluation of systematic uncertainties are presented in chapter 3 and chapter 4 respectively. Furthermore, the analysis of Monte Carlo simulated data is described in chapter 5. Finally, the results of this work are presented in chapter 6 followed by the summary and outlook towards future analyses in chapter 7.

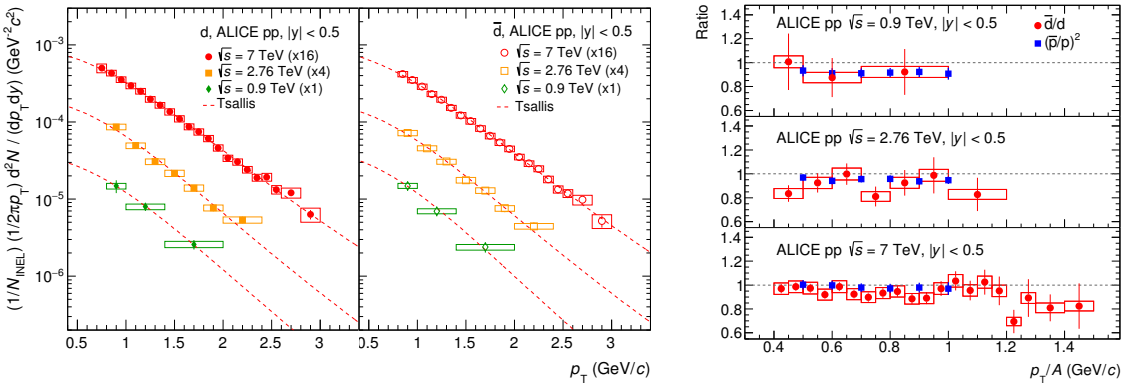

Figure 1.4.: Left: invariant differential yield of deuterons (left panel) and anti-deuterons (right panel) in proton-proton collisions at various energies. Right: primary anti-deuteron to deuteron ratio ($\bar{\mathrm{d}}/\mathrm{d}$) as a function of p_T per nucleon in pp collisions compared with the $(\bar{\mathrm{p}}/\mathrm{p})^2$ ratio [12].

1.1. LHC as anti-matter factory

One fundamental question after discovering the anti-proton in the 1950's [13] was whether anti-nucleons could form anti-nuclei with properties identical to those of their matter partners with opposite charge. The first observations of anti-deuterons in collider experiments [14, 15] were reported in 1965 and confirmed that there must be a process which binds anti-protons and anti-neutrons into anti-deuterons.

Nowadays, in ultrarelativistic proton and heavy-ion collisions, large amount of anti-particles and also anti-nuclei, currently with nucleon number A up to 4, can be produced. So the STAR collaboration reported results on $\bar{\mathrm{d}}$, $\bar{\mathrm{t}}$, $^3\overline{\mathrm{He}}$ and the first observation of $^4\overline{\mathrm{He}}$ measured at RHIC collider at energies between $\sqrt{s_{\mathrm{NN}}} = 7$ and 200 GeV [16, 17]. At higher energies at Large Hadron Collider (LHC), using Pb-Pb, p–Pb and pp collisions with energies from 0.9 TeV up to 7 TeV, the same anti-nuclei have been measured by the ALICE collaboration [12, 18, 19]. At LHC energies, the expected anti-baryon to baryon ratio produced in a collision is unity [20], and dedicated analyses of (anti-)nuclei yields indeed have shown that the primary anti-nuclei to nuclei ratio reaches unity within uncertainties [12, 19]. As can be seen in Figure 1.4 this also true for anti-deuterons.

Due to high production rate of anti-nuclei and an excellent particle identification and tracking capability ALICE is well suited to study the inelastic cross-section of anti-deuterons and other (anti-)nuclei. As mentioned, at LHC energies the anti-deuteron and deuteron yields should be almost equal. Therefore, due to different inelastic cross-sections of deuterons and anti-deuterons, the corresponding reconstructed yields in a collider experiment will be different if the detector effects regarding absorption in the detector material are not corrected for. In this work the raw reconstructed anti-deuteron to deuteron ratio is analysed as a function of momentum, for this the active part of the ALICE detector system is used to

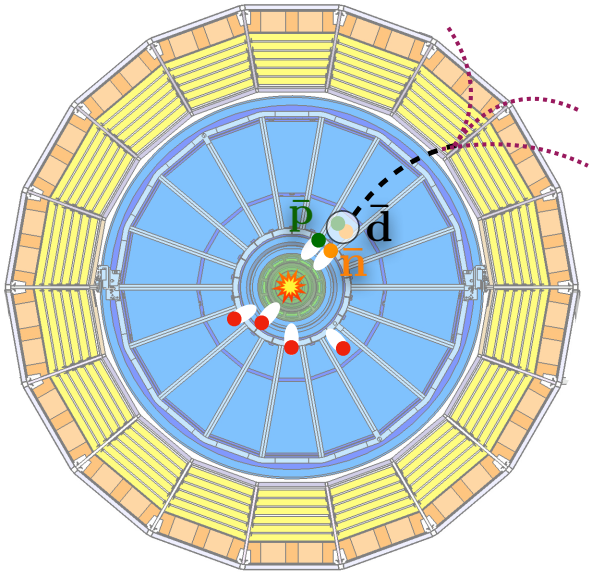

Figure 1.5.: Idea of a project, where an anti-deuteron is created in the collision and is propagated through the detectors. Possible interactions with the detector material leads to a production of secondary particles and to the disappearance of the original track.

track and identify (anti-)deuterons. Such ratios are very sensitive to the detector materials present in central barrel, including the passive parts of the detector i.e. cables, supporting structures and others. The higher the material budget, the more (anti-)deuterons get absorbed. Figure 1.5 shows the cross section of ALICE with a schematic representation of a collision followed by formation of an anti-deuteron which flies through the ALICE detector and annihilates in one of the detector subsystems. The ratios of experimental data are further compared to Monte Carlo simulations, allowing a more detailed investigation of these ratios. Simulations based on different versions of the Geant toolkit for particle propagations are used in this work [21, 22, 23]. The inelastic cross-sections implemented in Geant3 are based on parameterisations of Moiseev's empirical formula [24], whereas Geant4 uses the Glauber approach convoluted with Monte Carlo averaging method [25]. An example of Geant3 and Geant4 parameterisations for (anti-)proton and (anti-)deuteron inelastic cross-sections on carbon is shown in Figure 1.2 together with the available experimental data. This thesis will show that there is a dependence between reconstructed anti-deuteron to deuteron ratio and the inelastic cross-section, which allows extraction of upper and lower limits for the latter. The results can be converted to cross-sections of anti-deuteron on a hypothetical element which has the average mass and atomic number of ALICE detector materials. Since the anti-proton cross-sections are well known and in order to have a benchmark analysis, its inelastic cross-sections are also constrained by using the same method as for anti-deuteron.

2. Experimental Setup

The results of this work are based on data taken with A Large Ion Collider Experiment (ALICE). The current chapter presents the main aspects of the experimental setup and the analysis framework. In section 2.1 the Large Hadron Collider (LHC) at CERN is introduced briefly. Section 2.2 gives an overview of the ALICE detector by focusing on the main sub-detectors used in this work.

2.1. Large Hadron Collider (LHC)

The LHC was build between 1998 and 2008 by the European Organization for Nuclear Research (CERN) near Geneva, Switzerland. With a circumference of 27 km it is the biggest and most powerful particle accelerator that was ever build. As well as the detectors, it is set up in a tunnel approximately 100 m below the Earth's surface and is the last stage of a large system of accelerators.
So far the LHC had two run periods which were used to collide protons (p) and lead (Pb) ions in different combinations at various energies between $\sqrt{s} = 0.9$ and 13 TeV (per nucleon-nucleon pair). A schematic drawing of different pre-stages for the acceleration together with four independent LHC experiments can be seen in Figure 2.1. The pre-stages consist in ionizing protons and Pb ions followed by their pre-acceleration in the Proton Synchrotron (PS) and the Super Proton Synchrotron (SPS). They are fed into the LHC as two counter rotating beam bunches reaching almost the speed of light. Two beams cross each other and the particles collide in the interaction points of different experiments where the products of the collision are tracked and recorded.
This thesis is based on data taken with the ALICE detector, which will be described more closely in the next section.

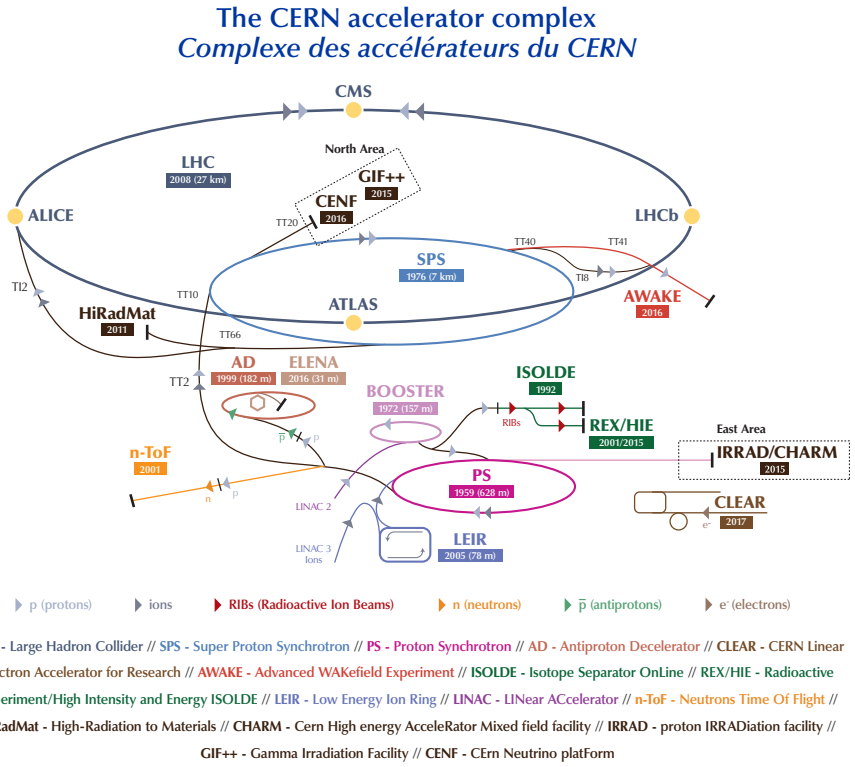

Figure 2.1.: Schematic representation of the accelerator system at CERN [26]

.

2.2. A Large Ion Collider Experiment (ALICE)

ALICE is designed to study heavy-ion collisions at the LHC. Therefore it has excellent particle identification and tracking capabilities down to very low momenta which is also very well suited for (anti-)nuclei studies. It is composed by a set of detectors, that give information about the charge, the velocity and the track, which allow the identification of particles that are coming out of the collisions.

The setup of ALICE during second LHC run can be seen in Figure 2.2. On the right side the muon arm can be seen, it is used for muon analyses and therefore not a part of this thesis. The solenoid magnet, colored in red, provides a homogeneous and low magnetic field of B = 0.5 T parallel to the beam axis and covers all central barrel detectors some of which are used in this work. This thesis focuses on tracking and identification of protons, deuterons and their anti-particles, therefore the analysis is based on the Inner Tracking System (ITS), the Time Projection Chamber (TPC) and the Time of Flight (TOF) detector, all described in more details in the following. The installed materials in the experiment are very important and have a big impact on the outcome of this work. For this reason, even if it is not used here for particle identification, the Transition Radiation Detector (TRD) is also described in subsection 2.2.4 focusing on the material budget.

In a collision, also called event, many particles can be produced what makes it complicated to

reconstruct tracks and events. Within ALICE, track and event reconstruction is performed by using information from ITS and TPC detectors[27]. Starting from large TPC radius, a found track is propagated inwards to the primary vertex, which is the location where particle collisions occur. This procedure is repeated three times, following an inward-outward-inward scheme until finding the final properties of a charged particle track.
Particle identification information for charged particles is provided by the ITS, TPC and TOF detectors. By measuring simultaneously the energy loss of a particle traversing a medium and the particle's momentum, ITS and TPC detectors are able to distinguish between particle species. Similarly, TOF detector provides information about the particle's velocity as a function of momentum, which makes it possible to distinguish between particle species.

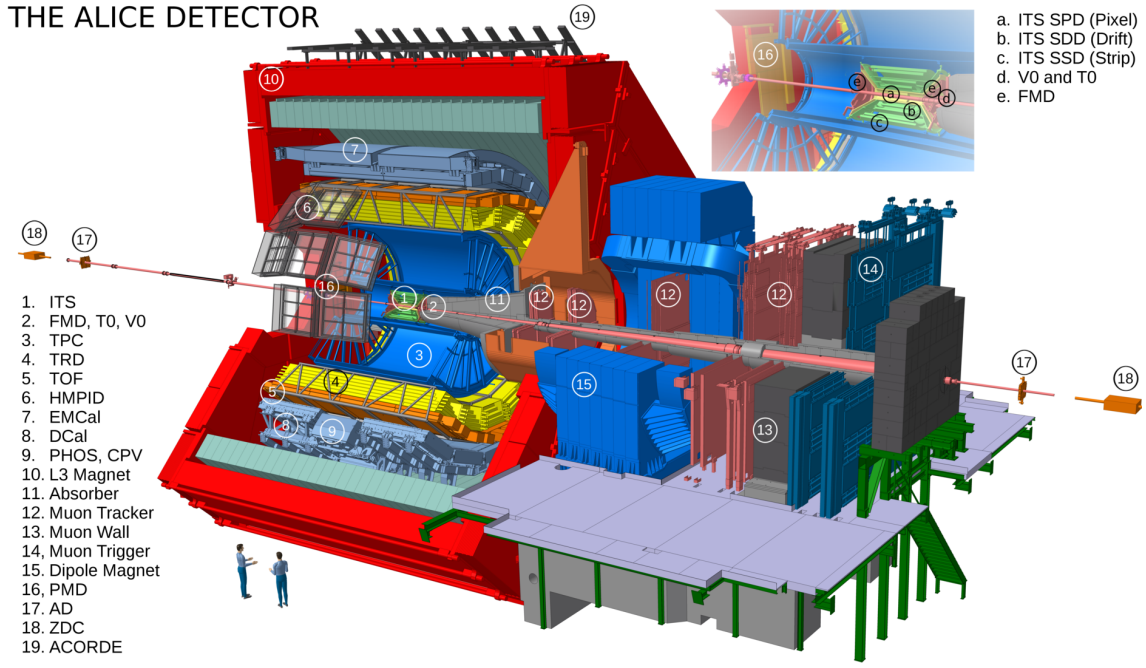

Figure 2.2.: ALICE detector with labeled subsystems [28]

2.2.1. Inner Tracking System (ITS)

The ITS is located in the most central area of the ALICE detector and surrounds coaxially the beam pipe, inside which particle collisions occur. It covers the pseudorapidity range of $|\eta| < 0.9$ and is surrounded by the TPC as can be seen in Figure 2.2. A detailed view of the ITS and its sub-systems can be seen in Figure 2.3 The ITS consists of six cylindrical layers of silicon detectors, counting from the interaction point: two Silicon Pixel Detectors (SPD), two Silicon Drift Detectors (SDD) and two Silicon Strip Detectors (SSD), which are located at radii between 4 and 43 cm respectively. With them, the ITS is able to localize the interaction point with a resolution better than 100 μm, to reconstruct the secondary vertices from hadronic decays, to track and improve the momentum and angle resolution for

particles reconstructed by the TPC and to identify particles down to low momenta using the provided information on the energy loss [29].
The thickness of the silicon detectors and the additional materials, i.e. electronics, cabling and support structure in the active volume of the ITS have been kept to a minimum. This is needed to perform excellent vertex reconstruction because multiple scattering and absorption of particles in materials would lower down not only the resolution of the vertex position but also the momentum resolution. Mass can be assigned by the radiation length X_0, which is a material specific constant and linked to the mean free path of high-energy photons. In Figure 2.4 the radiation lengths for the ITS subsystems are summarized. It can be seen that as a function of the azimuthal angle X_0 fluctuates between 6% and 10%, this is due to contributions with periodical structure such as the carbon supporting frame. The total average radiation length of the ITS sums up to 7.66%.

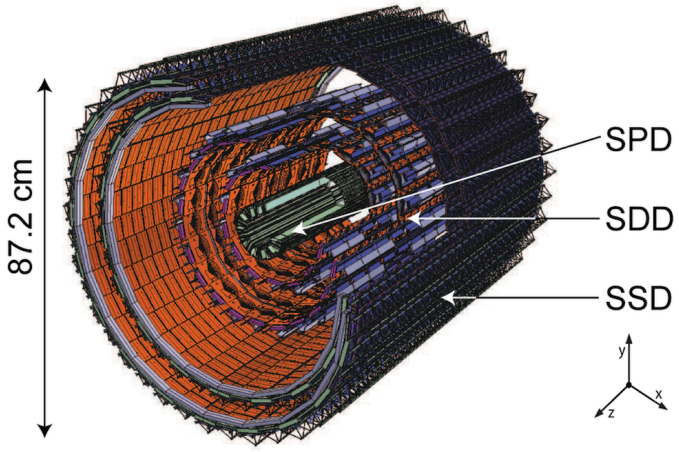

Figure 2.3.: Schematic representation of the ITS detector with its sub-detectors [30].

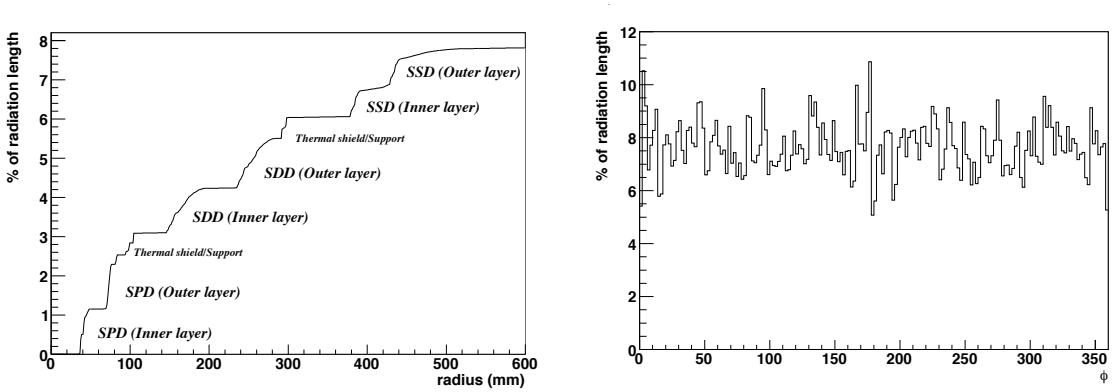

Figure 2.4.: Left: integral of material thickness traversed by a perpendicular track originating at the primary vertex as a function of radius. Right: material thinkness traversed by a perpendicular track originating at the primary vertex as a function of the azimuthal angle [29].

2.2.2. Time Projection Chamber (TPC)

The TPC is the main detector used for tracking and identification of particles in the central barrel. For high energy heavy-ion collisions, where an environment of high densities of charged particles is created, a large-volume TPC is the best choice for tracking and identification of particles.

With an inner radius of 85 cm, an outer radius of around 250 cm and 5 m of length it is the largest detector of the whole setup. In Figure 2.2 the TPC is colored blue and a schematic representation of the field cage can be seen in Figure 2.5. It is a gas detector covering full 2π azimuth acceptance and providing a significant pseudo-rapidity acceptance interval of $|\eta| \leq 0.9$. The 90m^3 detector worked with a gas mixture of Ar-CO_2 in 2016 and 2018, in 2017 it worked with a mixture of Ne-CO_2-N_2. The working principle of this detector consists in ionization of the detector gas by charged particles produced in the collision. Primary ionized electron-ion pairs are separated by an electric field which is parallel to the beam pipe. This electric field is caused by a high electric potential difference between the endplates and the central cathode. The positively charged ions drift towards the cathode and are neutralized. The electrons drift towards the readout chambers located at the endplates of the TPC, where they are amplified and read out in Multi Wire Proportional Chambers (MWPCs). The endplates are segmented into 18 separate readout modules in azimuthal direction. 159 rows in radial direction provide track points and information about the energy loss of the traversing particle. The particle's position in 3-dimensional space can be determined by the drift time (z-coordinate) of the electrons toward the readout, and the two dimensional projection of the track on the readout. By performing a fit, i.e. connecting all points of the particle that traversed the TPC, one obtains the full track in the TPC. Tracks within $|\eta| \leq 0.9$ and traversing all 159 rows, have the highest possible momentum resolution of the TPC, while for a pseudorapidity of $0.9 < |\eta| < 1.5$ the number of track points reduces to around a third [31].

The energy loss in the TPC gas is proportional to the the amount of freed charge along a track segment. The amount of energy lost by a massive particle through ionisation dE per travelled distance dx in a medium, depends only on its charge z and velocity v and can be described by the Bethe-Bloch formula:

$$-\left\langle \frac{dE}{dx} \right\rangle = \frac{4\pi n}{m_e c^2 \beta^2} \cdot \left(\frac{ze^2}{4\pi\varepsilon_0} \right)^2 \left[\ln\left(\frac{2m_e c^2 \beta^2}{I \cdot (1-\beta^2)} \right) - \beta^2 \right] \tag{2.1}$$

In this equation $\beta = v/c$ is the fraction of the velocity v of the particle and speed of light c, ε_0 the electric field constant, e the elementary charge , n the electron density of the material, m_e the mass of the electron and I the average excitation potential of the material. The behaviour as a function of the relevant momentum in this work can be seen in Figure 2.6.

Due to presence of a magnetic field and a resulting Lorentz force, a curvature to the tracks of charged particles is introduced. By measuring this curvature one can calculate the

momentum p of the particle traversing the TPC. By using the dependence $p = m_0\beta\gamma$, β can be replaced by the momentum and a mass dependence is introduced in Equation 2.1, and therefore the energy loss in TPC gas can be used to distinguish different particles.

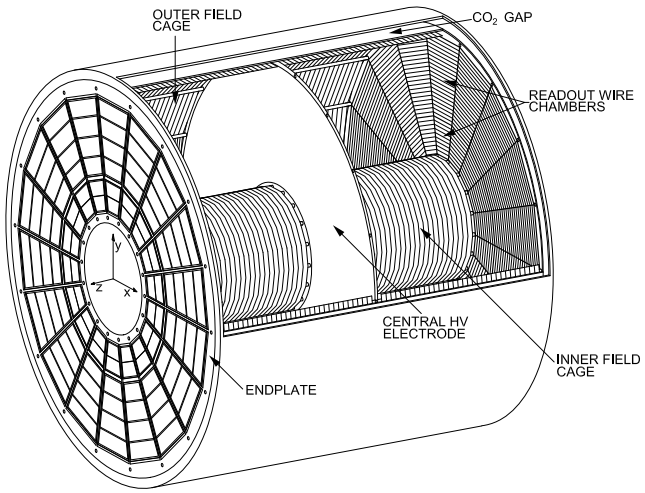

Figure 2.5.: 3D view of the TPC field cage [31]. The high voltage electrode is located at the center of the drift volume. The end- plates with 18 sectors and 36 readout chambers on each end are shown.

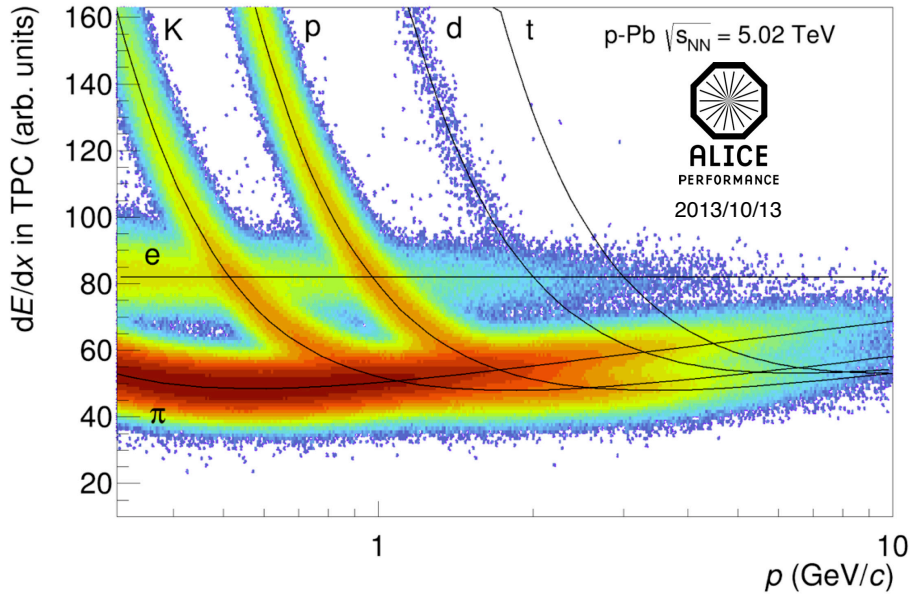

Figure 2.6.: Charged-particle specific energy loss (dE/dx) as a function of momentum, as measured in the TPC in p–Pb collisions. The black lines are the corresponding Bethe-Bloch parametrizations for various particle species.

In Figure 2.6 the energy loss distribution in the TPC gas as a function of particle momentum is shown. The points are distributed around the theoretical parametrization due to limited detector resolution. However, it can be seen that single particles such as proton,

deuterons, electrons, kaons and pions can be identified. At low momenta, up to 1 GeV/c, protons can be identified by using only the TPC, for higher momenta the proton band begins to merge with electron, pion and kaon bands. The deuteron band merges at around 1.5 GeV/c with the electron band. When particle bands merge they can be distinguished by using statistical methods and by complementing the signal with information from other detectors, for example the Time of Flight detector, which is described later in this chapter. Regarding the implemented materials, the main component of the TPC is a Ar-CO_2 gas mixture with fraction 88/12 (Ne-CO_2-N_2 in year 2017 with 90/10/5). The TPC field cage is made out of synthetic fibers and including the TPC gas they have a total average radiation length of 3.5%.

2.2.3. Time of Flight (TOF) Detector

The main task of the Time of Flight detector is, as the name already indicates, to measure the time a particle takes from the interaction point to reach the TOF detector. In Figure 2.2 the TOF is the orange colored cylinder that surrounds ITS, TPC and TRD.
The working principle is based on a large area array of Multigap Resistive Plate Chambers (MRPC). With an acceptance of $|\eta| < 0.9$ and 2π in azimuthal direction, it cylindrically encloses the beam axis at radii between 3.70 and 3.99 m and is divided into 18 supermodules and around 160000 readout pads. In Figure 2.8 one of the 18 TOF supermodules inside the ALICE space frame is shown. To determine the start time for the TOF measurement, other detector systems are needed, namely the T0C and T0A. These are two Cherenkov counters positioned at opposite sides of the interaction point at $-3.28 < \eta < -2.97$ and $4.61 < \eta < 4.92$, respectively. This setup makes it possible for the TOF detector to have a time resolution lower than 100 ps. In order to measure precisely the velocity of a particle, its track length needs to be known, this is done by matching tracks in TPC with TOF hits. With the particle momentum calculated in the TPC and ITS and the simultaneous calculation of β in TOF detector, it is also possible to distinguish different types of particles by using the mass dependence $p = m_0\beta\gamma$. In Figure 2.7 the performance of the TOF detector is illustrated by showing the measured β distribution as a function of momentum. Particles with low mass such as electrons and pions have velocities close to the speed of light with $\beta = v/c \approx 1$ in the whole momentum range. Heavier particles on the other hand have lower velocity for low momenta. Particles with a momentum lower than 0.3 GeV/c curl up before reaching the TOF and do not produce a signal. The bands correspond to different particle species and they are distributed around a mean value due to the detector resolution, whereas the points far away from the bands do not have the same origin, but are rather an effect of mismatched tracks [27].
This detector is the outermost one used for this work, this means that its materials have no influence in the results. However, a large amount of detector material is located between the TPC and TOF detectors, namely the TRD detector.

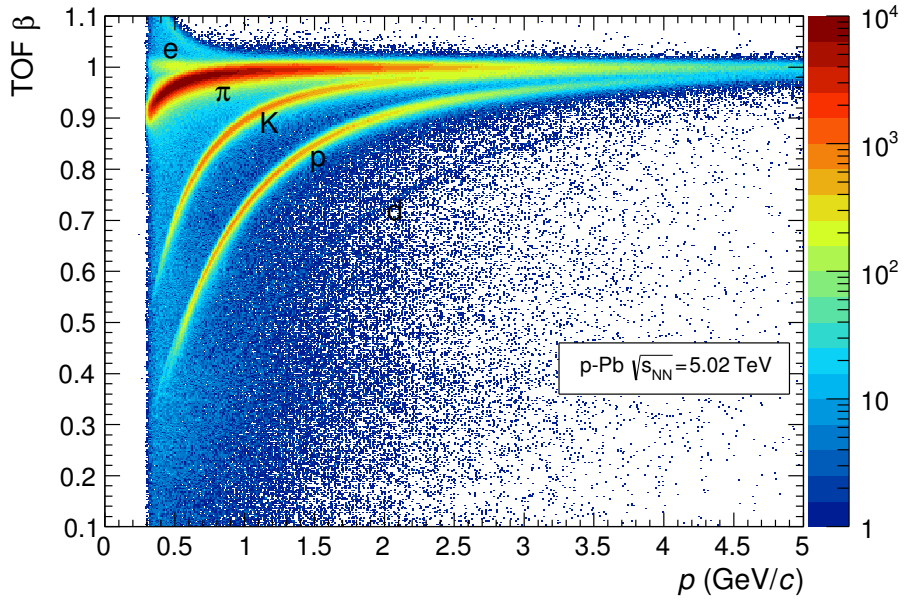

Figure 2.7.: Distribution of β as measured by the TOF detector as a function of momentum in p–Pb interactions [27]

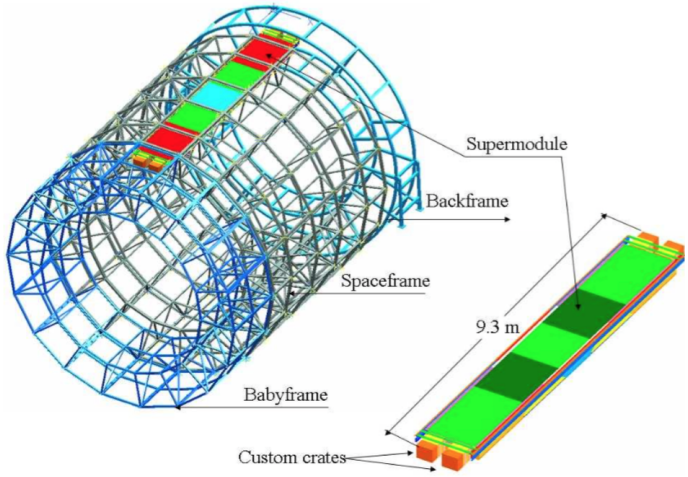

Figure 2.8.: A schematic layout of one of the 18 TOF supermodules inside the ALICE space frame [29].

2.2.4. Transition Radiation Detector (TRD)

To match the segmentation of the TPC in the space frame, the TRD also consists of 18 supermodules, each one with six layers of five drift chambers which are operated with a mixture of Xe (85%) and CO_2 (15%). These supermodules are arranged annularly around the collision point to cover up the total azimuthal angle of the collision. With the help of transition radiation, this detector can identify electrons and reject pions. This is not needed for this work, therefore signals from this detector are not used directly in this analysis. However, laying between the TPC and the TOF detectors, its parts are used as passive material to study absorption in the ALICE detector system. In Figure 2.9 the TRD is

shown inside the ALICE space frame. In addition of its well location, it is the detector with highest radiation length of 24.7% [32]. The main components contributing to this are Xe and CO_2 gas, polypropylene in the radiator and copper for electronics.

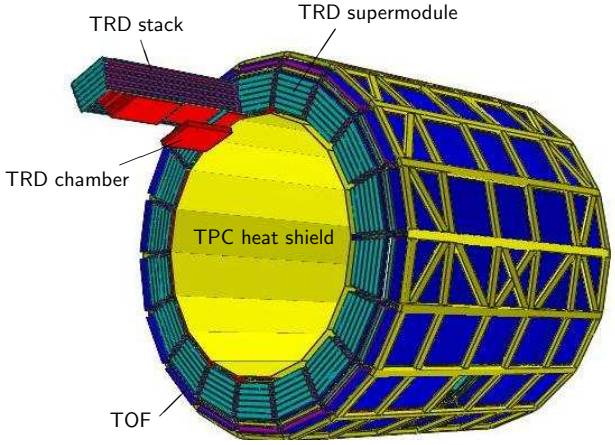

Figure 2.9.: Schematic representation of the TRD in the ALICE space frame [29]. Shown are 18 supermodules each containing 30 readout chambers (red) arranged in five stacks of six layers. One chamber has been displaced for clarity. On the outside the TRD is surrounded by the Time-Of-Flight (TOF) system (dark blue). On the inside the heat shield (yellow) towards the TPC is shown.

2.2.5. Additional passive materials in central barrel

Other parts of the ALICE setup, which are not directly part of the sub-detectors, also do contribute to the total material budget. Additional passive materials in central barrel relevant for this analysis are the ALICE beam pipe and the ALICE space frame between TPC and TOF detectors. The central beam pipe section is the place where the beam bunches cross each other and particles collide. It is a 4 m long beryllium vacuum pipe with an internal diameter of 58 mm and a 0.8 mm thick wall leading to a radiation length of 0.3%. The supporting space frame is a cylindrical grid made out of stainless steel as can be seen in Figure 2.8. Due to this geometry only an average radiation length for a full cylinder was estimated, which has as a result 20% X_0.
The average atomic and mass number of all the materials between the primary vertex and the TOF detector amount to $Z = 11.9$ and $A = 25.5$.

3. Analysis Methods

The goal of this thesis is to find upper and lower limits of the anti-deuteron inelastic interaction cross-section. For this purpose a first analysis, using data from p–Pb collisions at $\sqrt{s_{\mathrm{NN}}} = 5.02$ TeV which was recorded in the second LHC run in 2016, was performed. The analysis was repeated with data from proton-proton (pp) collisions at $\sqrt{s} = 13$ TeV, recorded in the second LHC runs in 2016, 2017 and 2018. By comparing the results, it is possible to test the stability of the analysis and to check whether the results depend on the collision system or not.
Since the procedure to get to the final results is equivalent for both collision systems, the analysis methods are presented by showing examples from pp collisions analysis. To compare and discuss the analyses and its results, also some intermediate results from both collision systems are presented. An important requirement for this work is to identify a very pure sample of protons, deuterons and its corresponding anti-particles as a function of the momentum p. In this chapter it is described how this is accomplished and it concludes with the discussion of raw primary particle ratios.

3.1. Event and track selection

Collected data also contain events which are not necessary suitable for analysis. In order to exclude them, so called event selections were implemented.
The events are first selected according to the used trigger. In this work, two different types of triggers were used, the minimum-bias (MB) trigger for p–Pb collisions and the high multiplicity (HM) trigger for pp collisions. The MB trigger corresponds to a simultaneous signal in two V0 scintillators covering the pseudorapidity ranges of $2.8 < \eta < 5.1$ (V0A) and $-3.7 < \eta < -1.7$ (V0C). The HM trigger additionally requires that the number of hits in V0A and V0C are above a certain threshold. The average multiplicity is $\sim$4 times higher in HM data with respect to MB data and therefore largely increases the statistics. In order to further clean this data sample from remaining contamination, additional cuts are applied. Information from V0 and SPD detectors is used to reject background events such as beam-gas interactions or collisions with de-bunched protons. Only events with a primary vertex position within $\pm$10 cm from the geometrical centre of the detector along the beam axis, and at least 1 track contributing to vertex reconstruction, as discussed in section 2.2, are used for the analysis.
A total number of 302×10^6 MB events from p–Pb collisions and 864×10^6 HM events from

pp collisions are selected in this procedure .
After an event has been selected, cuts on tracks are implemented to filter tracks originating from primary event vertex and with a certain criteria for the reconstruction quality. The used cuts are summarised in Table 3.1. Tracking within the full acceptance of all used central barrel detectors was ensured by selecting tracks within a pseudorapidity range of $|\eta| < 0.8$. A high amount of particles, which do not come from the primary vertex can be excluded by performing a selection on the distance of closest approach (DCA) variable. It is the closest distance to the interaction vertex that the extrapolation of a reconstructed track has. DCA selection criteria are chosen to be relatively tight in order to suppress contribution from secondary particles which have wider DCA distributions than primary particles.

Event cut Parameter	**Value**
Number of contributors to the primary vertex	≥ 1
Vertex in $\|z\|$ direction	≤ 10 cm
Track cut Parameter	
$\|\eta\|$	≤ 0.8
Number of TPC clusters	≥ 70
Number of ITS clusters	≥ 2
χ^2 of track fit per TPC cluster	≤ 4
χ^2 of track fit per ITS cluster	≤ 36
Hit in SPD detector	required
$\|\mathrm{DCA}_{xy}\|$	≤ 0.1 cm
$\|\mathrm{DCA}_{z}\|$	≤ 0.2 cm

Table 3.1.: Event and Track cut parameters and their respective values.

3.2. Particle Identification (PID)

As discussed in section 2.2, all described detectors allow particle identification. The TPC measures the energy loss of a particle which follows Equation 2.1 and the simultaneous measurement of the track momentum allows PID. The theoretical values of $\left\langle \frac{dE}{dx} \right\rangle$ for the TPC detector can be determined by a parametrization of the Bethe Bloch formula. To distinguish different particles species, the numbers of sigma (nσ) method is used. It is a statistical method where a cut on the relative difference nσ of the energy loss value is employed in terms of numbers of standard deviations from the mean $\left\langle \frac{dE}{dx} \right\rangle$ normalised by the PID resolution of the detector (σ).

$$\mathrm{n}\sigma = \frac{\left(\frac{dE}{dx}\right)_{\mathrm{measured}} - \left\langle \frac{dE}{dx} \right\rangle_{\mathrm{theo}}}{\sigma} \tag{3.1}$$

Figure 3.1 shows one example for pions in a high transverse momentum (p_T) interval to illustrate the separation power. The distribution is fit with a convolution of Gaussian functions. Thus particles can be identified by cutting on the nσ variable.
Since the Bethe Bloch formula depends on the momentum, nσ needs to be calculated for all momentum bins. As discussed in subsection 2.2.2, for low momenta the signal in the TPC is well separated for each particle species. While for higher momenta, as it is the case in Figure 3.1, the distributions overlap and one particle specie contaminates the purity of an other particle specie.

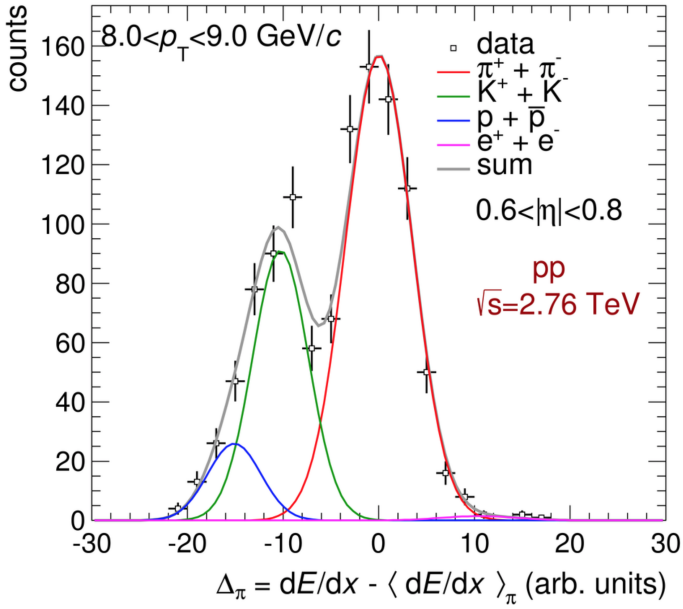

Figure 3.1.: Ionization energy loss (dE/dx) distributions in the TPC in pp collisions at $\sqrt{s_{NN}} = 2.76$ TeV [27]. The lines represent Gaussian fits as described in the text.

The TOF detector is also able to perform a PID and it uses the same method to extract the nσ variable, but using the β distribution instead of the specific energy loss

$$\mathrm{n}\sigma = \frac{(\beta)_{\mathrm{measured}} - \langle\beta\rangle_{\mathrm{theo}}}{\sigma} \tag{3.2}$$

In this analysis, the used method to identify a particle depends on its momentum. See in Table 3.2 a summary of the implemented PID method for different particle species and momentum ranges. All further described requirements are the same between the corresponding particles and antiparticles.
The TPC is used to identify particles in the whole momentum range with $|\mathrm{TPCn}\sigma_{\mathrm{p,d}}| < 3$. At low momenta, the TPC is able to identify particles on a track by track basis using the nσ method. Up to which momentum the TPC is capable of PID depends on the particles mass and charge. In this work a TPC only PID was performed for protons (deuterons) below

$p = 0.7$ GeV/c ($p = 1.4$ GeV/c). Above $p = 2.5$ GeV/c ($p = 1.4$ GeV/c), a hit on the TOF detector is requires for proton (deuteron) candidates. A detailed description on how the particle yields are extracted in this momentum range by using fits to TOF m^2 distributions, is explained in section 3.3. In the momentum range $0.7 < p < 2.5$ GeV/c, protons are identified by additionally requiring $|\mathrm{TOFn}\sigma_\mathrm{p}| < 3$, since the fit to the TOF m^2 distribution is not able to describe the data in all details.

To identify (anti-)deuterons, an additional selection based on ITS PID information is applied to all tracks below $p = 1.4$ GeV/c. The purpose of this cut is to reject an additional contribution to the $\mathrm{ITSn}\sigma_\mathrm{d}$ distribution with high nσ values, which is present at low momentum for deuterons, but not for anti-deuterons as can be seen in Figure 3.2. A requirement of $\mathrm{ITSn}\sigma_\mathrm{d} > -2.0$ is applied to both, deuteron and to anti-deuteron candidates, up to this momentum range.

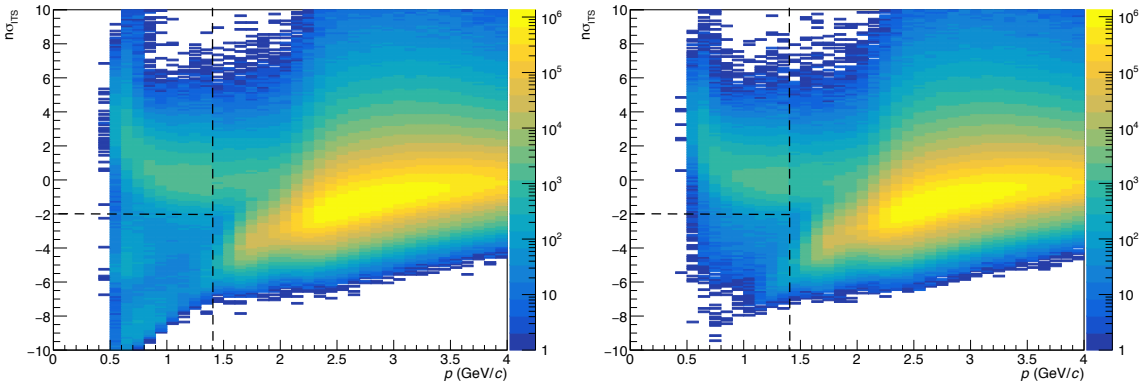

Figure 3.2.: ITSnσ distributions as a function of the momentum after TPC and TOF PID selection of deuterons (right) and anti-deuterons (right) candidates. Vertical dashed lines indicate the momentum up to which the ITS PID selection is applied.

Particle	**PID Requirement**	p **Range** [GeV/c]
(anti-)proton	$\lvert\mathrm{TPCn}\sigma_\mathrm{p}\rvert < 3$	$[0.2; \infty]$
	$\lvert\mathrm{TOFn}\sigma_\mathrm{p}\rvert < 3$	$[0.7; 2.5]$
	Matched TOF hit	$[2.5; \infty]$
(anti-)deuteron	$\lvert\mathrm{TPCn}\sigma_\mathrm{d}\rvert < 3$	$[0.2; \infty]$
	$\mathrm{ITSn}\sigma_\mathrm{d} > -2$	$[0.2; 1.4]$
	Matched TOF hit	$[1.4; \infty]$

Table 3.2.: PID cut parameters and their respective values.

3.3. Raw signal extraction

After the event, track and PID selection were applied, the (anti-)particle p spectra are obtained, however with impurities from other particles. In order to extract the most pure

sample of the desired particle, a further analysis of the spectra is needed.
In this thesis the terminology "low momentum range" is used when referring to the p range where no TOF PID is performed and "high momentum range" when the TOF detector is used to identify particles. Whether to perform a TOF PID or not is crucial for this work and will be discussed at the end of this chapter.

3.3.1. Low momentum range

In this momentum range raw (anti-)particle yields are extracted by the raw counts after the PID selection. Thus no further analysis needs to be performed here. The ranges are:

- $0.3 < p < 0.7$ GeV/c for (anti-)protons using PID information from the TPC detector only
- $0.5 < p < 1.4$ GeV/c for (anti-)deuterons using PID information from the ITS and TPC detectors.

3.3.2. High momentum range

As already mentioned, in the high momentum range particles are identified by additionally using the TOF detector. The procedure to extract the raw signal in this momentum range can be summarised as follow:

- (anti-)protons:
  - $0.7 < p < 2.5$ GeV/c by using PID information from the TPC and the TOF detectors. The purity is evaluated afterwards and the raw spectra are corrected in this "intermediate" range as described in subsection 3.3.3.
  - $2.5 < p < 4.0$ GeV/c tracks are required to have a matched TOF hit, and the raw yields are extracted with the fits to TOF m^2 distributions as described below
- (anti-)deuterons:
  - $1.4 < p < 4.0$ GeV/c tracks are required to have a matched TOF hit, and the raw yields are extracted with the fits to TOF m^2 distributions as described below

The squared mass m^2 of each particle can be calculated by combining information obtained by the TPC and TOF detectors using Equation 3.3. In this equation p and L are the track's momentum at the interaction vertex and the track's length correspondingly. t_{TOF} is the track's time of flight measured by the TOF detector.

$$m^2_{\mathrm{TOF}} = p^2 \left(\left(\frac{t_{\mathrm{TOF}}}{L} \right)^2 - \frac{1}{c^2} \right) \tag{3.3}$$

The raw signal can now be extracted as a function of the momentum by fitting the TOF m^2

distribution in each p bin. An example of a fit to TOF m^2 distributions of protons and deuterons is shown in Figure 3.3 and the collection of all fits is in Appendix A.

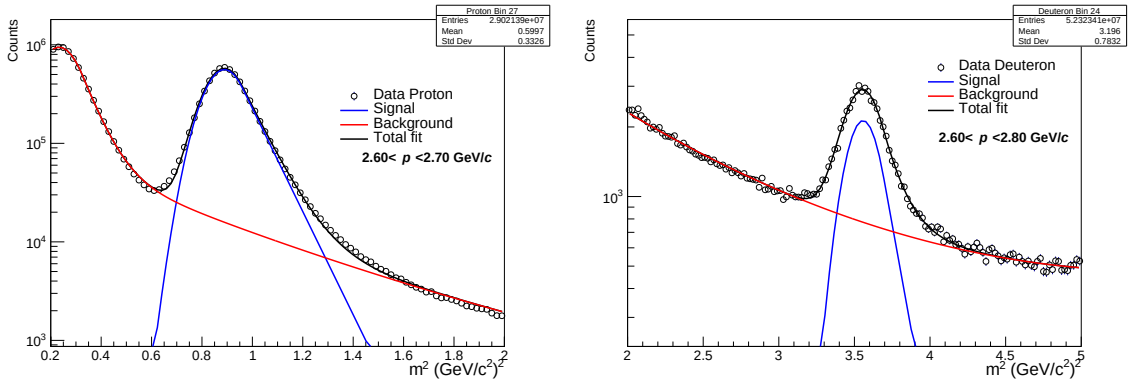

(a) Protons **(b)** Deuterons

Figure 3.3.: TOF m^2 distributions for a selected momentum interval from pp collisions. The blue line represents a fit of a Gaussian function plus an exponential tail, the red line the fit of the background, and the black line is the sum of signal and background.

This thesis follows the procedure described in [33], where the signal $s(m^2)$ is fitted according to Equation 3.4, using a Gaussian function with an exponential tail towards higher masses for the signal that reflects the TOF detector time response.

$$s(m^2) = I\hat{s}(m^2) \tag{3.4}$$

where I is the integral of the function and $\hat{s}(m^2)$ is the corresponding normalised function defined as

$$\hat{s}(m^2) = \begin{cases} c_0 \exp\left(-\frac{(m^2-\mu)^2}{2\sigma^2}\right), & m^2 \leq \mu + \tau\sigma \\ c_0 \exp\left[-\left(m^2 - \mu - \frac{\tau}{2}\sigma\right)\frac{\tau}{\sigma}\right], & m^2 > \mu + \tau\sigma \end{cases} \tag{3.5}$$

Here μ and σ correspond to the signal mean and width values, and τ is a parameter needed to describe the exponential tail of TOF response. The normalisation parameter c_0 is given by

$$c_0 = \frac{1}{\sqrt{\frac{\pi}{2}}[\sigma + \sigma erf\left(\frac{\tau}{2}\right)] + \frac{\sigma}{\tau}\exp\left(-\frac{\tau^2}{2}\right)} \tag{3.6}$$

To describe the background $b(m^2)$, the distribution was fitted with the exponential function in Equation 3.7.

$$b(m^2) = \exp(p_0 + p_1 m^2 + p_2 m^4) \tag{3.7}$$

This function accounts for those tracks erroneously associated to a TOF hit and for the tail of particles with lower masses. For (anti-)protons, an additional function for kaon peak (according to Equation 3.4), visible at $m^2 \approx 0.25$ $(\mathrm{GeV}/c^2)^2$, is added to the background function. The (anti-)particle yield and its statistical error are both returned by the fit and can be used directly as raw signal.

3.3.3. Intermediate momentum range for (anti-)protons

In this momentum range, $0.7 < p < 2.5$ GeV/c, the signal is not extracted by fitting the TOF m^2 distribution, but by applying a TOFnσ cut. This is due to the fact that the signal function for the TOF m^2 can not describe the (anti-)proton peak in all details, with a disagreement becoming worse in lower momentum bins, specially for anti-protons where an additional contribution is visible at $m^2 \approx 0.7$ (GeV/c^2)^2 as can be seen in Figure 3.4. By looking at simulations, it was studied whether this behaviour comes from contamination from other particles or from secondary (anti-)protons. The result indicate that contamination and secondaries can be excluded as source. Further investigations are needed to check detector effects and reconstruction quality.
In this intermediate momentum range $0.7 < p < 2.5$ GeV/c, the raw (anti-)proton yield is extracted by additionally applying a PID selection of $|\text{TOFn}\sigma_\text{p}| < 3$. This cuts also the shoulder in the anti-proton m^2 distribution away.
The purity of the (anti-)proton sample selected by this method is estimated by fitting the TOF m^2 distribution only using the background function, presented in Equation 3.7, outside of the peak region between (0.2,0.6) and (1.8,2.0) (GeV/c^2)^2. An example for one momentum bin can be seen for both proton and anti-proton in Figure 3.4. The purity is then calculated by evaluating a $\pm 3\sigma$ range around the signal peak and stays above 96% in this momentum region.

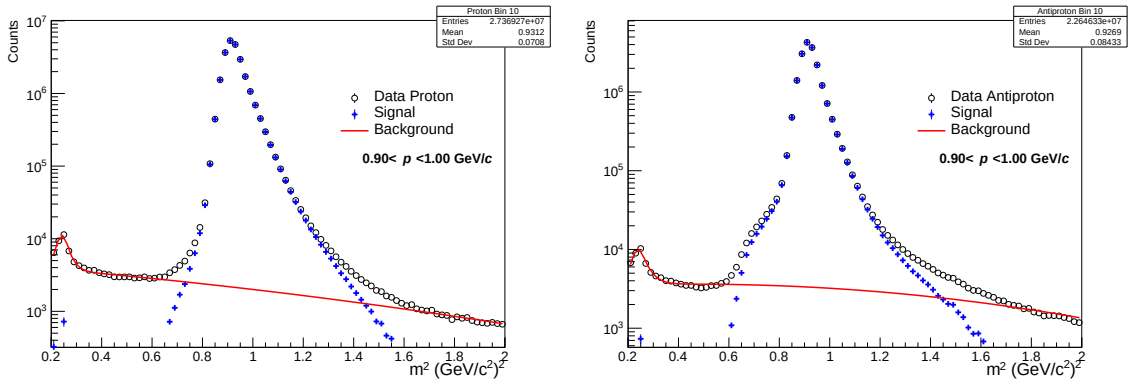

(a) Protons **(b)** Anti-protons

Figure 3.4.: Fits to TOF m^2 distributions in momentum bin $0.9 < p < 1.0$ GeV/c. The fit is performed by using only the background function in red.

3.3.4. Raw (anti-)particle spectra

All previously presented procedures were implemented in both of the analyzed collision systems: p–Pb collisions at $\sqrt{s_\text{NN}} = 5.02$ TeV and pp collisions at $\sqrt{s} = 13$ TeV. After going through all of the steps, a first quantitative comparison of the analyses can be done. In Figure 3.5 the raw momentum spectrum of each analysed particle specie and collision system

is shown. With respect to the particle species there are ~ 700 times more (anti-)protons produced and identified than (anti-)deuterons in both collision systems. By comparing the collision systems, it can be seen that the extracted raw (anti-)particles yields in pp analysis is higher by a factor ~ 4.6 with respect to the p–Pb analysis. This is not only due to the higher number of events but also due to a higher multiplicity per event. Finally, the comparison of anti-particles to particles makes clear that more particles are identified in both analyses. Higher inelastic interaction cross-sections for anti-particles than for particles and the consequent annihilation process of them in the detector material and a lower amount of secondary anti-particles than particles contribute to the origin of this behaviour. An interesting characteristic of these figures is the step for (anti-)protons ((anti-)deuterons) visible at $p = 0.7$ GeV/c ($p = 1.4$ GeV/c), which indicates a loss of (anti-)particles when performing TOF PID. The first source of it is the limited efficiency of TOF detector which also includes miss-matched TPC to TOF tracks. The second one is a higher absorption (anti-)particles due to the fact that they need to cross the TRD detector ($X_0 \sim 24.7\%$) in order to reach the TOF detector. This means that particles and anti-particles are sensitive to traversing more material. As mentioned, these spectra contain secondary (anti-)particles, which need to be corrected for. This procedure is described in the next section.

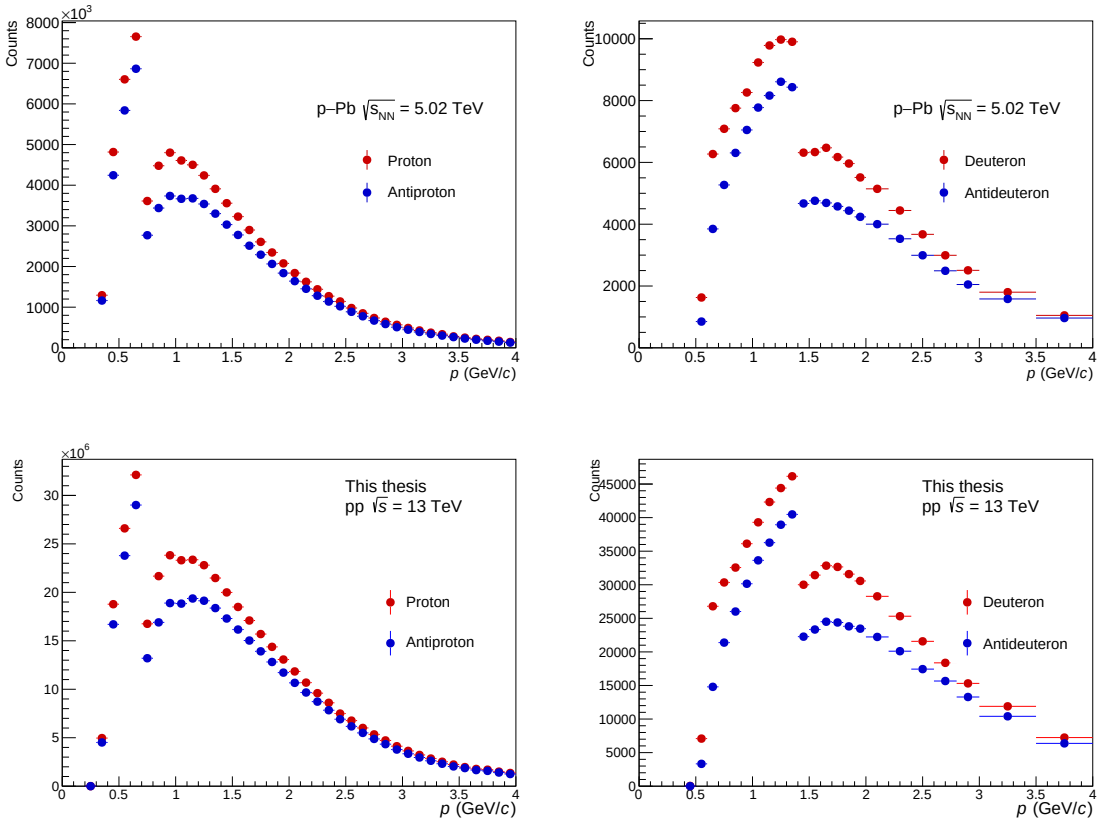

Figure 3.5.: Raw (anti-)proton (left) and (anti-)deuteron (right) spectra from p–Pb (top) and pp collisions (bottom). The dramatic decrease of (anti-)protons ((anti-)deuterons) at $p \sim 0.7$ GeV/c ($p \sim 1.4$ GeV/c) is due to additional detector material (TRD). Corrections for secondary (anti-)particles are yet not applied.

3.4. Correction for secondary (anti-)particles

In the previous sections it is outlined, step by step, how to identify protons, deuterons and its corresponding antiparticle. However for this analysis, it is important to have not only a very pure sample of (anti-)particle species but also select particles originating only from the primary vertex. For this, the raw spectra need to be corrected for contamination due to secondary (anti-)particles originating from weak decays or spallation processes in the detector material.

In section 3.1 it was described how contribution from secondary (anti-)particles is suppressed, using a tight cut on the $\mathrm{DCA}_{xy,z}$ variables. This is improved by analysing the DCA_{xy} distributions as a function of the (anti-)particle momenta. It is possible to distinguish whether a particle is originated in the primary vertex or not by looking at the singular shape of the DCA_{xy} distribution. The difficulty is, that in experimental data this distributions can not simply be separated, what introduces the help of a Monte Carlo (MC) simulation. In chapter 5 MC datasets are described in more details.

It must be noted that almost every LHC run period has a corresponding MC simulation

production, which is the case for the used p–Pb collisions in this work, but not for the used HM pp collisions. Nevertheless, in the pp analysis secondaries where rejected by using the same MC production as for the p–Pb analysis.
The strategy to reject secondary particles from the data sample, is to fit the sum of primary and secondary (anti-)particle's DCA_{xy} templates distributions obtained from MC data to the experimental data in momentum bins. This is done by using the TFractionFitter class of ROOT. In order to obtain a more reliable fit, the DCA_{xy} cut is opened to $|\mathrm{DCA}_{xy}| < 1.0$ cm (both in MC and in experimental data). The fraction of primary (anti-)particles is extracted as the ratio of primary (anti-)particles over the sum but only in the region $|\mathrm{DCA}_{xy}| < 0.1$cm, where the actual cut is applied. This results as fractions of primary particles as a function of the momentum, which can be used to multiply the raw momentum spectra to reject contribution from secondary particles.

The **(anti-)proton** DCA_{xy} distributions are fit with three templates from MC simulations: primaries, secondaries from weak decay and secondaries from material. Figure 3.6 shows one example of such a template fit and the resulting purity of (anti-)proton as a function of the momentum. The purity stays high for all momenta, due to the previously discussed tight DCA_{xy} cuts. It can be seen that the anti-proton purity is slightly higher at low momenta, this is due to the fact that secondary protons from spallation processes are more probable than anti-protons.

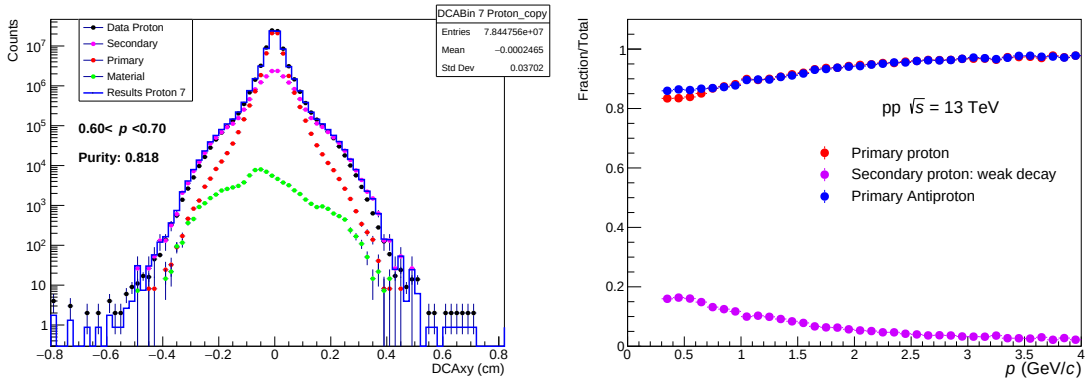

Figure 3.6.: DCA_{xy} distribution of protons (left) in momentum interval $0.6 < p < 0.7$ GeV/c along with MC templates for primaries, secondaries from material and secondaries from weak decays which are fitted to the data. Resulting fraction of primary (anti-)protons (right) and fraction of secondary protons from weak decay as a function of momentum in experimental data.

Anti-deuterons are not corrected for secondary anti-particles, their fraction of secondaries is assumed to be zero [12]. The **deuteron** DCA_{xy} distributions are fit with only two templates. The templates from secondaries from material are taken from MC simulations, whereas the primary templates are taken from anti-deuteron experimental data, since they

are assumed to be pure primaries. One example of a deuteron template fit and the resulting purity as a function of track momentum is shown in Figure 3.7 and all template fits are listed in Appendix B. It can be seen that the purity is low for low momenta, but increases monotonically until reaching unity at $p \approx 1.4$ GeV/c

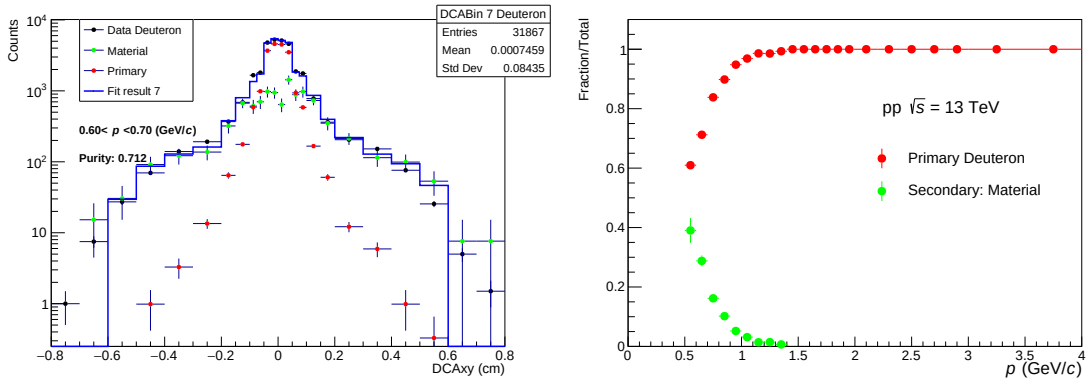

Figure 3.7.: DCA$_{xy}$ distribution of deuterons (left) in momentum interval $0.6 < p < 0.7$ GeV/c along with one MC template for secondaries from material and one template from experimental anti-deuteron data for primaries. Resulting fraction of primary deuterons (right) as a function of momentum in experimental data.

3.5. Primary antiparticle to particle ratios

After going through all the previously described procedures, the (anti-)particle spectra are composed only by the desired primary (anti-)particles species, namely raw primary protons, deuterons and the corresponding anti-particles. Here must be noted, that these spectra were not corrected for any detector effect. These raw spectra are used to build the raw anti-particles to particles yield ratios. The ratios for both p–Pb and pp collisions are shown in Figure 3.8 as a function of the momentum at the vertex. To know the momentum at which annihilation occurs, this results need to be corrected for energy loss, which is described in section 6.2.

The ratios show clear deviations from unity, indicating a higher loss of primary anti-particles in the detector material than particles. At low momentum, absorption of (anti-)particles is possible in the beam pipe ($X_0 \sim 0.3\%$) as well as in ITS ($X_0 \sim 8.0\%$) and TPC ($X_0 \sim 4.0\%$) detectors. The step, visible at $p = 0.7$ GeV/c for $\bar{\mathrm{p}}$/p ratio and at $p = 1.4$ GeV/c for $\bar{\mathrm{d}}$/d ratio is the transition to the momentum region where TOF PID is used. It is the proof that anti-particles are affected more strongly when traversing more material such as the TRD ($X_0 \sim 24.7\%$).

The figures also show that the analyses in different collision systems are in good agreement in almost all bins, giving a first indication that the work has good stability and also that the results are not dependent on the collision system, but rather on the detector material present in central barrel.

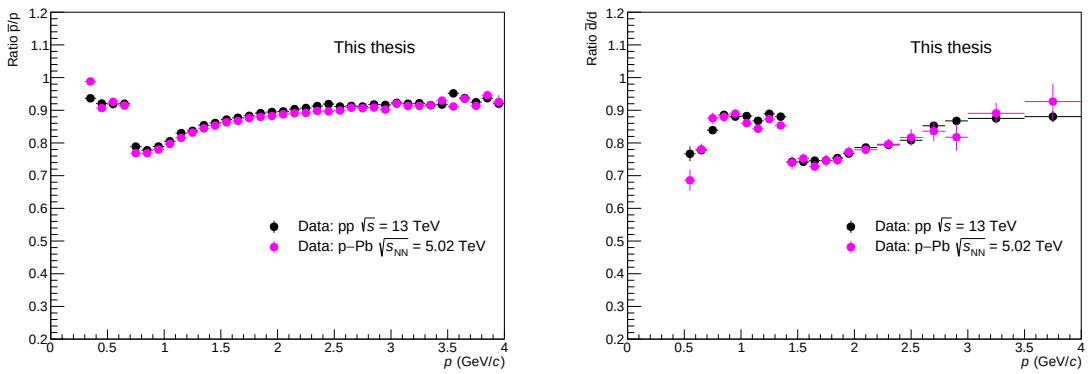

Figure 3.8.: Raw primary anti-proton to proton (left) and anti-deuteron to deuteron (right) ratios as a function of momentum. For comparison, results of both collision systems are on the same plot. Only statistical uncertainties are shown.

4. Systematic uncertainties

Systematic uncertainties are evaluated to test the stability of the obtained results and to evaluate possible bias introduced by the analysis procedure described in chapter 3. The sources of systematic uncertainties in this thesis are mainly tracking precision, particle identification and corrections due to secondary particles. In this section it is described how this uncertainties were estimated concluding with a discussion of the results. Section 4.5 introduces a global uncertainty related to the primordial ratio of anti-particles to particles.

4.1. Tracking

In order to test the stability of the results against tracking, the analysis was inspected in dependence of track selection criteria, magnetic field polarity, ITS-TPC matching and TPC-TOF matching.
To estimate the impact due to track selection, the analysis has been redone by using 20 different track cut settings, which have been randomly composed from 3 possible variations for each cut variable according to Table 4.1. With “loose” cuts the number of tracks rises but the track quality falls and vice versa for “tight” cuts the number of tracks goes down but the track quality rises. The uncertainty has been evaluated by calculation of the RMS value of the distribution of this 20 resulting ratios.
Positive and negative charged particles can be affected by different reconstruction efficiencies due to asymmetric coverage of the central barrel detectors. Therefore, the analysis was repeated by using two data sets with different polarities and the relative difference in the results was taken as uncertainty.
The uncertainty from ITS-TPC and TPC-TOF matching is estimated in both cases by the matching efficiency, which is the number of tracks with TPC-ITS (hit on TOF detector) requirements divided by the number of tracks with only TPC requirement. The TPC-TOF matching efficiency was estimated with charged pions, in order to (anti-)particle absorption in the TRD material. The relative difference in matching efficiency between particles and anti-particles is used as uncertainty.
The before mentioned procedures have been repeated with MC data. In each uncertainty source, only the relative difference, between the experimental data and the MC results have been taken as systematic uncertainty, that means if a deviation is reproduced perfectly in the simulation, no uncertainty is assigned. The contribution of each source was added in

Variable	Loose	Default	Tight
TPC crosses rows	≥50	≥ 70	≥110
Ratio crossed rows over find.	≤0.5	≤0.8	≤0.9
Number of TPC clusters	≥60	≥ 70	≥80
Number of ITS clusters	≥1	≥ 2	≥3
χ^2 of track fit per TPC cluster	≤6	≤ 4	≤3
χ^2 of track fit per ITS cluster	≤49	≤ 36	≤25
Hit in SPD detector	no requirement	required	required in first SPD layer

Table 4.1.: Track cut variations used for systematic studies

quadrature and the final result is summarised in Figure 4.1.

4.2. Particle identification

The second source of systematic uncertainty for this analysis comes from PID. In order to estimate this uncertainty, the impact on the analysis of the implemented PID selection and the procedure of TOF m^2 fit was studied.
For systematic studies of the PID selection criteria, the absolute value of n$\sigma_{p,d}$ is varied separately for all detectors according to Table 4.2. For each variation the analysis was repeated and the maximal resulting deviation from the default results was taken as uncertainty. MC data was analysed in the same way and the relative difference between the experimental results and simulation has been taken as systematic uncertainty.
To study the uncertainty on the analysis due to the TOF m^2 fit procedure, two fit parameters have been varied according to Table 4.2 and the fits were performed again for each variation. The uncertainty from this source was estimated by summing up the relative differences to the default analysis in quadrature.
The total systematic uncertainty due to particle identification was finally calculated by adding these two contribution in quadrature and is shown in Figure 4.1.

Particle	PID selection	Loose	Default	Tight	Range $[GeV/c]$
(anti-)proton	$\lvert\mathrm{TPCn}\sigma_\mathrm{p}\rvert$	<4	< 3	<2	$[0.2;\infty]$
	$\lvert\mathrm{TOFn}\sigma_\mathrm{p}\rvert$	<4	< 3	<2	$[0.7;2.5]$
(anti-)deuteron	$\lvert\mathrm{TPCn}\sigma_\mathrm{d}\rvert$	<4	< 3	<2	$[0.2;\infty]$
	$\mathrm{ITSn}\sigma_\mathrm{d}$	>-1	> -2	>-3	$[0.2;1.4]$

Fit parameter	Wide	Default	Tight
Fit range (protons), $(\mathrm{GeV}/c^2)^2$	(0.1, 2.2)	(0.2, 2.0)	(0.3, 1.8)
Fit range (deuterons), $(\mathrm{GeV}/c^2)^2$	(1.7, 5.3)	(2.0, 5.0)	(2.3, 4.7)
Bin size, $(\mathrm{GeV}/c^2)^2$	0.04	0.02	0.01

Table 4.2.: PID cut variation and variation of TOF m^2 fit parameters

4.3. Secondary (anti-)particles

The last studied source of system uncertainty is related to the Secondary correction of (anti-)particle's momentum spectra, which is the template fit procedure to DCA_{xy} distributions. For systematic studies the DCA cuts and the fit parameters used in the analysis have been varied according to Table 4.3. The presented fit range has been varied between $(-0.8, 0.8)$ cm and $(-0.2, 0.2)$ cm in 0.1 cm steps. The signal template function has been flipped between particles and anti-particles, for deuterons the MC template of primary deuterons has been used instead of the experimental anti-deuteron distribution. The template fit has then been repeated again for all variations.

For the case of $\bar{\mathrm{p}}/\mathrm{p}$ ratio, the relative differences to the default result are taken as uncertainties and are added in quadrature to finally result as total systematic uncertainty due to secondary correction.

For the (anti-)deuteron analysis, the total systematic uncertainty due to secondaries, shown in Figure 4.1, has been evaluated as an RMS value of the distribution of all $\bar{\mathrm{d}}/\mathrm{d}$ ratios resulting from all permutations of the variations.

Variable	**Loose**	**Default**	**Tight**
DCA$_{xy}$, (cm)	0.5	0.1	0.05
DCA$_z$, (cm)	1.0	0.2	0.1
Fit parameter	**Wide**	**Default**	**Tight**
Fit range, (cm)	(-0.8, 0.8)	(-0.6, 0.6)	(-0.2, 0.2)
Bin size, (cm)	0.05	0.025	0.01
Signal template	-	particle	anti-particle

Table 4.3.: DCA cut variations and template fit parameters variations

4.4. Total systematic uncertainty

Finally, all estimated systematic uncertainties from different sources were added in quadrature, and the resulting total systematic uncertainty is also shown in Figure 4.1. It can be seen that secondary rejection has a significant systematic uncertainty on the anti-particle to particle ratio at low momenta for both collision systems and particles species. The shape for (anti-)deuterons originates from the chosen method of evaluating the RMS distribution in each p bin as discussed before. In the low momentum range, where no TOF PID is applied, the systematic uncertainty related to PID is small because of a clear separation of the signals in the TPC. This uncertainty rises immediately when fits to TOF m^2 distributions are applied, due to the tail of the kaon (proton) m^2 distribution, which contaminates the (anti-)proton ((anti-)deuteron) signal in the TOF. The visible differences related to this uncertainty between pp and p–Pb analysis originates from one additional implemented feature when estimating the uncertainty in pp analysis. It consists in fitting the resulting ratios from the variations of TOF m^2 fit parameters with a polynomial function, and take the values from the fit curve as deviation. In this way, fluctuation from single bins are averaged out and the systematic uncertainty drops significantly for the $\bar{\mathrm{d}}$/d ratio.

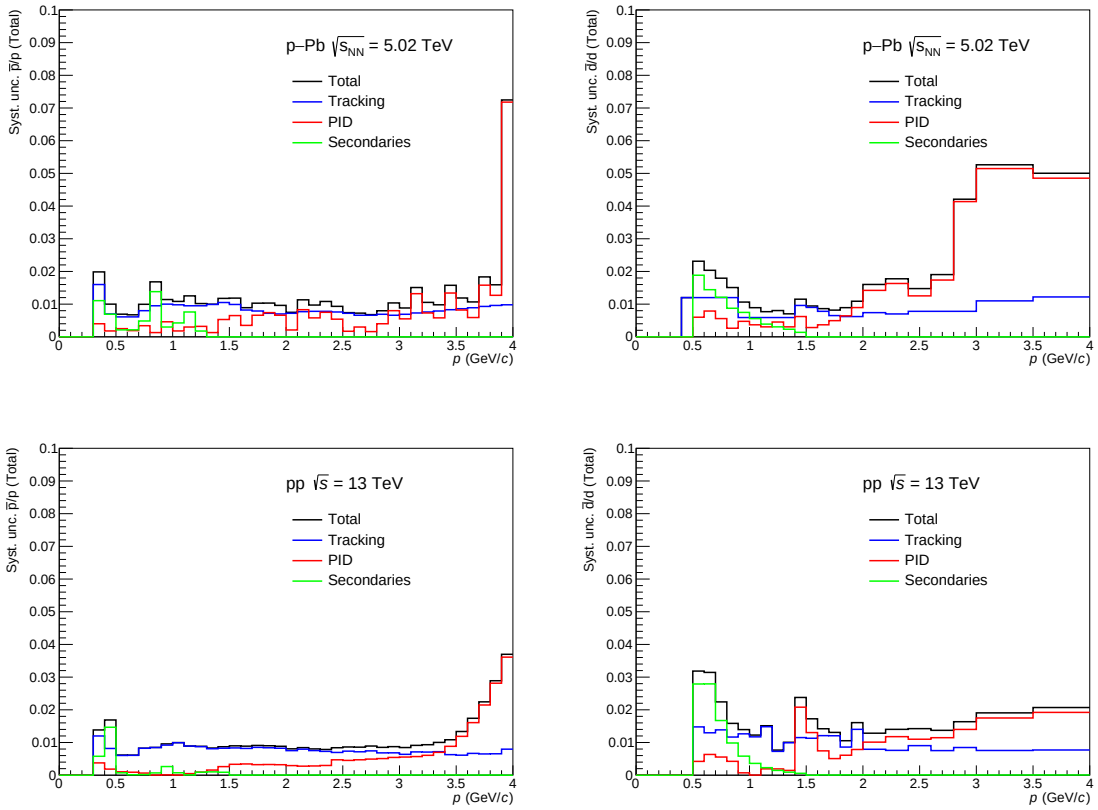

Figure 4.1.: Total systematic uncertainty for $\bar{\mathrm{p}}/\mathrm{p}$ (left) and $\bar{\mathrm{d}}/\mathrm{d}$ (right) as a function of momentum for both p–Pb (top) and pp (bottom) collisions.

4.5. Global uncertainty from primordial ratio

High-energy proton-proton collisions should produce matter and anti-matter in almost same amount. A dedicated study to measure the (anti-)proton production yields and its ratio at various collision energies was performed in ALICE [34]. The ratios conclude to reach compatibility with unity for pp collisions at $\sqrt{s} = 7$ TeV and are summarised in Table 4.4. These results were extrapolated linearly to estimate the $\bar{\mathrm{p}}/\mathrm{p}$ primordial ratio and its uncertainty of the collision energies used in this thesis, these are $\sqrt{s} = 5$ TeV and $\sqrt{s} = 13$ TeV. Further, the primordial ratio of $\bar{\mathrm{d}}/\mathrm{d}$ is assumed to be $(\bar{\mathrm{p}}/\mathrm{p})^2$ [33]. The resulting primordial ratios and its uncertainties for this work are shown in Table 4.5.

Energy ($\sqrt{s}$)	$\bar{\mathrm{p}}/\mathrm{p}$ **ratio**	**stat.**	**syst.**
0.9 TeV	0.957	0.006	0.014
2.76 TeV	0.977	0.002	0.014
7 TeV	0.991	0.005	0.014

Table 4.4.: The integrated over mid-rapidity yields $\bar{\mathrm{p}}/\mathrm{p}$ ratios with statistical and systematic uncertainties for various collision energies [34].

Energy ($\sqrt{s}$)	$\bar{\mathrm{p}}/\mathrm{p}$ **ratio**	$\bar{\mathrm{d}}/\mathrm{d}$ **ratio**
5 TeV	0.984 ± 0.015	0.968 ± 0.030
13 TeV	0.998 ± 0.015	0.980 ± 0.030

Table 4.5.: Primordial ratios and unc. needed for this work. Values from Table 4.4 are extrapolated to obtain these results.

5. Monte Carlo Studies

Monte Carlo (MC) simulations are very important utensils for particle physics experiments, in order to design and tune the detectors and analysis strategies. In ALICE almost each period of the reconstructed experimental data has its corresponding MC simulation datasets, all stored in official data repositories. The simulations are performed by passing through mainly two steps, which are MC simulations of the collisions and MC simulations of the passage of particles through matter.
First, MC event generators run simulations of a desired collision system, using software libraries as for example PYTHIA [35] or DPMJET [36]. As in a real collision, the outcomes of a simulated collision are particles with observables such as mass, momentum and many others. The difference however is, that in simulations these quantities are stored as so called MC truth samples, whereas in real collisions they are a priori not known.
In the second part, a simulation of the subsequent steps is performed. In these simulations the generated particles are propagated through the detector using software libraries such as Geant4 toolkit [22], which contain the exact geometry and state of the detector during the data taking. The simulated output of the detectors have the same type of information as the one from real data. Thus, these signals are then used to reconstruct the events with the same algorithm employed for real collisions.

In this thesis a special MC production was used, in which the actual collision was not simulated, the desired (anti-)particles simply come out of a "Box" with realistic distributions of several observables so each event contains one deuteron (proton) and one anti-deuteron (anti-proton). This can be used to study the (anti-)particle interaction with the detector material. In section 5.1 the anti-particle to particle ratios are constructed by using different MC datasets and compared to the experimental data. In order to investigate in more details these results, a simple Geant4-based model has been set up which is described in section 5.2.

5.1. Anti-Particle to particle ratios from simulations

Similar to the analysis methods presented in chapter 3, the anti-particle to particle ratios were constructed using MC datasets. The results from experimental data were compared to two different MC datasets, namely to the full-scale ALICE simulations using Geant3 and using Geant4 toolkits for the propagation of (anti-)particles through the detectors. The comparison is shown in Figure 5.1 for p–Pb and for pp collisions.

As explained, in contrast to actual collisions, in simulations the MC truth information

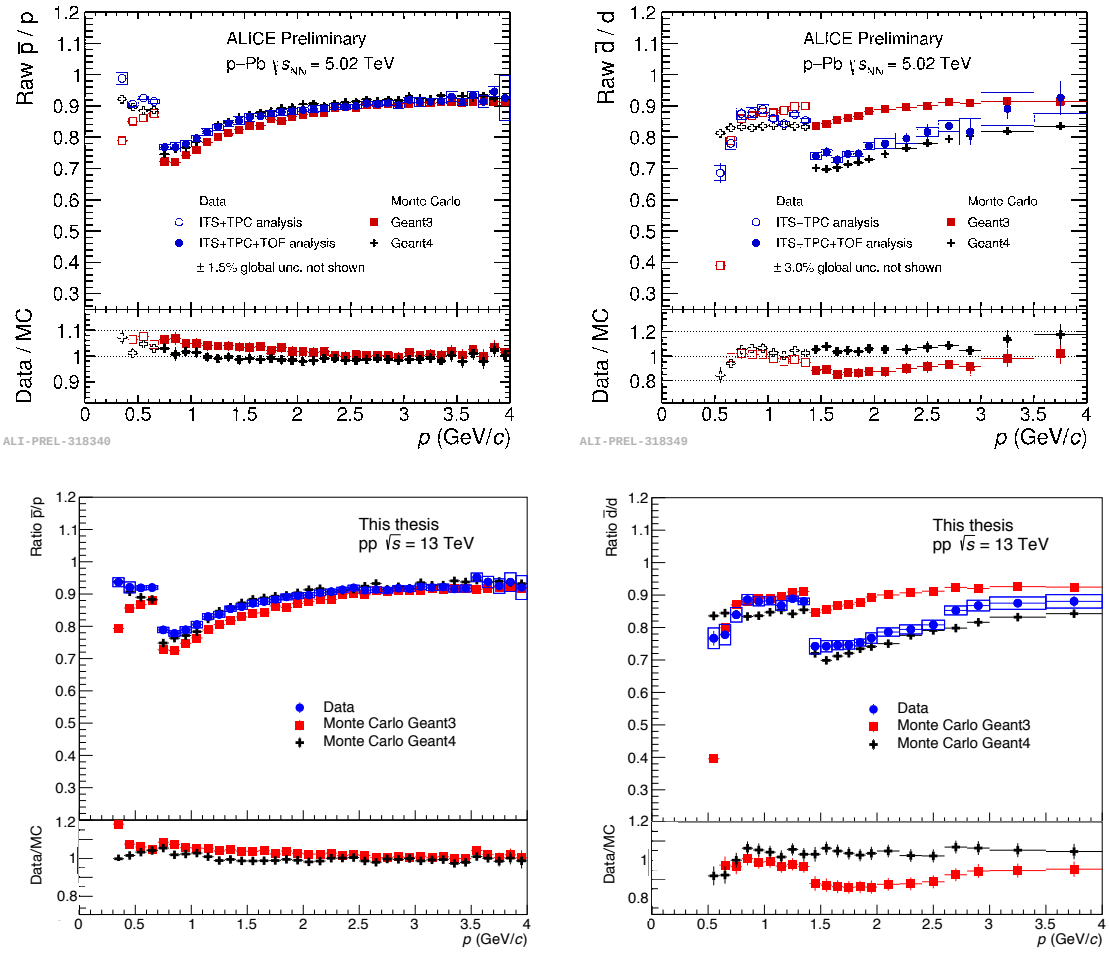

Figure 5.1.: Raw primary $\bar{p}/p$ (left) and $\bar{d}/d$ (right) ratios from p–Pb (top) and pp (bottom) collisions compared to full-scale ALICE simulations based on Geant3 and Geant4. Statistical and systematic uncertainties of experimental data are shown on the top plots as vertical bars and boxes, correspondingly. The lower panels in each figure show the ratio between experimental data and Monte Carlo results, with the errors corresponding to the quadratic sum of statistical, systematic and global uncertainties.

can be accessed. Pure primary (anti-)protons and (anti-)deuterons have been selected on generated level by using this information, and the same track and PID selection criteria as for experimental data have been applied to the reconstructed MC tracks. Since in the used MC production anti-nuclei and nuclei come out of a "Box" with a $1:1$ ratio, the Monte Carlo results are scaled, according to Table 4.5, with a correction factor of 0.984 (0.968) for $\bar{p}/p$ ($\bar{d}/d$) ratio in p–Pb analysis and with a factor of 0.998 (0.98) for $\bar{p}/p$ ($\bar{d}/d$) ratio in pp analysis.

Figure 5.1 shows clearly that both simulations, using Geant3 and Geant4, are able to at least qualitatively reproduce higher absorptions of anti-particles than particles in the detector material. A ratio lower than unity and the step between the high and the low momentum region are evidences for this. It can be seen that for $\bar{p}/p$ ratios the experimental data are

in better agreement with Geant4 simulations for momenta below $p \sim 2$ GeV/c, above this values it is in agreement within uncertainties with both Geant versions. For $\bar{\mathrm{d}}$/d ratios the simulations using Geant4 are clearly in much better agreement with experimental data in most of the momentum bins. Thus, the propagation of (anti-)deuterons through the ALICE detector is described better by using Geant4 based simulations.
With this conclusion, the subsequent work was done by using only MC simulations based on Geant4.

5.2. Simple Geant4 Model

In order to understand in more details the anti-particle-to-particle ratios, a simple Geant4-based model has been set up to produce (anti-)particle spectra and corresponding ratios. The advantage of using such productions is that the simulation time and memory cost are significantly lower than in full-scale ALICE simulations. Using this model, the simulation can be run on local machines and is flexible for any change that needs to be implemented. In this section the basic structure for this simple model is presented.

The main idea is shown schematically in Figure 5.2. It consists in taking a source of (anti-)protons and (anti-)deuterons with a realistic momentum distribution, propagating them through a material that mimics the ALICE detector by using Geant4 and finally analyze the outcome.
(anti-)protons and (anti-)deuterons can interact inelastically with the ALICE detector material when flying through the experimental setup. To account for this effect, the target material for the simple Geant4 model is made out of material slices, which represent the average thickness of the ALICE detector materials in perpendicular direction from the beam axis.
Due to elastic re-scattering of (anti-)particles with the detector material, their trajectory can significantly be modified which can result in a "loss" of (anti-)particles in final raw spectrum in the real experiment. This effect can happen, either because the track reconstruction algorithm fails to find the corresponding track or because a scattered track does not fulfil the selection criteria used in the analysis anymore. To account for these effects in the simple model, a limit of a maximal re-scattering angle is introduced, all (anti-)particles exceeding this limit are "lost" as in the real experiment.

In Figure 5.3 the resulting anti-particle to particle ratios using the simple Geant4 model is shown compared to the ratios from full-scale ALICE simulations. A very good agreement can be seen between the two simulations at high momentum for both $\bar{\mathrm{p}}$/p and $\bar{\mathrm{d}}$/d. Some disagreements observed in the lower momentum range are due to not yet fully understood effects and need further investigation. Therefore the used momentum range to extract the anti-particle's inelastic cross-sections in this work is limited to the high momentum range

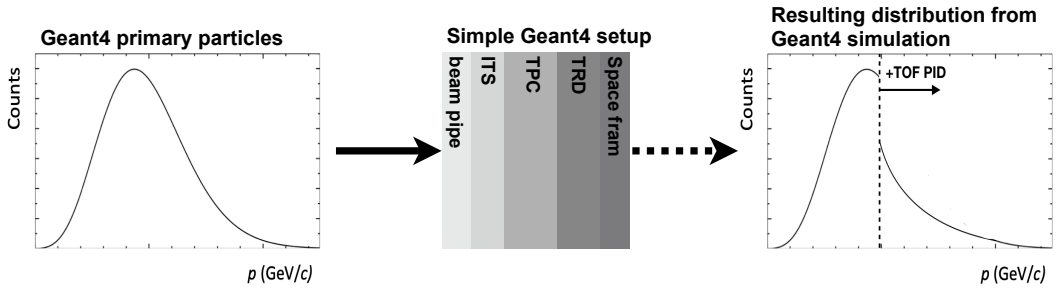

Figure 5.2.: Schematic representation of the simple Geant4 model. Fro left to right: a source of (anti-)particles with a realistic momentum distribution is propagated through a material (target) that mimics the ALICE detector by using Geant4. In the final step the outcome is analysed.

$p > 1.4$ GeV/c for $\bar{\mathrm{d}}$ and $p > 0.7$ GeV/c for $\bar{\mathrm{p}}$.

As mentioned, by using a simple model the implementation of some modifications is facilitated. This advantage was taken to vary the inelastic cross-section of anti-protons by 10% and of anti-deuterons by 15% to see how this influences the results. The effect can be seen in Figure 5.3. This variation has a higher effect on the ratio in the higher momentum range due to the fact that (anti-)particles travers more material to reach the TOF detector. The dependence between the raw primary anti-particle to particle ratios and the variation of the inelastic cross-sections of (anti-)particles is the key element, which allows to extract constraints on the anti-proton and on the anti-deuteron inelastic cross-sections.

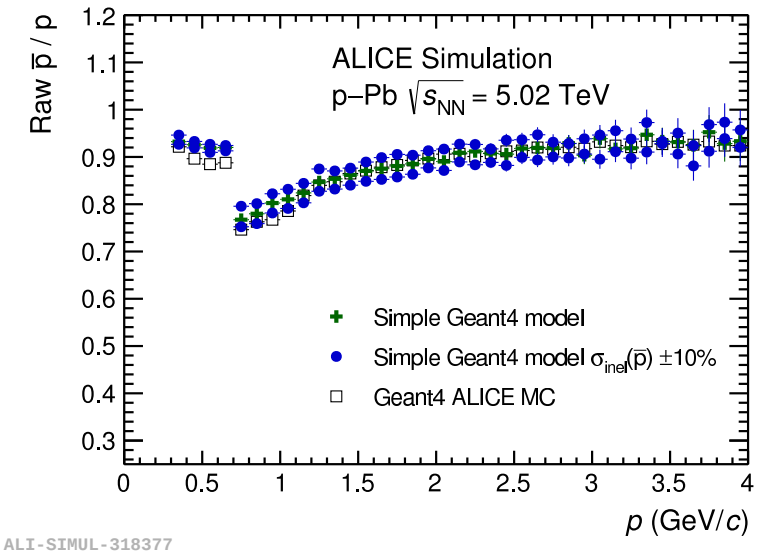

(a) Anti-proton to proton ratio

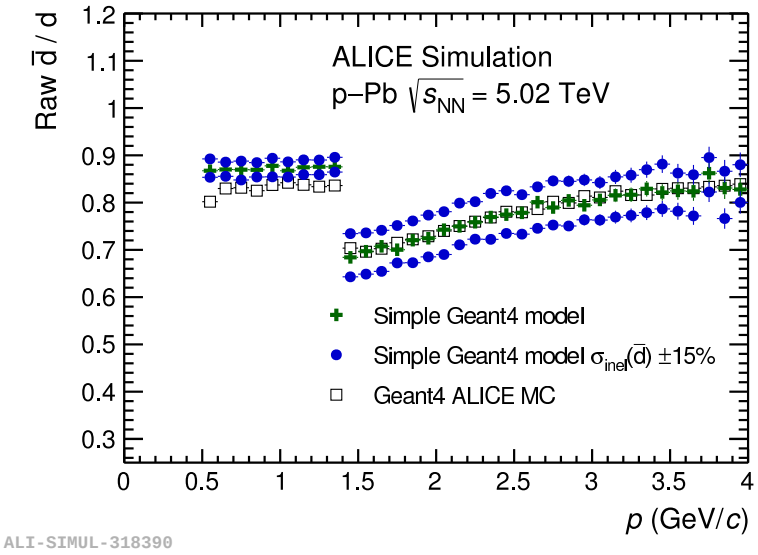

(b) Anti-deuteron to deuteron ratio

Figure 5.3.: Raw primary anti-particle to particle ratios as a function of momentum in simple Geant4 model and in full ALICE Monte Carlo simulations. The blue markers correspond to the results of simple Geant4 model with modified inelastic cross-sections. The same dependence is assumed for pp collisions at $\sqrt{s} = 13$ TeV.

6. Results

The extraction of upper and lower limits of the anti-deuteron inelastic interaction cross-sections is done by comparing the experimental data with simple Geant4-based MC simulations where $\sigma_{\text{inel}}(\bar{\text{p}})$ or $\sigma_{\text{inel}}(\bar{\text{d}})$ can be easily varied. The results for $\sigma_{\text{inel}}(\bar{\text{p}})$ serve as a benchmark for this analysis. Section 6.1 outlines this procedure and compares the results for p–Pb analysis and pp analysis. In section 6.2 the effect of continuous energy loss of (anti-)particles in the detector material is described, and also how this effect is taken into account in the results $\sigma_{\text{inel}}(\bar{\text{p}})$ and $\sigma_{\text{inel}}(\bar{\text{d}})$.

6.1. Constraints on the anti-deuteron inelastic cross-sections

The idea how to get $\pm1\sigma$ and $\pm2\sigma$ limits, is to vary the anti-particle inelastic cross-section in MC data so that the anti-particle to particle ratio reaches the $\pm1\sigma$ and $\pm2\sigma$ experimental limits. Such variations correspond therefore to $\pm1\sigma$ and $\pm2\sigma$ experimental limits for the inelastic cross-sections. To get $\pm1\sigma$ uncertainty on the ratio, all possible sources are added in quadrature. These sources of uncertainties are described in more details in the following and can be seen in Figure 6.1.

The **statistical** and **systematic** uncertainties of the experimental data are the most natural contribution to this uncertainty and were already discussed in chapter 4. The global uncertainty from the **primordial ratio** is also a part of the uncertainty sources in order to extract the upper and lower limits for $\sigma_{\text{inel}}(\bar{\text{p}})$ and $\sigma_{\text{inel}}(\bar{\text{d}})$. This already takes into account the uncertainty due to a limited precision of knowledge of the ALICE material budget which amounts to 0.5% (1%) of a total of 1.5% (3%) for $\bar{\text{p}}$/p ($\bar{\text{d}}$/d).

Inelastic cross-sections of particles also have an influence on the anti-particle to particle ratio. To account for this effect, it was studied how precise the inelastic cross-sections of protons ($\sigma_{\text{inel}}(\text{p})$) and deuterons ($\sigma_{\text{inel}}(\text{d})$) are described in Geant4. To do so, the agreement between the implemented cross-sections in Geant4 and the existing experimental data has been estimated by shifting the Geant4 parameterisations up and down by a common scaling factor. This is possible due to the fact that there are experimental results for $\sigma_{\text{inel}}(\text{d})$, also some measurements at low momenta as presented in chapter 1. The best agreement between simulation and experimental data is achieved for the factor of 0.9925 ± 0.035 (1.0175 ± 0.07) for protons (deuterons), which means that on average the experimental data are well described by Geant4 parameterisations. Further, to estimate the impact of the inelastic cross-sections of protons (deuterons) on the $\bar{\text{p}}$/p ($\bar{\text{d}}$/d) ratio, $\sigma_{\text{inel}}(\text{p})$ ($\sigma_{\text{inel}}(\text{d})$) has been

varied by 3.5% (7%) in simple Geant4 simulations. This lead to an uncertainty of 0.5% (1%) for the resulting $\bar{\mathrm{p}}/\mathrm{p}$ ($\bar{\mathrm{d}}/\mathrm{d}$) ratio.
The effect of **elastic cross-sections** (σ_{el}) plays a role on multiple scattering on the detector material and affects for instance ITS-TPC matching efficiency and therefore the ratio. The uncertainty due to σ_{el} has been estimated by varying the elastic cross-section of each (anti-)particle, separately one by one, by 20% in the simple Geant4 model. The impact on the anti-particle to particle ratio has then been taken as uncertainty. In Figure 6.1 it can be seen that σ_{el} depends on the (anti-)particles momentum and the material budget.
Thus $\pm 1\sigma$ corresponds to the quadratic sum of all mentioned sources of uncertainties and is labeled as the total uncertainty in Figure 6.1.

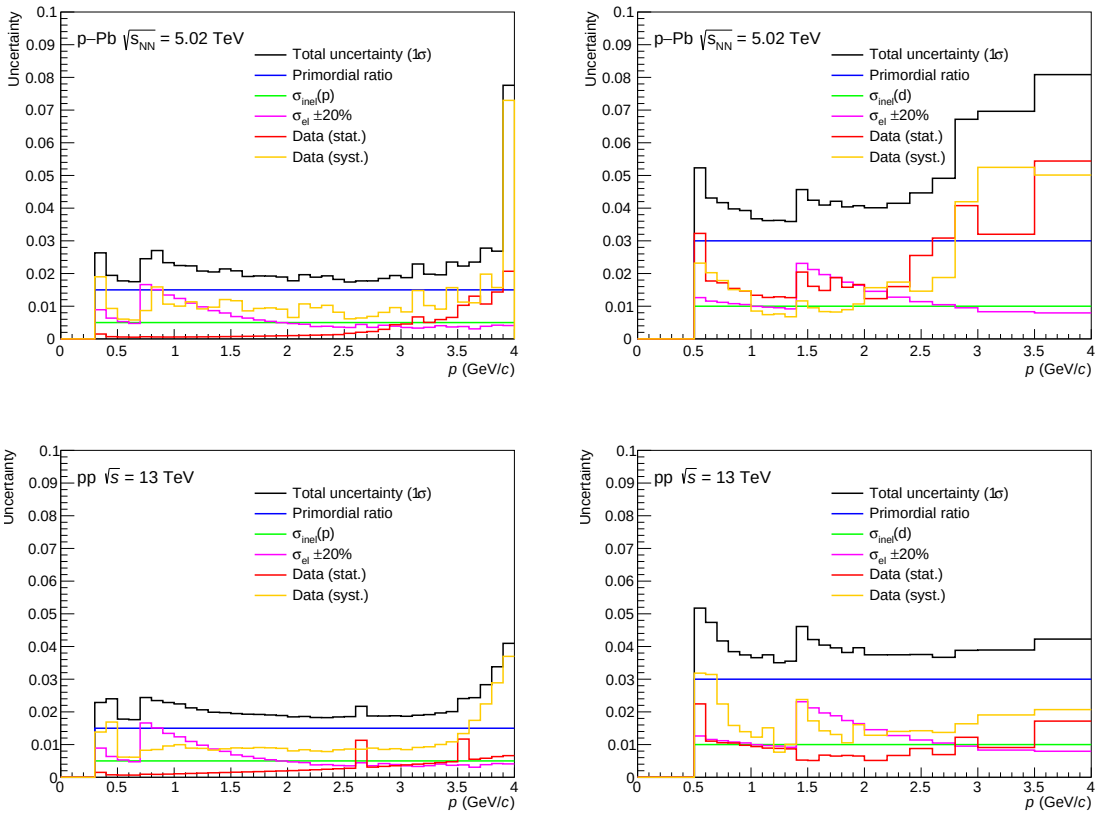

Figure 6.1.: Summary of all uncertainties used for the constraints on $\sigma_{inel}(\bar{\mathrm{p}})$ (left) and on $\sigma_{inel}(\bar{\mathrm{d}})$ (right) for both analysed collision systems p–Pb (top) and pp (botton). For the total uncertainty, all sources are added in quadrature.

These uncertainties are added as $\pm 1\sigma$ and $\pm 2\sigma$ to the experimental anti-particle to particle ratios as Figure 6.2 shows together with the raw primary $\bar{\mathrm{p}}/\mathrm{p}$ ($\bar{\mathrm{d}}/\mathrm{d}$) ratio from full ALICE simulation. These experimental limits can be translated into $\pm 1\sigma$ and $\pm 2\sigma$ limits for the inelastic interaction cross-sections of anti-protons and anti-deuterons, for which one needs to know the dependence between ratio and $\sigma_{\mathrm{inel}}(\bar{\mathrm{d}})$ and $\sigma_{\mathrm{inel}}(\bar{\mathrm{p}})$. This dependence is assumed to be linear, which is well confirmed by simple Geant4 simulations as can be

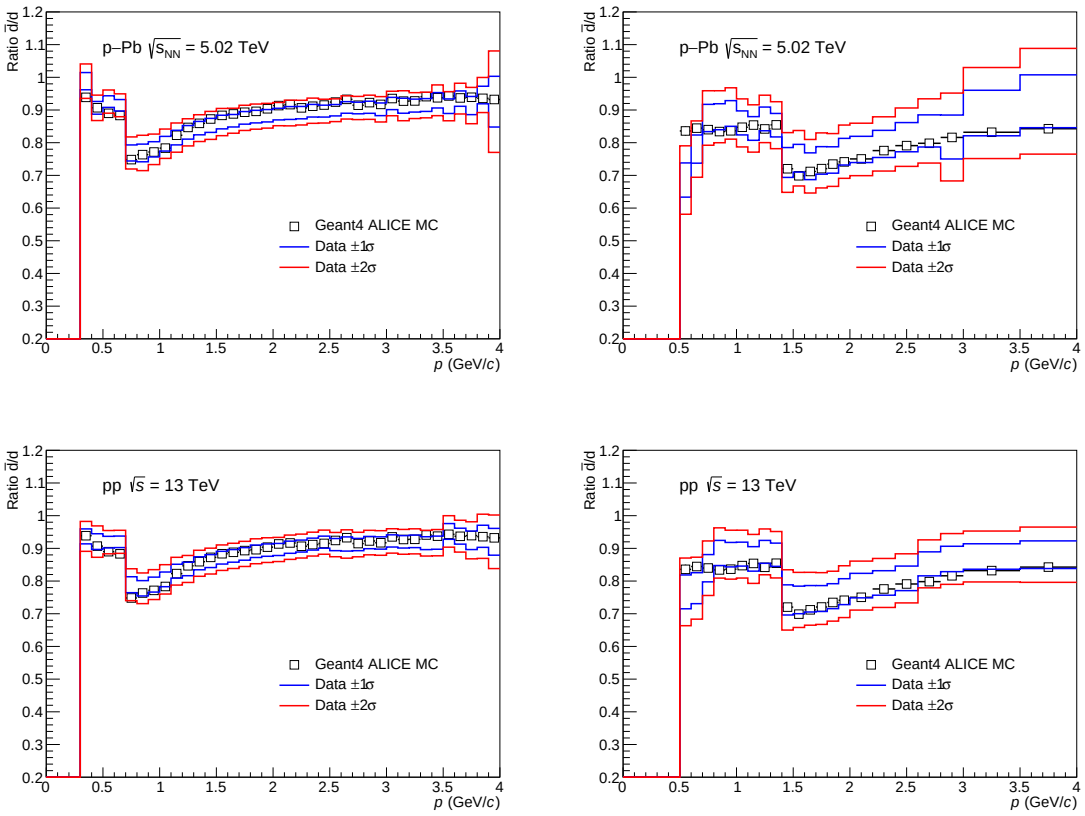

Figure 6.2.: Raw $\bar{p}/p$ (left) and $\bar{d}/d$ (ratios) ratios in full ALICE Monte Carlo simulations in comparison with the experimental $\pm1\sigma$ and $\pm2\sigma$ limits from p–Pb (top) and pp data analysis.

seen in Figure 6.3. Scaling the cross-section up (down) by a certain amount and increasing (decreasing) this factor linearly has the consequence that the ratio decreases (increases) linearly. In Figure 6.4 the procedure to translate the limits from experimental data into cross-sections is presented for one momentum interval, all fits are shown in Appendix C. It shows the resulting anti-deuteron to deuteron ratio with varied $\sigma_{\text{inel}}(\bar{d})$ from Figure 5.3 and $\pm1\sigma$ and $\pm2\sigma$ experimental limits from Figure 6.2 for momentum interval $1.4 < p < 1.5$ GeV/c as a function of the re-scaling factor for $\sigma_{\text{inel}}(\bar{d})$. The black line represents a linear fit to the results from simple Geant4 simulations with modified inelastic cross-sections, which have a known re-scaling factor of $\sigma_{\text{inel}}(\bar{p}) \pm 10\%$ for protons and $\sigma_{\text{inel}}(\bar{d}) \pm 15\%$ for deuterons. The factor by how much the Geant4 parametrization needs to be scaled in order to reach $\pm1\sigma$ and $\pm2\sigma$ experimental limits corresponds to the interception of the linear fit and the corresponding horizontal blue or red line. As discussed in section 5.2, only in the high momentum range an agreement between the simple Geant4 model and the full ALICE simulation is found, therefore the constraints on inelastic cross-sections have been extracted only in this momentum range. This procedure is repeated in each momentum bin in order to get 4 scaling factors ($\pm1\sigma$ and $\pm2\sigma$) as a function of the momentum. Finally, the results are obtained for a hypothetical element, with $Z = 11.9$ and $A = 25.5$, which is the average

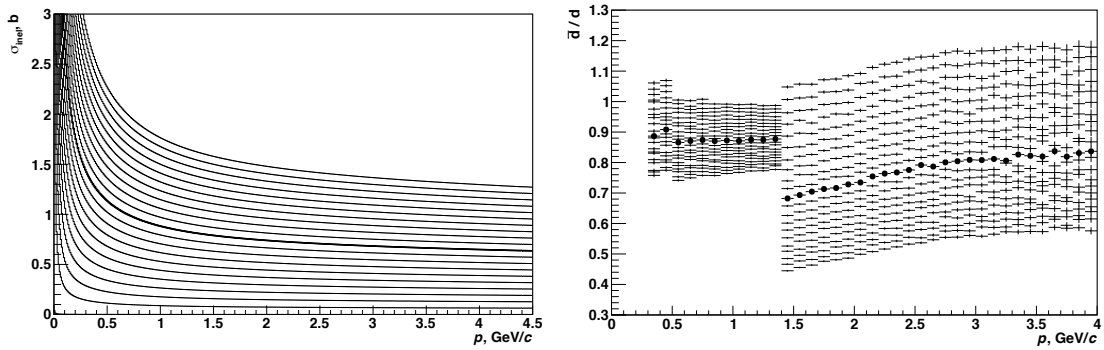

Figure 6.3.: Left: variations of $\sigma_{\mathrm{inel}}(\bar{\mathrm{d}})$ in simple Geant4 model used to test the assumption of linear dependence between $\sigma_{\mathrm{inel}}(\bar{\mathrm{d}})$ and $\bar{\mathrm{d}}$/d ratio. Right: the resulting $\bar{\mathrm{d}}$/d ratios as a function of momentum. Thick line (thick points) on the left (right) plot corresponds to the default parameterisation implemented in Geant4.

over the ALICE detector materials from the primary vertex up to the TOF detector. The results are shown in Figure 6.5 together with the default Geant4 parametrization for such an element. The p–Pb analysis results show wider limits and more fluctuations compared to the pp analysis, mainly due to higher and more fluctuating systematic and statistical uncertainty. The results for $\sigma_{\mathrm{inel}}(\bar{\mathrm{p}})$ are in good agreement with Geant4 parametrization, which in turn describes well experimental data as presented in chapter 1. This demonstrate that the procedure works for anti-protons and it can be used as a benchmark giving more confidence on the results of $\sigma_{\mathrm{inel}}(\bar{\mathrm{d}})$.

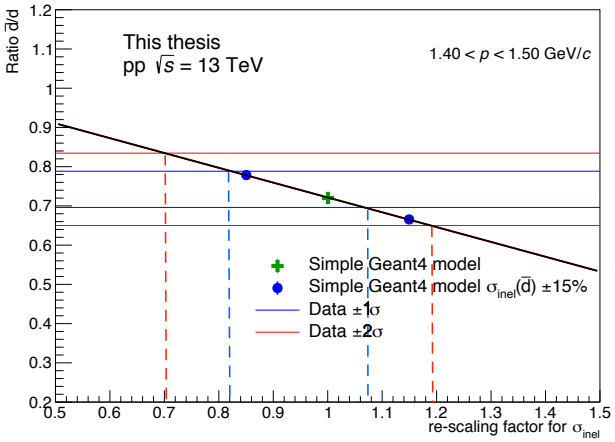

Figure 6.4.: $\bar{\mathrm{d}}$/d ratio in one momentum interval $1.4 < p < 1.5$ GeV/c as a function of re-scaling factor applied to $\sigma_{\mathrm{inel}}(\bar{\mathrm{d}})$. The black line performs a linear fit to the known $\sigma_{\mathrm{inel}}(\bar{\mathrm{d}}) \pm 15\%$ variations and the default parameterization in green. Finally the interception of the horizontal blue and red lines and the fit line represent the re-scaling factor to reach $\pm 1\sigma$ and $\pm 2\sigma$ experimental limits.

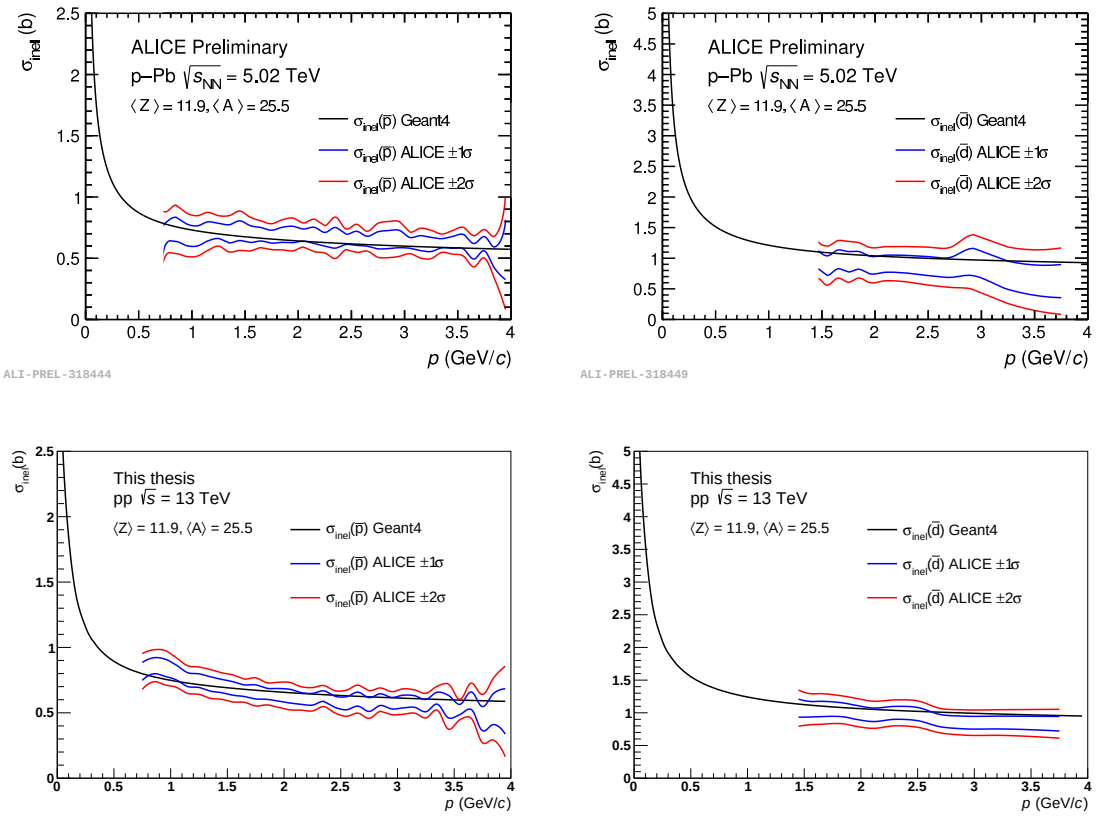

Figure 6.5.: Inelastic interaction cross-section of anti-protons (left) and anti-deuterons (right) per element averaged over the ALICE detector materials (with Z = 11.9 and A = 25.5). The Geant4 parameterisation is shown as a black line, and the constraints from experimental ALICE data are shown as blue ($\pm 1\sigma$) and red ($\pm 2\sigma$) lines. The top row corresponds to the analysis of p–Pb data at collision energy of $\sqrt{s_{\mathrm{NN}}} = 5.02$ TeV and the bottom row to data from pp collision at of $\sqrt{s} = 13$ TeV.

6.2. Energy loss effects and estimation of annihilation momentum

As presented in the previous section, ALICE uses characteristic energy loss for particle identification. Losing energy in this context means that the created particle loses some of its momentum. This in turn influences the results presented so far in this work, because instead of plotting the constraints of the cross-sections as a function of the vertex momentum p it should be plotted as a function of momentum p^* at which the inelastic interaction happened. In order to correct the results, by translating p into p^* ($p \rightarrow p^*$), an analysis has been performed in Monte Carlo data using the help of so called track references. Inside these track references, information about each generated (anti-)particle is stored, comparable to the MC truth information explained in chapter 5. One of these informations is the track momentum at a certain location. As an estimation of p^*, the last stored momentum of each track has been taken. Figure 6.6 shows the ratio of p^*/p as a function of momentum p at

the vertex and there is indeed an effect due to energy loss, p^* is smaller than p as expected. Specially at low (vertex) momenta the difference is significant.
In order to take this effect into account and translate $p \to p^*$, Figure 6.6 was used as a momentum transformation map. For example, to translate the first bin for anti-protons, which starts at $p_1 = 0.7$ GeV/c it needs to be scaled with p_1^*/p_1, in this case

$$p_1^* = 0.7 \text{ GeV}/c \cdot 0.89 \qquad \Rightarrow \qquad p_1^* = 0.623 \text{ GeV}/c \tag{6.1}$$

It must be noted that for this procedure, only mean values of p^*/p have been used. The results from Figure 6.5 will be stretched along the x-axis as a result of $p \to p^*$ transformation. This behaviour is shown in Figure 6.7, where the colored blue and red curves represent the results as a function of the momentum and the dashed black curves are the ones for the vertex momentum. The effect is small but visible, specially for low momenta. For anti-protons (anti-deuterons) with momenta higher than ~ 1.5 GeV/c (~ 2.0 GeV/c) this effect makes no difference in the results and can be neglected.

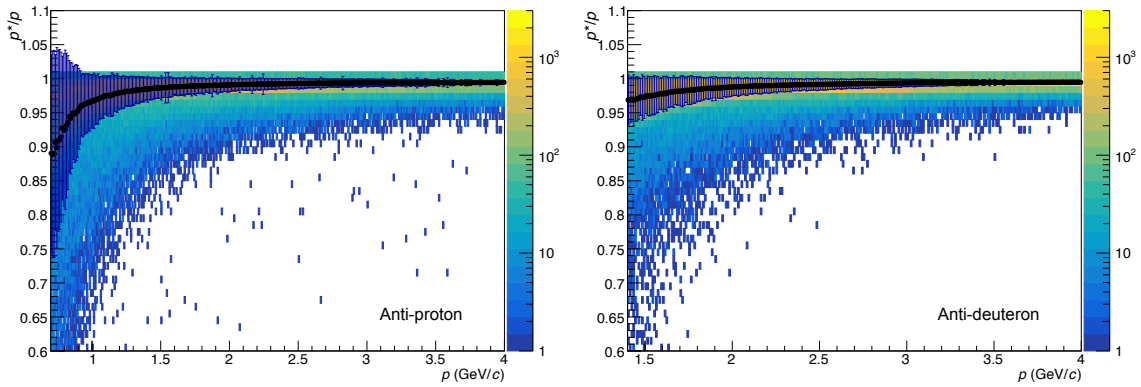

Figure 6.6.: The ratio of p^*/p as a function of momentum p at the vertex for anti-protons (left) and anti-deuterons (right). The black points and errors represent the mean p^*/p values and the corresponding RMS in each momentum bin. Note that the momentum on the x-axis only shows the range where TOF PID is applied.

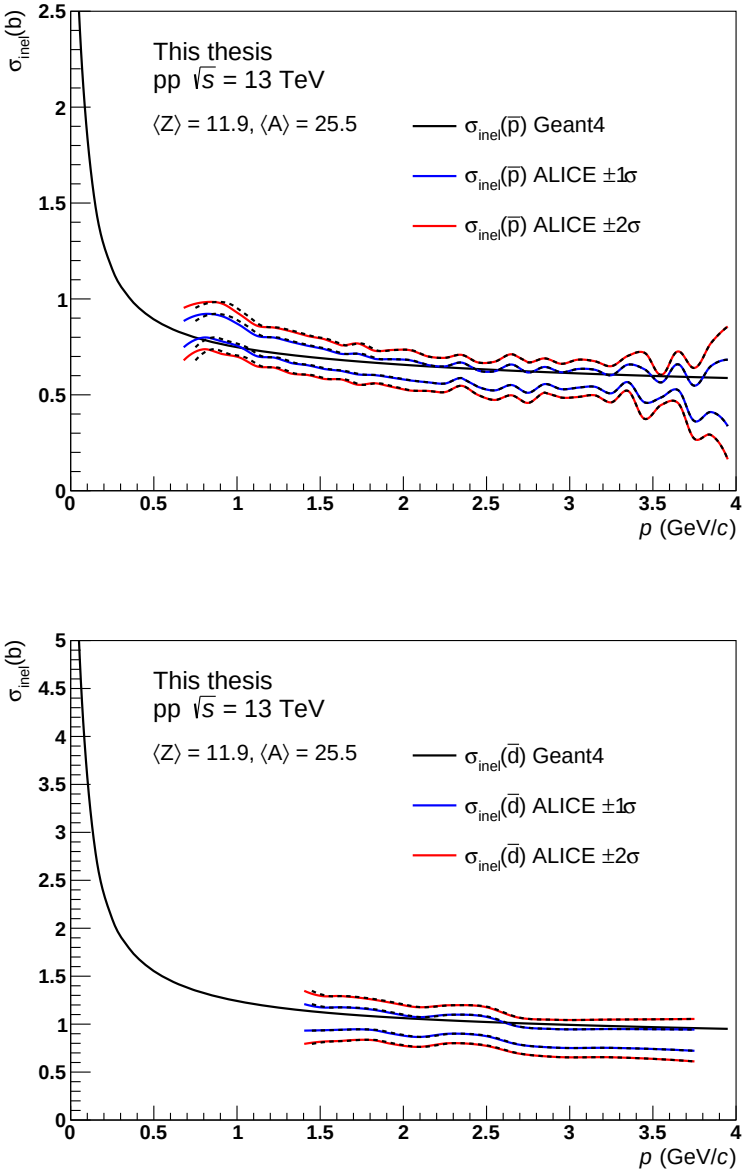

Figure 6.7.: Inelastic interaction cross-section of anti-protons (top) and anti-deuterons (bottom) per element averaged over the ALICE detector materials (with Z = 11.9 and A = 25.5) as a function of the real annihilation momentum. The Geant4 parameterisation is shown as a black line, and the constraints from experimental ALICE data are shown as blue ($\pm 1\sigma$) and red ($\pm 2\sigma$) lines. The dashed line on top of each of the lines corresponds the the results where $p \to p^*$ transformation is not applied.

6.3. Comparison to existing data

Existing experimental results for $\sigma_{\text{inel}}(\bar{\text{p}})$ can be well described by Geant4 parameterization as presented in chapter 1, thus the constraints achieved for $\sigma_{\text{inel}}(\bar{\text{p}})$ are in good agreement with previous measurements. As showed in the Introduction, for $\sigma_{\text{inel}}(\bar{\text{d}})$ only a very limited amount of measurements exist, which are also obtained for much higher momenta compared to the results from this thesis. In Figure 6.8 the comparison between existing data and the results from this work can be seen. The experimental data points correspond to $\sigma_{\text{inel}}(\bar{\text{d}})$ on aluminium which has similar atomic and mass number as the calculated average ALICE element. The presented results are normalised by $1/\sqrt{A}$ in order to minimise the dependence on the mass number A. It can be seen that the results of this thesis cover wide momentum range, with the precision of the constraints compatible to the uncertainties of the actual measurement at $p = 25$ GeV/c.

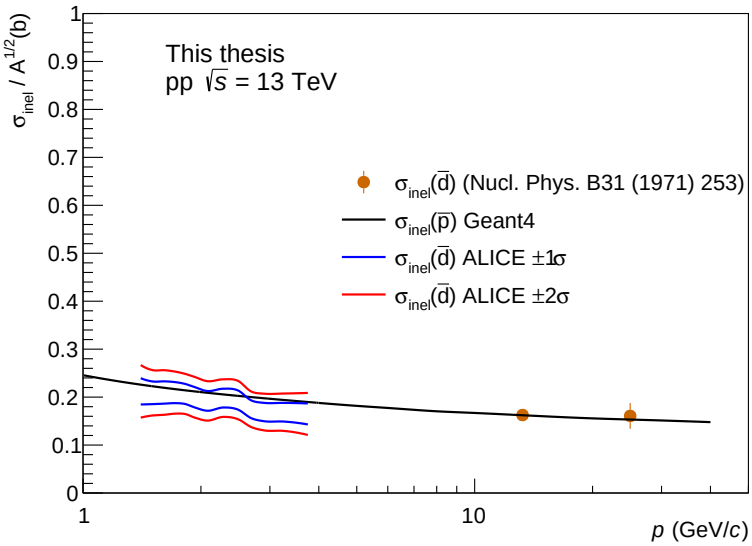

Figure 6.8.: The results from this work compared to existing data of $\sigma_{\text{inel}}(\bar{\text{d}})$ at $p_{\bar{\text{d}}} = 13.3$ GeV/c $p_{\bar{\text{d}}} = 25$ GeV/c on aluminium target.

7. Summary and Outlook

This thesis presented the first experimental constraint at low momenta of the anti-deuteron inelastic cross-sections, which have been extracted by analysing p–Pb and pp collisions at $\sqrt{s_{\mathrm{NN}}} = 5.02$ TeV and $\sqrt{s} = 13$ TeV in ALICE at LHC. The same analysis has been performed to extract anti-proton inelastic cross-sections, in order to confirm the analysis procedure and to have a benchmark.

The analysis consisted in first measuring raw primary (anti-)particles yields in order to construct anti-particle to particle ratios as a function of momentum. Such ratios already have clues about absorption in the detector material. Comparisons to Monte Carlo simulations using different Geant versions for propagation through detector material give more precise information about the inelastic $\bar{\mathrm{p}}$ and $\bar{\mathrm{d}}$ cross-sections. Geant4-based simulations are found to be in better agreement with experimental data. The final piece which allowed the extraction of $\sigma_{\mathrm{inel}}(\bar{\mathrm{d}})$ is the conclusion about linear dependence between $\sigma_{\mathrm{inel}}(\bar{\mathrm{d}})$ and the raw primary $\bar{\mathrm{d}}/\mathrm{d}$ ratio.

The constraints for $\sigma_{\mathrm{inel}}(\bar{\mathrm{p}})$ were extracted for momentum range $0.7 < p < 4.0$ GeV/c and are consistent with the Geant4 parametrization which describe well the existing data. Those for $\sigma_{\mathrm{inel}}(\bar{\mathrm{d}})$ were extracted for the range $1.4 < p < 4.0$ GeV/c and are the first experimental constraints for such low momentum range. As expected, comparisons of the results between two collision systems also conclude that there is no special dependance with respect to this. The results in p–Pb collisions have been discussed within the ALICE collaboration and were approved as preliminary physics results, as indicated on the plots in chapter 5 and chapter 6.

Since the TOF detector is able to identify (anti-)deuterons with momenta down to ~ 0.9 GeV/c, future analyses could cover a wider momentum range. Even for lower momenta, down to ~ 0.5 GeV/c, $\sigma_{\mathrm{inel}}(\bar{\mathrm{d}})$ could be extracted by using the full-scale ALICE simulations. In order to analyse anti-particles with higher atomic number in the same way, whole LHC Run 2 statistics could be enough to make quantitative conclusions. Such (anti-)particles, for example $\overline{^3\mathrm{He}}$ and $\overline{^4\mathrm{He}}$, have the advantage that their TPC $\mathrm{d}E/\mathrm{d}x$ signal can be well separated from other particle species. This would also lead to a different analysis, where spectra could be analysed separately for particles and anti-particles before and after the TRD detector. The structure of such an analysis would be to perform TPC only PID and TPC+TOF PID in the same momentum range and compare the resulting yields. This can also be implemented for $\sigma_{\mathrm{inel}}(\bar{\mathrm{d}})$ analysis, it is however limited to the momentum range $0.9 < p < 1.4$ GeV/c because for lower momenta TOF information is not available and for higher momenta TPC only PID is not possible due to high contamination from other

(anti-)particles. Finally, the presented results and future constraints of σ_{inel} of various anti-nuclei are expected to contribute to a better understanding of anti-deuteron absorption in interstellar medium, which would be a crucial step towards precise calculations of primary and secondary cosmic anti-deuteron fluxes near Earth and thus support the indirect search for dark matter.

A. TOF squared-mass fits

Following figures show fits to TOF m^2 distributions of (anti-)proton and (anti-)deuteron candidates in all analysed momentum bins. The fit procedure is described in section 3.3.

A.1. TOF m^2 fits for proton

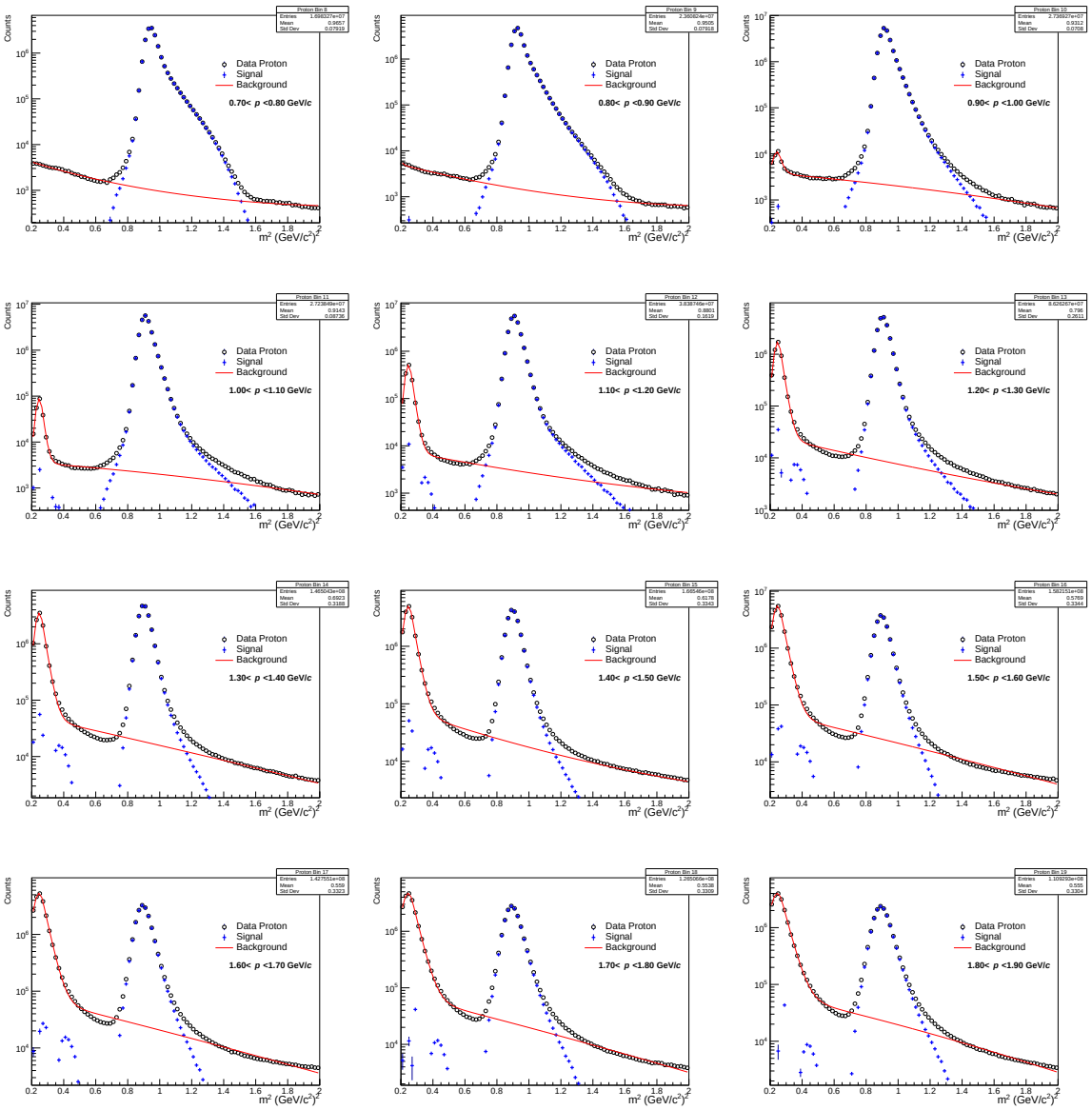

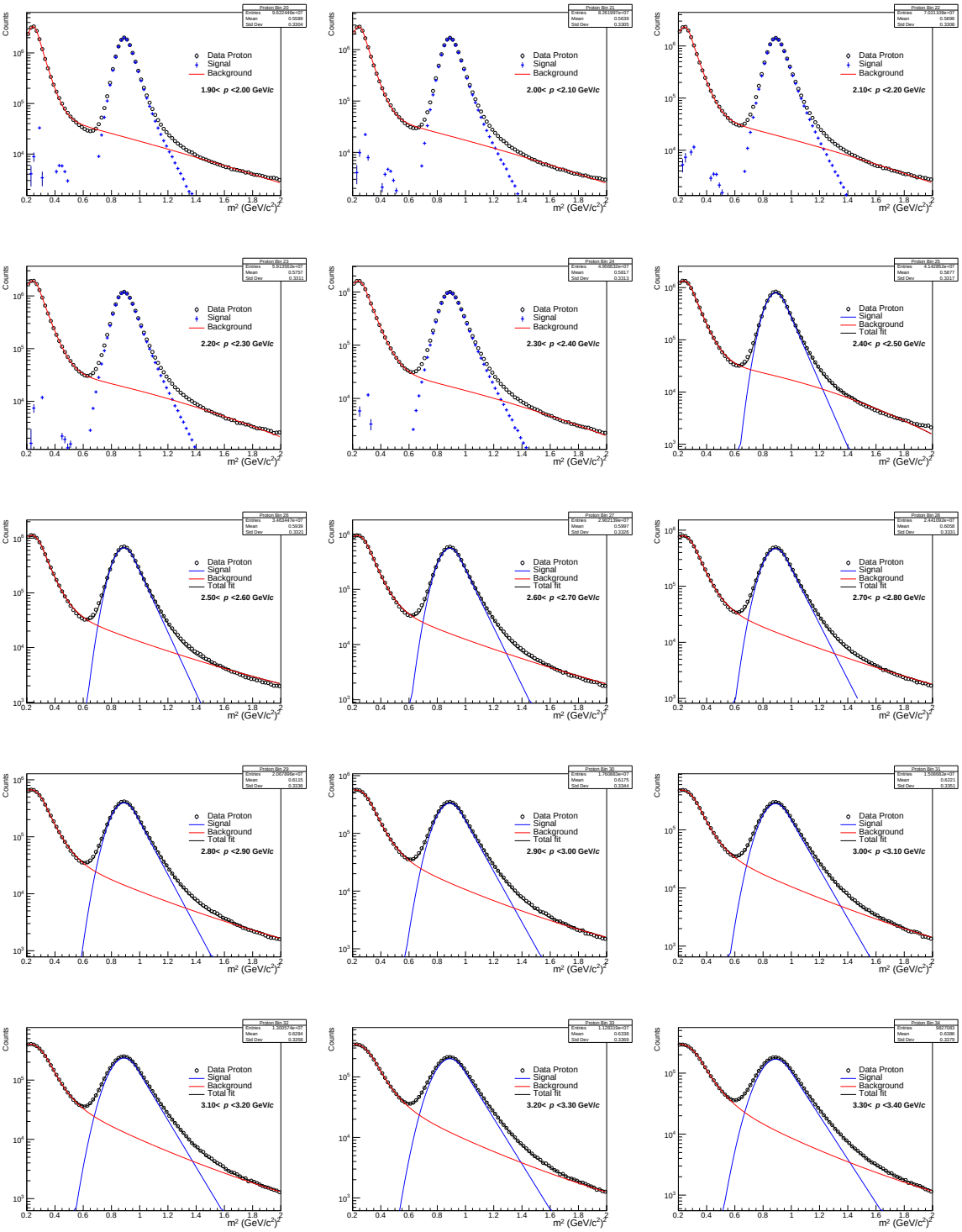
Data Proton
Signal
Background
Total fit
1.90< p <2.00 GeV/c
2.00< p <2.10 GeV/c
2.10< p <2.20 GeV/c
2.20< p <2.30 GeV/c
2.30< p <2.40 GeV/c
2.40< p <2.50 GeV/c
2.50< p <2.60 GeV/c
2.60< p <2.70 GeV/c
2.70< p <2.80 GeV/c
2.80< p <2.90 GeV/c
2.90< p <3.00 GeV/c
3.00< p <3.10 GeV/c
3.10< p <3.20 GeV/c
3.20< p <3.30 GeV/c
3.30< p <3.40 GeV/c
Counts
m² (GeV/c²)²

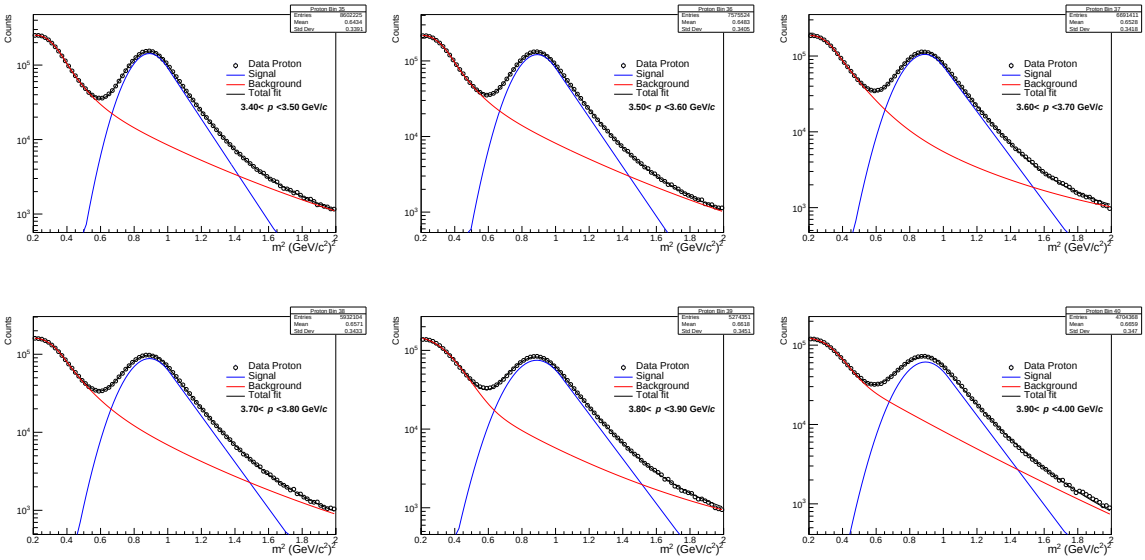

Figure A.1.: Fits to TOF m^2 distributions of proton candidates in all analysed momentum bins.

A.2. TOF m^2 fits for anti-proton

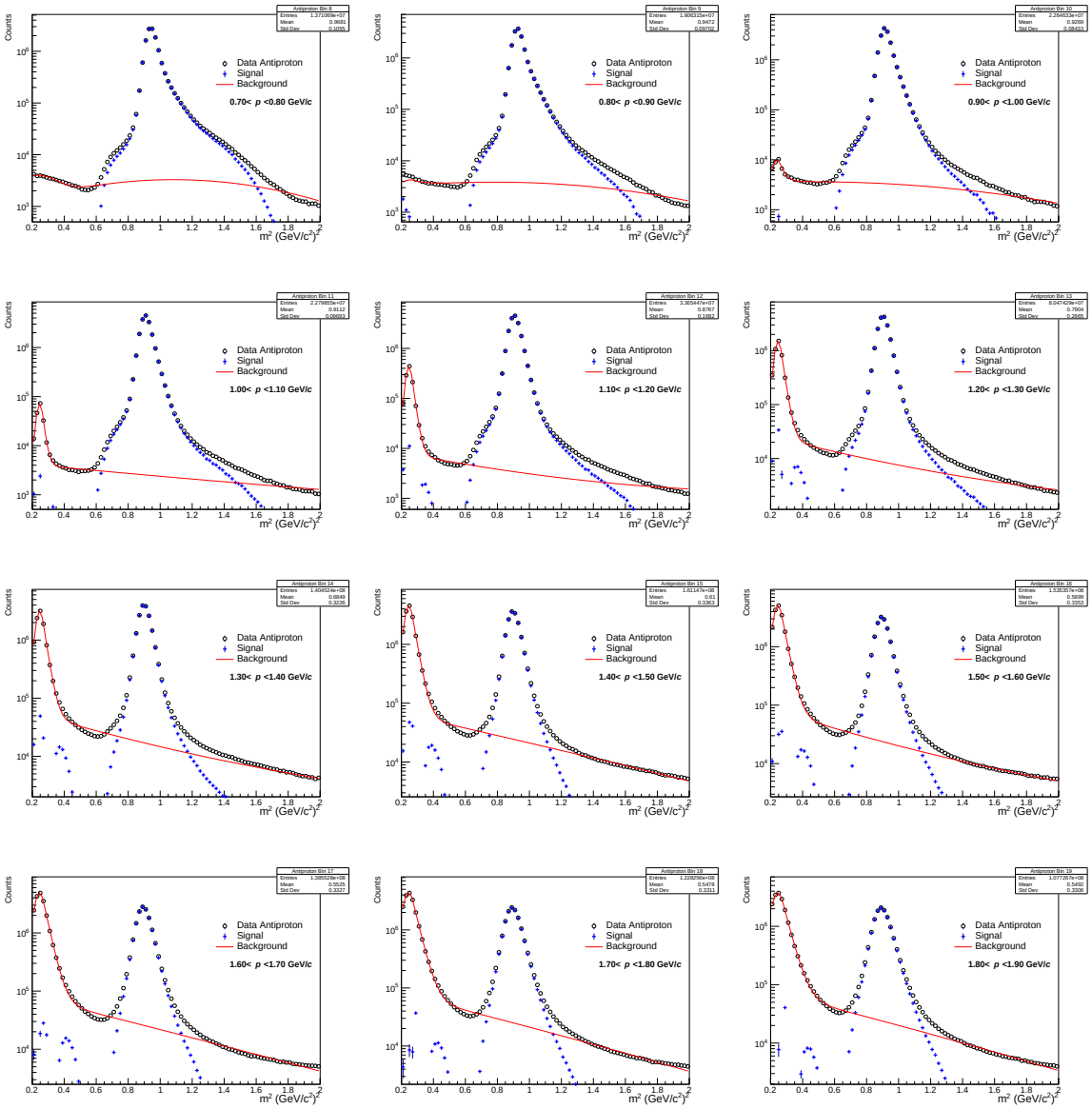

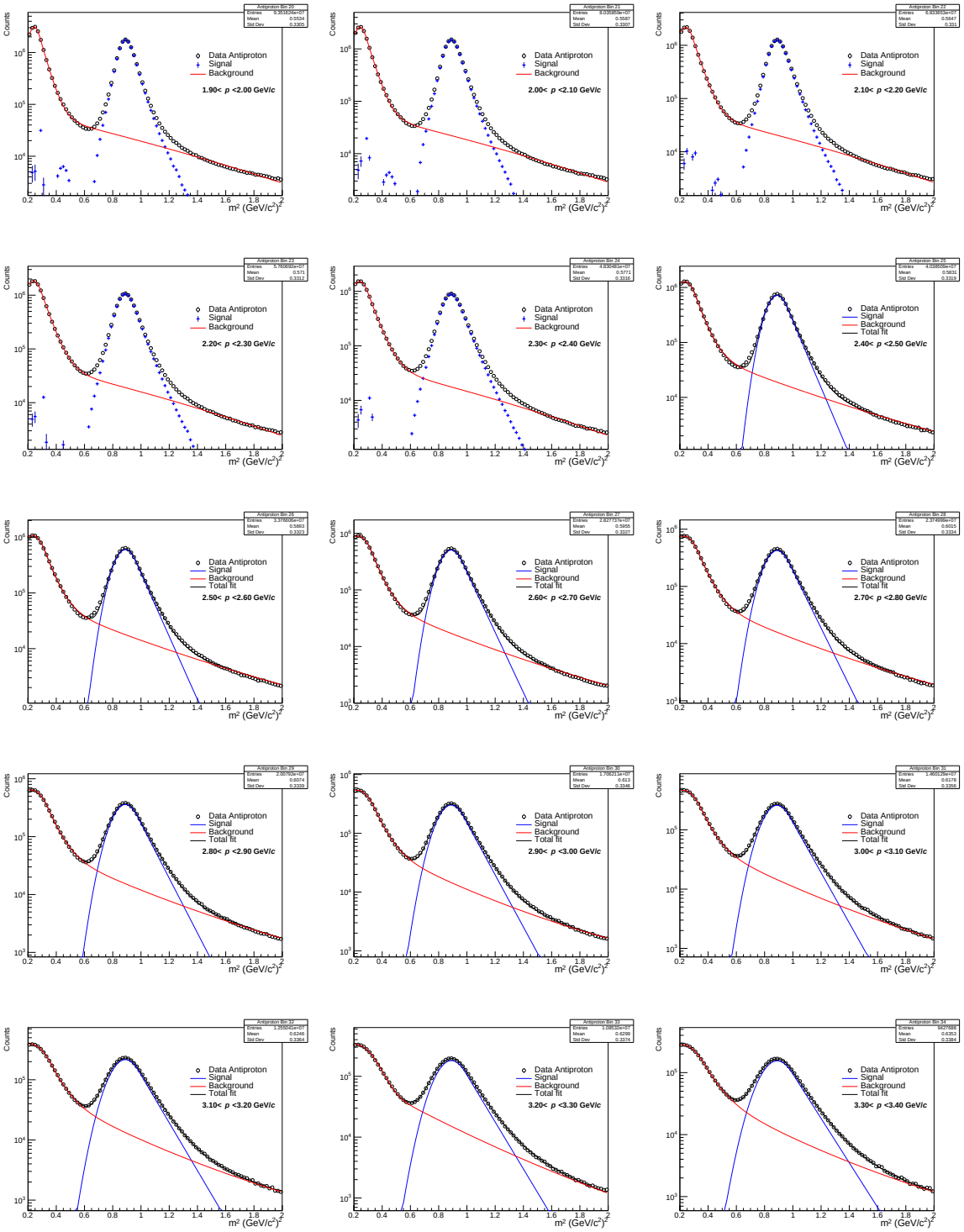
Data Antiproton
Signal
Background
Total fit
1.90< p <2.00 GeV/c
2.00< p <2.10 GeV/c
2.10< p <2.20 GeV/c
2.20< p <2.30 GeV/c
2.30< p <2.40 GeV/c
2.40< p <2.50 GeV/c
2.50< p <2.60 GeV/c
2.60< p <2.70 GeV/c
2.70< p <2.80 GeV/c
2.80< p <2.90 GeV/c
2.90< p <3.00 GeV/c
3.00< p <3.10 GeV/c
3.10< p <3.20 GeV/c
3.20< p <3.30 GeV/c
3.30< p <3.40 GeV/c
Counts
m² (GeV/c²)²

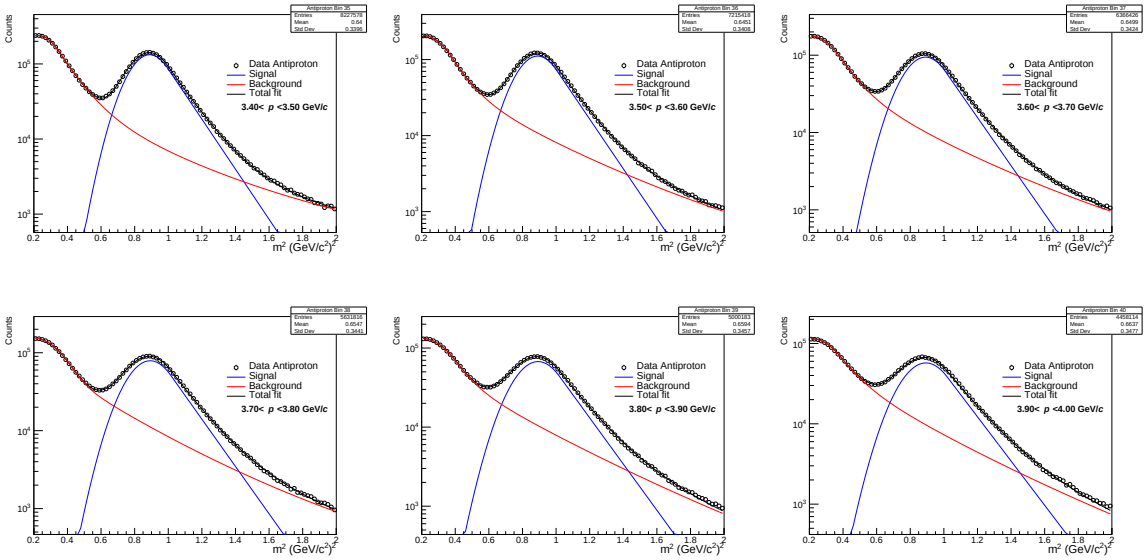

Figure A.2.: Fits to TOF m^2 distributions of (anti-)proton candidates in all analysed momentum bins.

A.3. TOF m^2 fits for deuteron

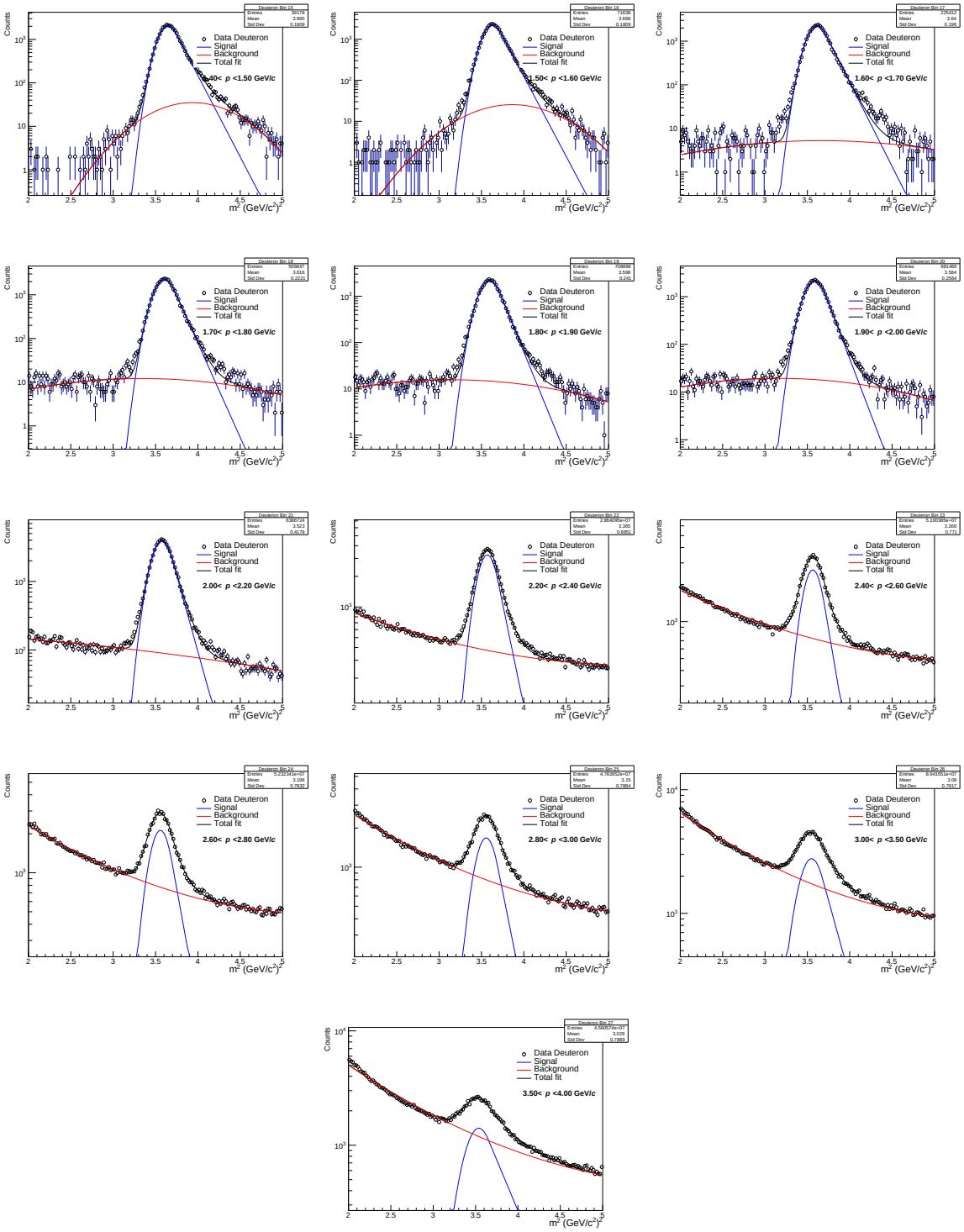

Figure A.3.: Fits to TOF m^2 distributions of deuteron candidates in all analysed momentum bins.

A.4. TOF m^2 fits for anti-deuteron

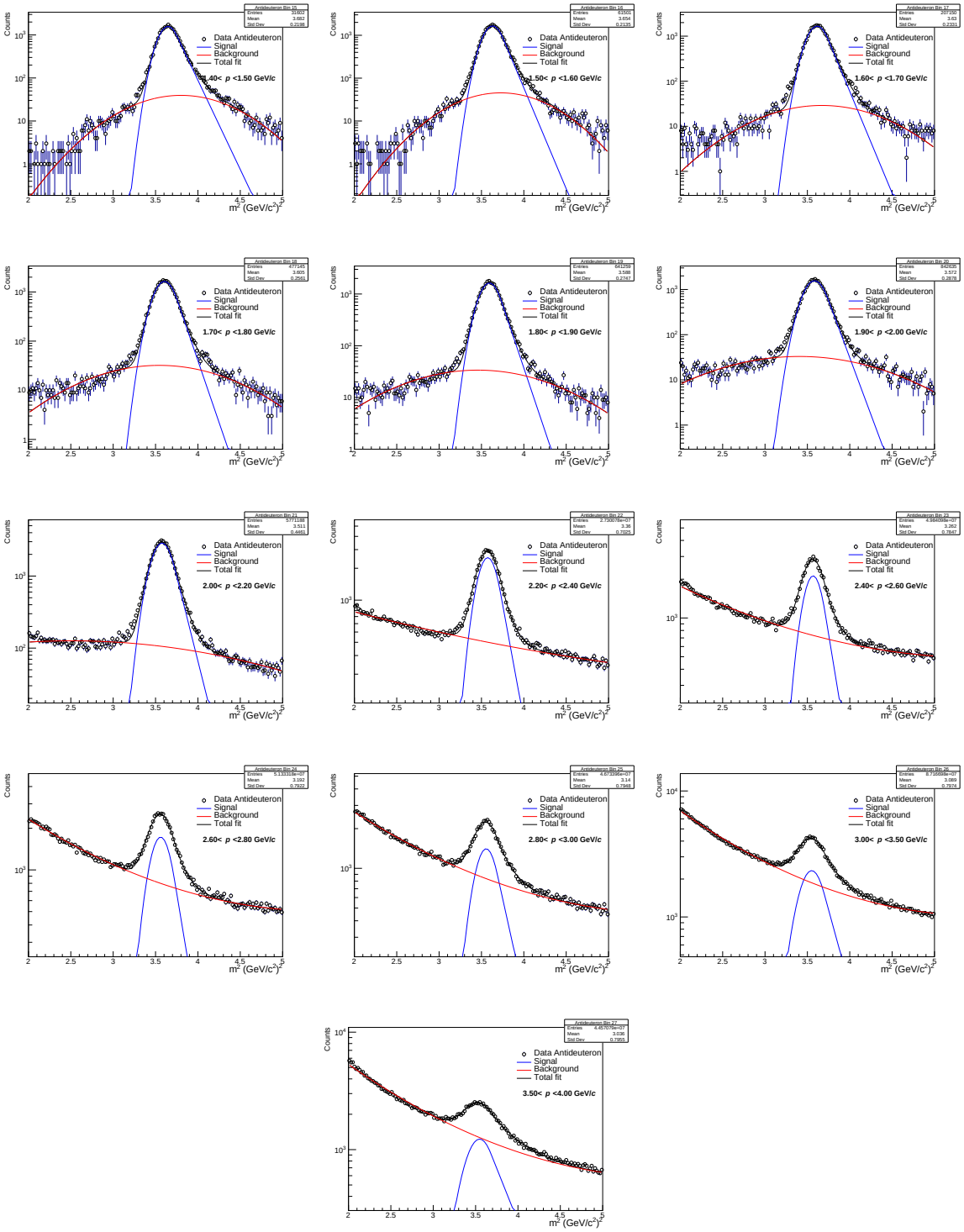

Figure A.4.: Fits to TOF m^2 distributions of (anti-)deuteron candidates in all analysed momentum bins.

B. Template fits

Following figures show template fits to DCA_{xy} distributions of (anti-)proton and deuteron candidates in different momentum bins. The fit procedure is described in section 3.4.

B.1. Template fits for proton

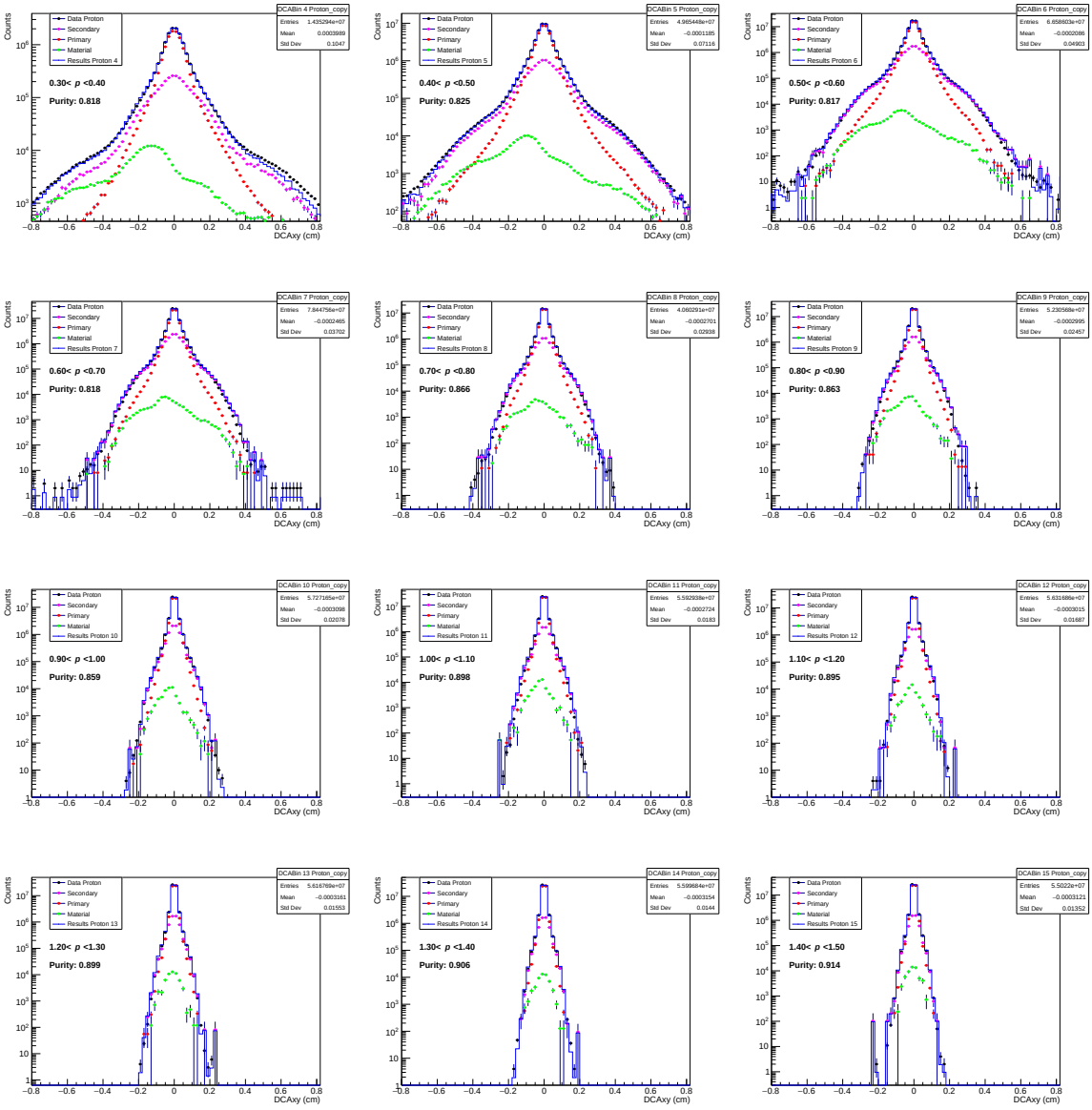

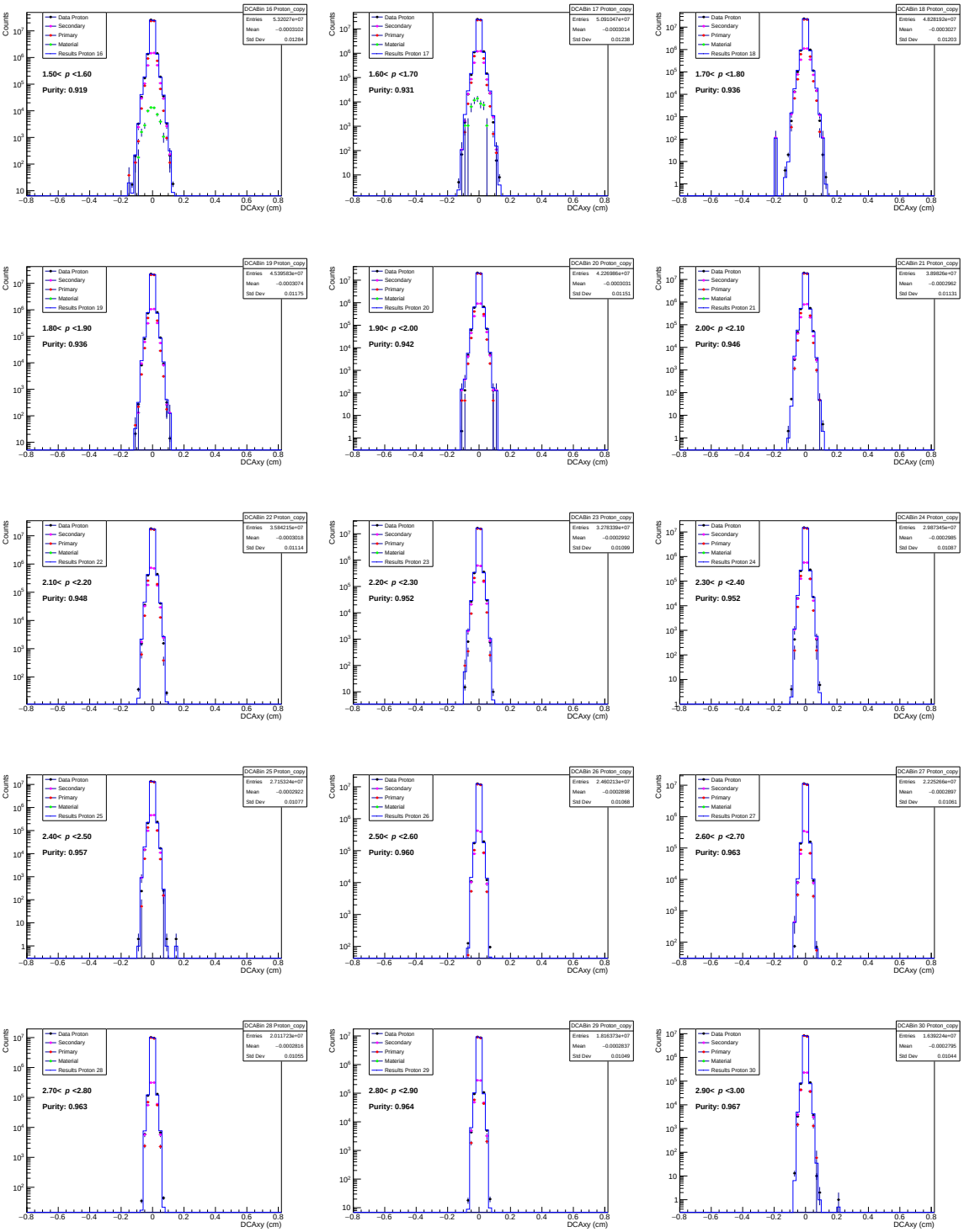
Data Proton
Secondary
Primary
Material
Results Proton 16
1.50< p <1.60
Purity: 0.919
Data Proton
Secondary
Primary
Material
Results Proton 17
1.60< p <1.70
Purity: 0.931
Data Proton
Secondary
Primary
Material
Results Proton 18
1.70< p <1.80
Purity: 0.936
Data Proton
Secondary
Primary
Material
Results Proton 19
1.80< p <1.90
Purity: 0.936
Data Proton
Secondary
Primary
Material
Results Proton 20
1.90< p <2.00
Purity: 0.942
Data Proton
Secondary
Primary
Material
Results Proton 21
2.00< p <2.10
Purity: 0.946
Data Proton
Secondary
Primary
Material
Results Proton 22
2.10< p <2.20
Purity: 0.948
Data Proton
Secondary
Primary
Material
Results Proton 23
2.20< p <2.30
Purity: 0.952
Data Proton
Secondary
Primary
Material
Results Proton 24
2.30< p <2.40
Purity: 0.952
Data Proton
Secondary
Primary
Material
Results Proton 25
2.40< p <2.50
Purity: 0.957
Data Proton
Secondary
Primary
Material
Results Proton 26
2.50< p <2.60
Purity: 0.960
Data Proton
Secondary
Primary
Material
Results Proton 27
2.60< p <2.70
Purity: 0.963
Data Proton
Secondary
Primary
Material
Results Proton 28
2.70< p <2.80
Purity: 0.963
Data Proton
Secondary
Primary
Material
Results Proton 29
2.80< p <2.90
Purity: 0.964
Data Proton
Secondary
Primary
Material
Results Proton 30
2.90< p <3.00
Purity: 0.967
Counts
DCAxy (cm)

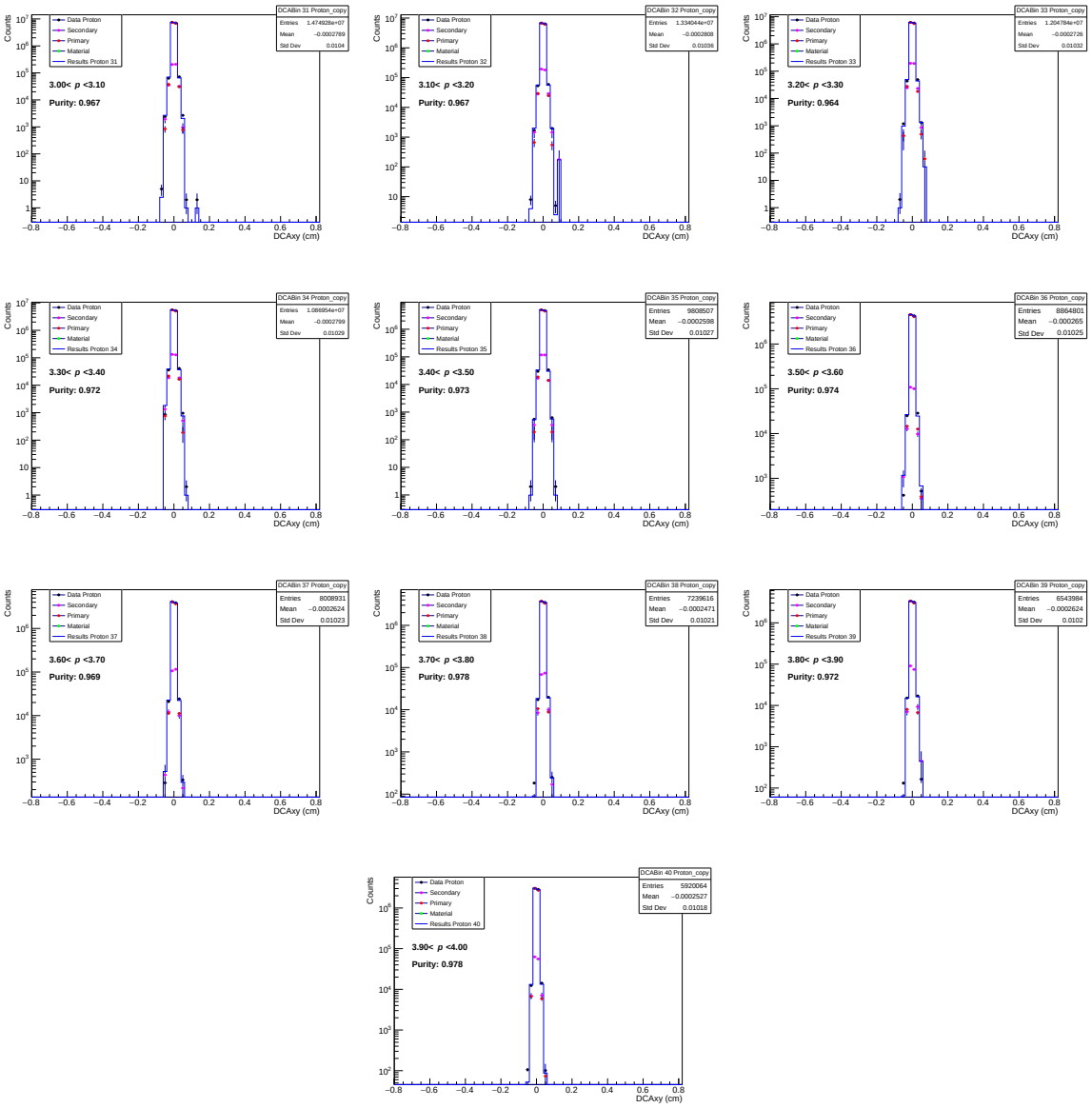

Figure B.1.: DCA_{xy} template fits of proton candidates in different momentum bins.

B.2. Template fits for anti-proton

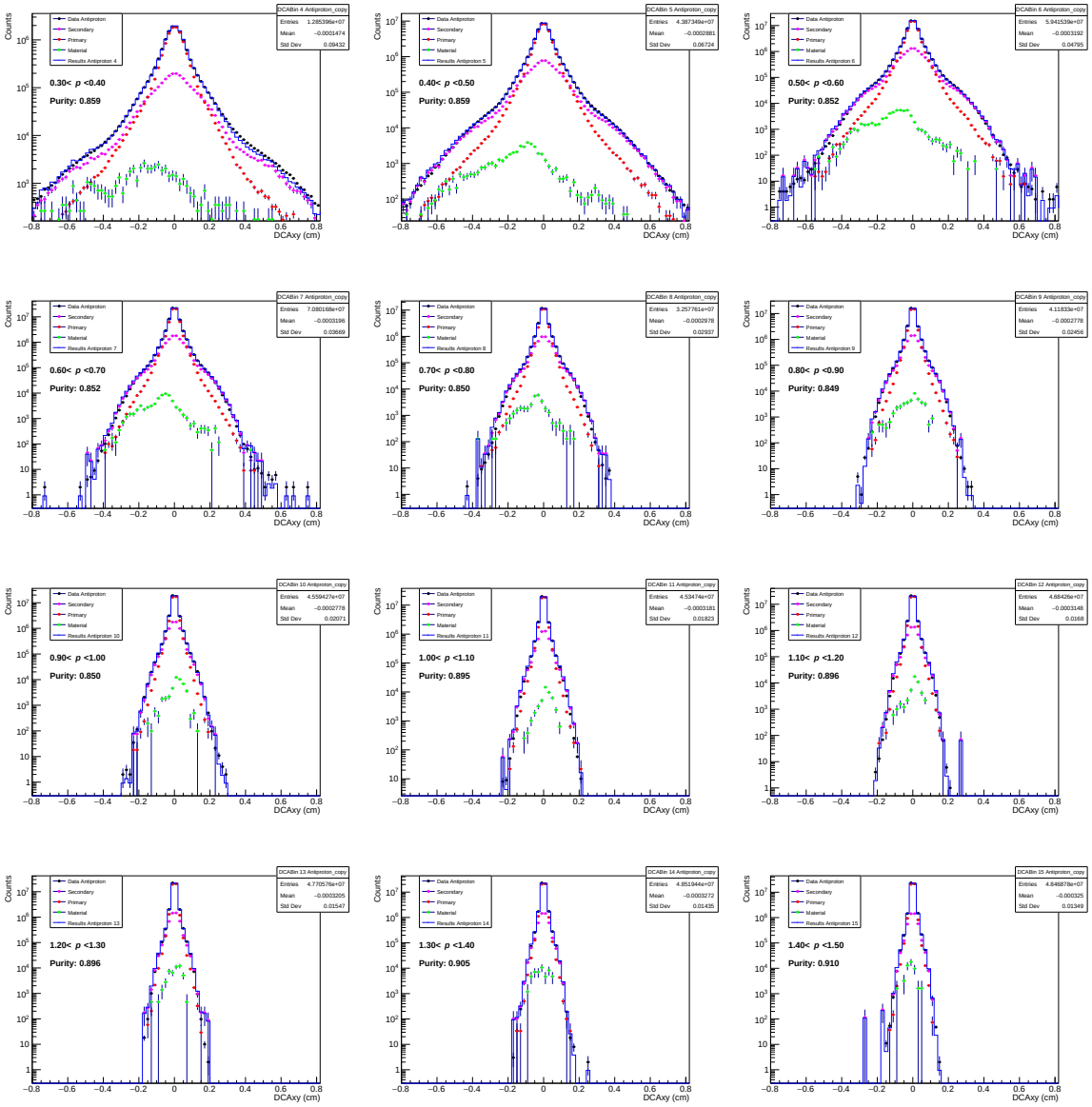

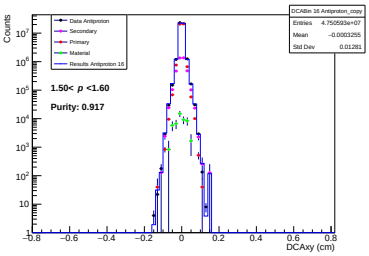
1.50< p <1.60
Purity: 0.917
Counts
DCAxy (cm)

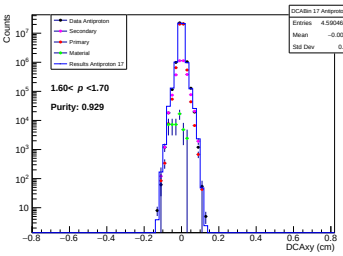
1.60< p <1.70
Purity: 0.929
Counts
DCAxy (cm)

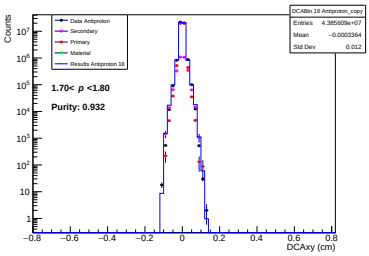
1.70< p <1.80
Purity: 0.932
Counts
DCAxy (cm)

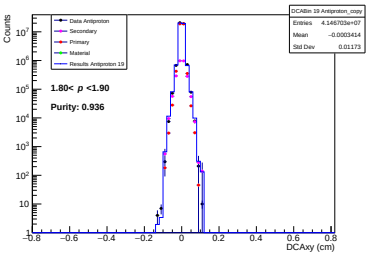
1.80< p <1.90
Purity: 0.936
Counts
DCAxy (cm)

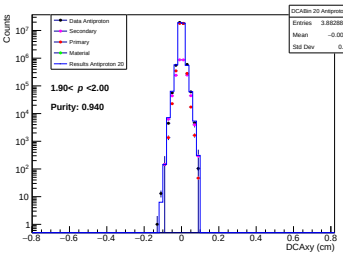
1.90< p <2.00
Purity: 0.940
Counts
DCAxy (cm)

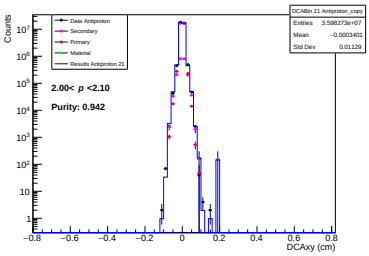
2.00< p <2.10
Purity: 0.942
Counts
DCAxy (cm)

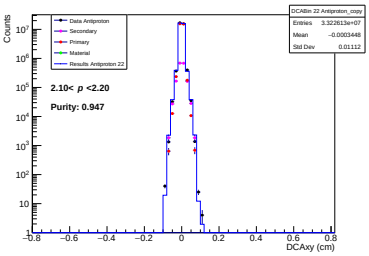
2.10< p <2.20
Purity: 0.947
Counts
DCAxy (cm)

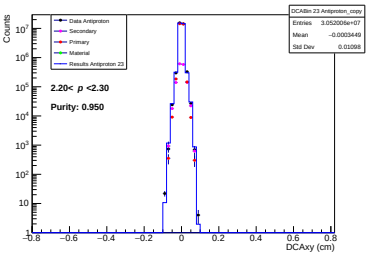
2.20< p <2.30
Purity: 0.950
Counts
DCAxy (cm)

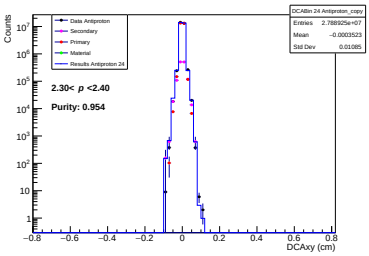
2.30< p <2.40
Purity: 0.954
Counts
DCAxy (cm)

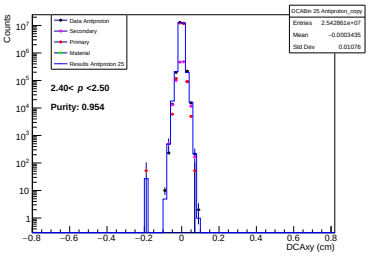
2.40< p <2.50
Purity: 0.954
Counts
DCAxy (cm)

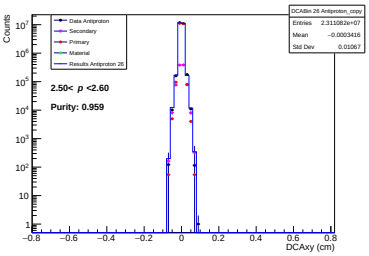
2.50< p <2.60
Purity: 0.959
Counts
DCAxy (cm)

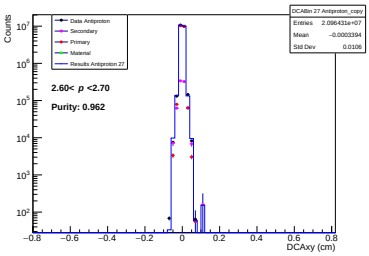
2.60< p <2.70
Purity: 0.962
Counts
DCAxy (cm)

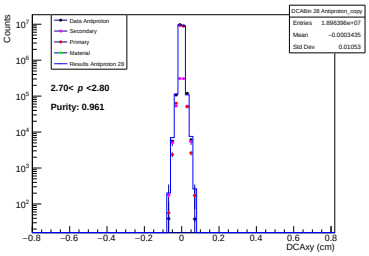
2.70< p <2.80
Purity: 0.961
Counts
DCAxy (cm)

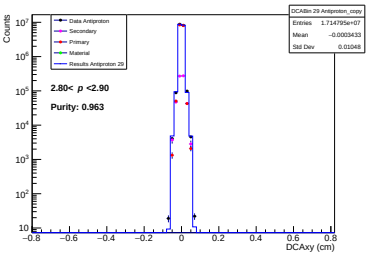
2.80< p <2.90
Purity: 0.963
Counts
DCAxy (cm)

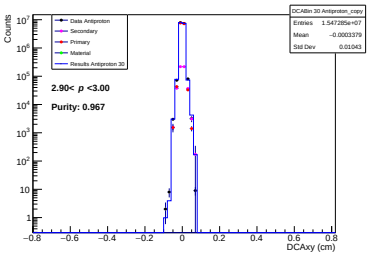
2.90< p <3.00
Purity: 0.967
Counts
DCAxy (cm)

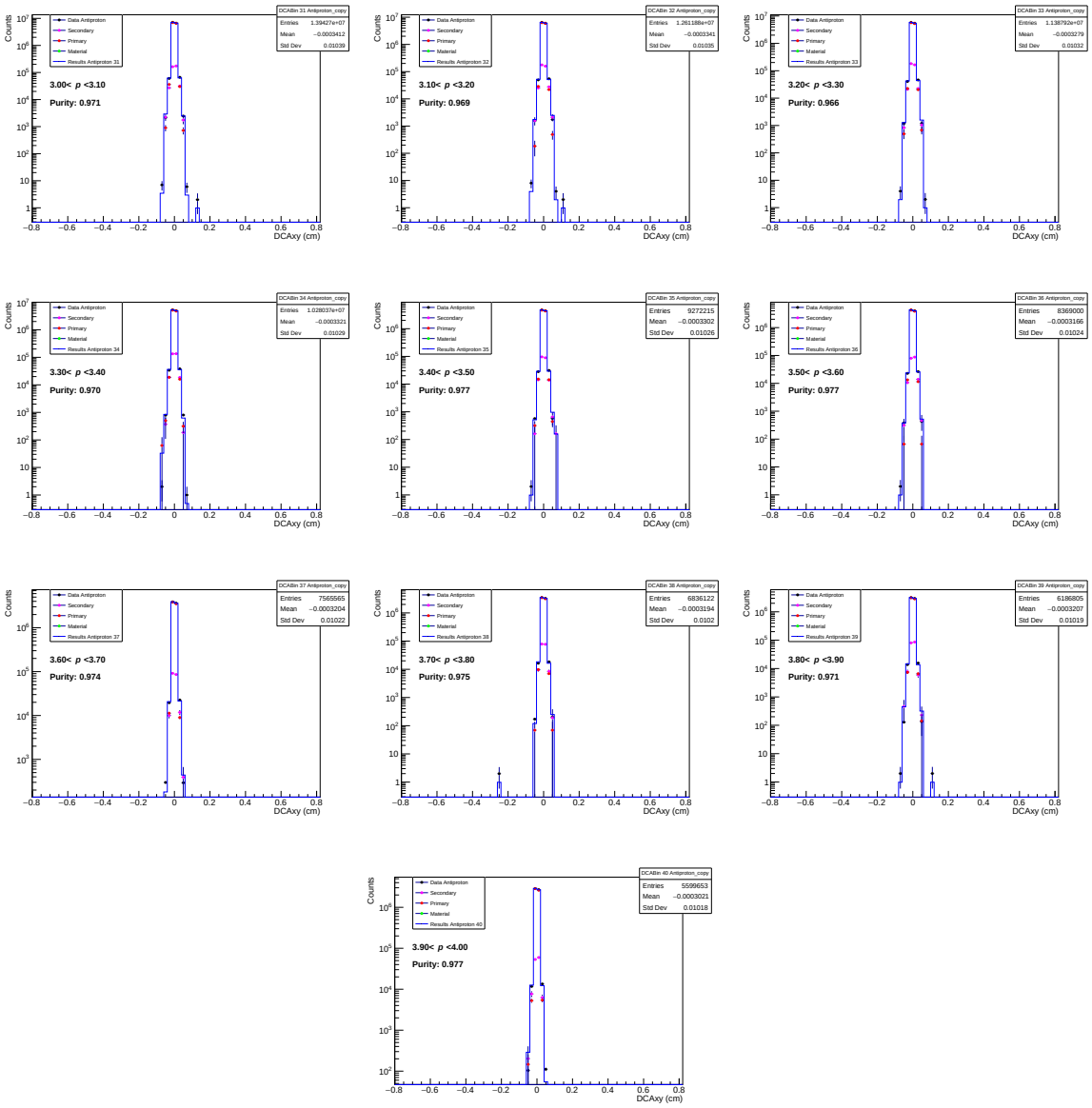

Figure B.2.: DCA_{xy} template fits of anti-proton candidates in different momentum bins.

B.3. Template fits for deuteron

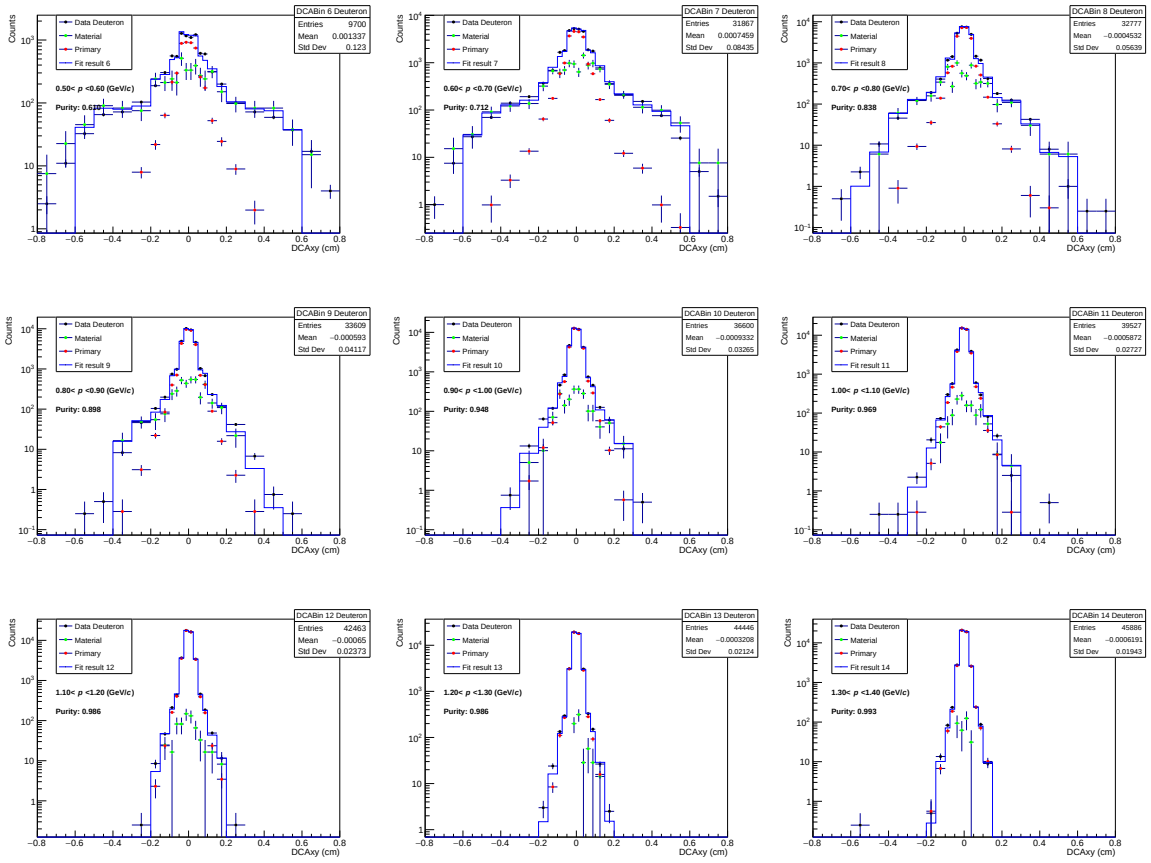

Figure B.3.: DCA_{xy} template fits of deuteron candidates in different momentum bins.

C. Linear fits to ratios with varied cross-sections

Following figures show $\bar{\mathrm{p}}/\mathrm{p}$ and $\bar{\mathrm{d}}/\mathrm{d}$ ratios as a function of re-scaling factors in all analysed momentum bins. The interception of the black line, which is a linear fit of the simple Geant4 simulation data, with the blue and red lines correspond to the re-scaling factor applied to $\sigma_{\mathrm{inel}}(\bar{\mathrm{p}})$ and $\sigma_{\mathrm{inel}}(\bar{\mathrm{d}})$.

C.1. Anti-proton to proton ratios

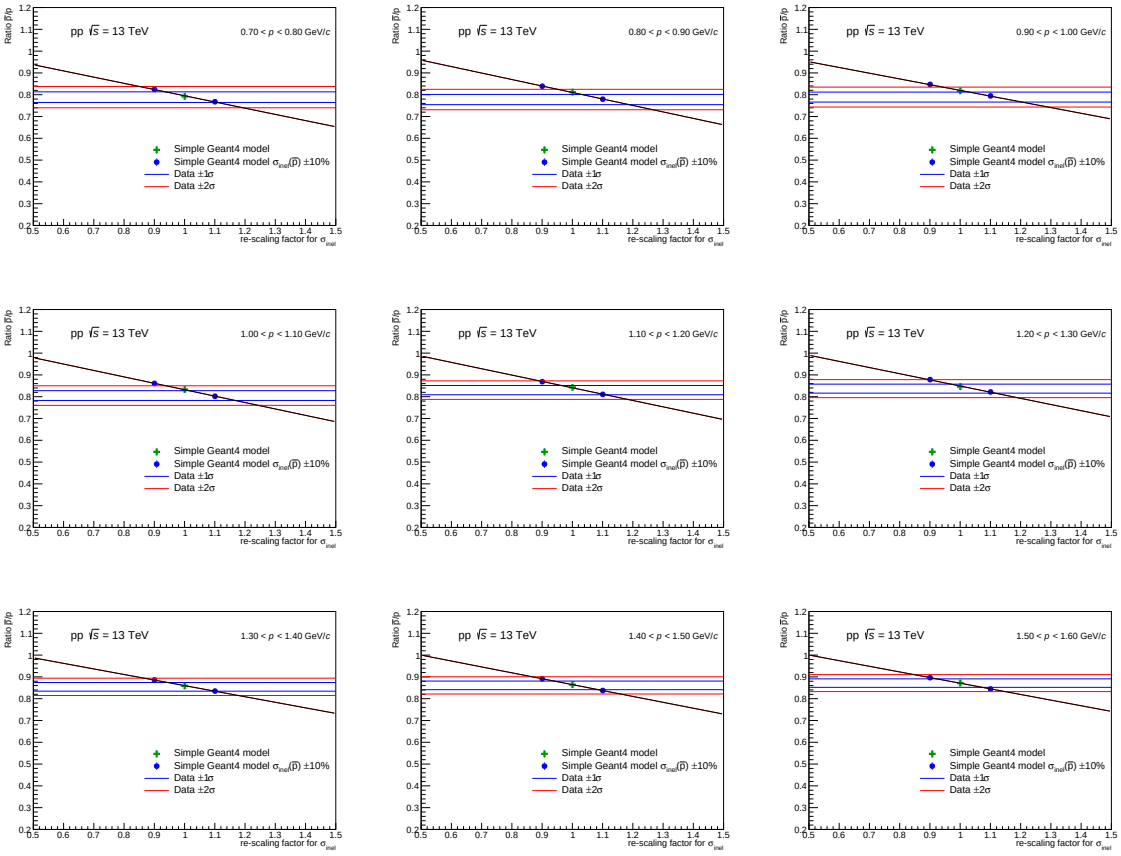

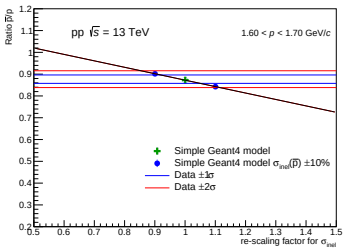
pp $\sqrt{s}$ = 13 TeV
1.60 < p < 1.70 GeV/c
Simple Geant4 model
Simple Geant4 model $\sigma_{inel}(\bar{p})$ ±10%
Data ±1σ
Data ±2σ
Ratio $\bar{p}/p$
re-scaling factor for σ_{inel}

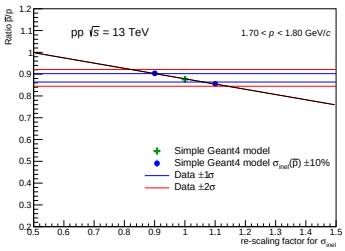
pp $\sqrt{s}$ = 13 TeV
1.70 < p < 1.80 GeV/c
Simple Geant4 model
Simple Geant4 model $\sigma_{inel}(\bar{p})$ ±10%
Data ±1σ
Data ±2σ
Ratio $\bar{p}/p$
re-scaling factor for σ_{inel}

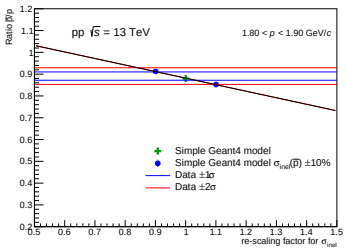
pp $\sqrt{s}$ = 13 TeV
1.80 < p < 1.90 GeV/c
Simple Geant4 model
Simple Geant4 model $\sigma_{inel}(\bar{p})$ ±10%
Data ±1σ
Data ±2σ
Ratio $\bar{p}/p$
re-scaling factor for σ_{inel}

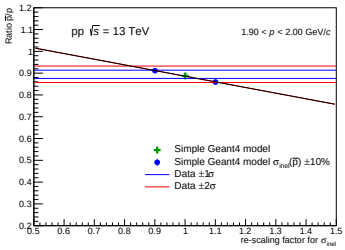
pp $\sqrt{s}$ = 13 TeV
1.90 < p < 2.00 GeV/c
Simple Geant4 model
Simple Geant4 model $\sigma_{inel}(\bar{p})$ ±10%
Data ±1σ
Data ±2σ
Ratio $\bar{p}/p$
re-scaling factor for σ_{inel}

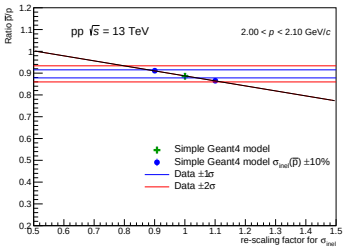
pp $\sqrt{s}$ = 13 TeV
2.00 < p < 2.10 GeV/c
Simple Geant4 model
Simple Geant4 model $\sigma_{inel}(\bar{p})$ ±10%
Data ±1σ
Data ±2σ
Ratio $\bar{p}/p$
re-scaling factor for σ_{inel}

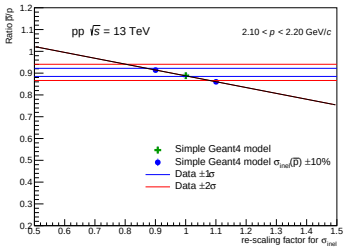
pp $\sqrt{s}$ = 13 TeV
2.10 < p < 2.20 GeV/c
Simple Geant4 model
Simple Geant4 model $\sigma_{inel}(\bar{p})$ ±10%
Data ±1σ
Data ±2σ
Ratio $\bar{p}/p$
re-scaling factor for σ_{inel}

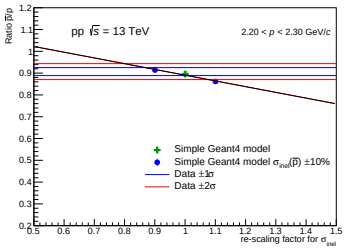
pp $\sqrt{s}$ = 13 TeV
2.20 < p < 2.30 GeV/c
Simple Geant4 model
Simple Geant4 model $\sigma_{inel}(\bar{p})$ ±10%
Data ±1σ
Data ±2σ
Ratio $\bar{p}/p$
re-scaling factor for σ_{inel}

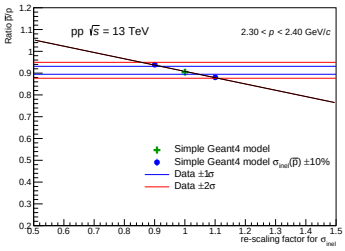
pp $\sqrt{s}$ = 13 TeV
2.30 < p < 2.40 GeV/c
Simple Geant4 model
Simple Geant4 model $\sigma_{inel}(\bar{p})$ ±10%
Data ±1σ
Data ±2σ
Ratio $\bar{p}/p$
re-scaling factor for σ_{inel}

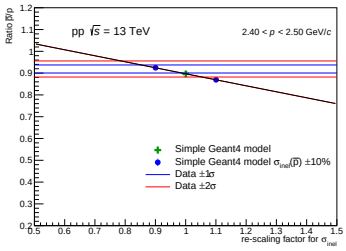
pp $\sqrt{s}$ = 13 TeV
2.40 < p < 2.50 GeV/c
Simple Geant4 model
Simple Geant4 model $\sigma_{inel}(\bar{p})$ ±10%
Data ±1σ
Data ±2σ
Ratio $\bar{p}/p$
re-scaling factor for σ_{inel}

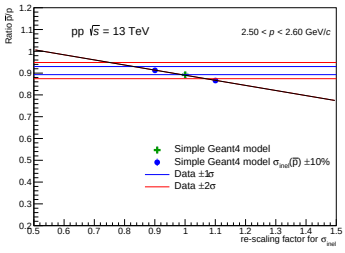
pp $\sqrt{s}$ = 13 TeV
2.50 < p < 2.60 GeV/c
Simple Geant4 model
Simple Geant4 model $\sigma_{inel}(\bar{p})$ ±10%
Data ±1σ
Data ±2σ
Ratio $\bar{p}/p$
re-scaling factor for σ_{inel}

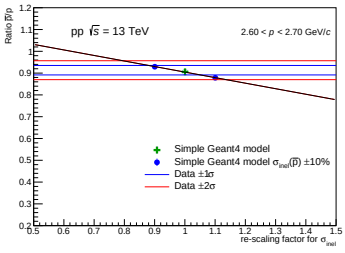
pp $\sqrt{s}$ = 13 TeV
2.60 < p < 2.70 GeV/c
Simple Geant4 model
Simple Geant4 model $\sigma_{inel}(\bar{p})$ ±10%
Data ±1σ
Data ±2σ
Ratio $\bar{p}/p$
re-scaling factor for σ_{inel}

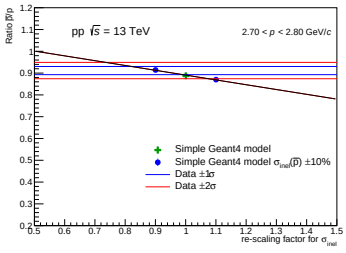
pp $\sqrt{s}$ = 13 TeV
2.70 < p < 2.80 GeV/c
Simple Geant4 model
Simple Geant4 model $\sigma_{inel}(\bar{p})$ ±10%
Data ±1σ
Data ±2σ
Ratio $\bar{p}/p$
re-scaling factor for σ_{inel}

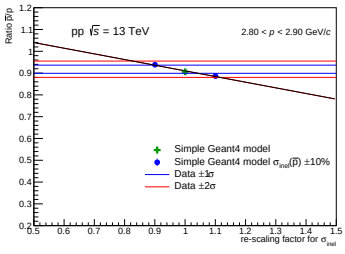
pp $\sqrt{s}$ = 13 TeV
2.80 < p < 2.90 GeV/c
Simple Geant4 model
Simple Geant4 model $\sigma_{inel}(\bar{p})$ ±10%
Data ±1σ
Data ±2σ
Ratio $\bar{p}/p$
re-scaling factor for σ_{inel}

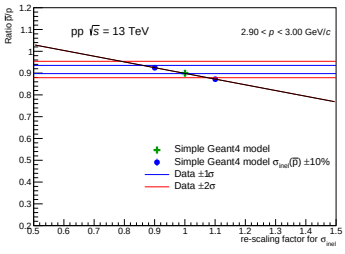
pp $\sqrt{s}$ = 13 TeV
2.90 < p < 3.00 GeV/c
Simple Geant4 model
Simple Geant4 model $\sigma_{inel}(\bar{p})$ ±10%
Data ±1σ
Data ±2σ
Ratio $\bar{p}/p$
re-scaling factor for σ_{inel}

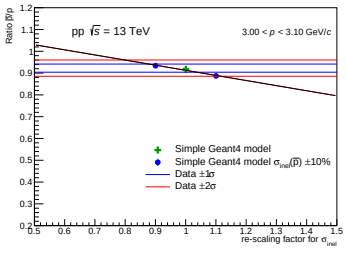
pp $\sqrt{s}$ = 13 TeV
3.00 < p < 3.10 GeV/c
Simple Geant4 model
Simple Geant4 model $\sigma_{inel}(\bar{p})$ ±10%
Data ±1σ
Data ±2σ
Ratio $\bar{p}/p$
re-scaling factor for σ_{inel}

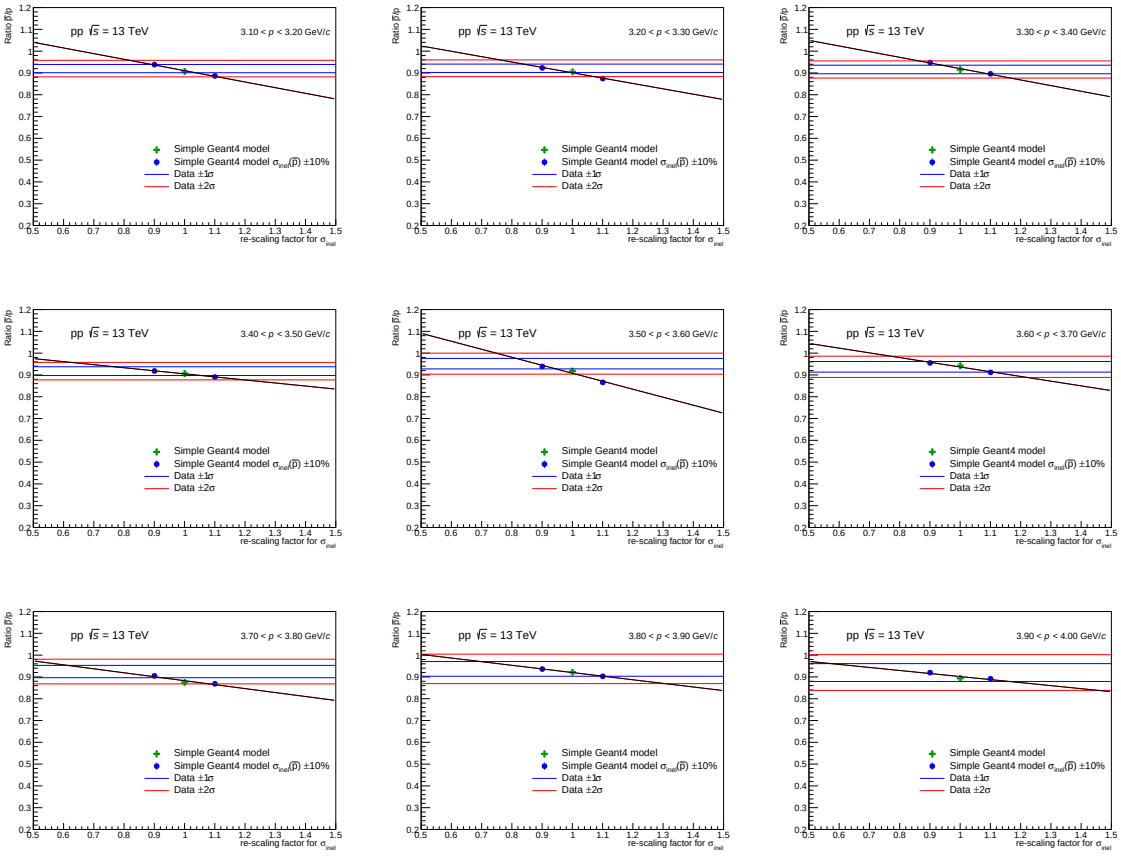

Figure C.1.: $\bar{\mathrm{p}}/\mathrm{p}$ ratio as a function of re-scaling factor applied to $\sigma_{\mathrm{inel}}(\bar{\mathrm{p}})$ in all analysed momentum bins.

C.2. Anti-deuteron to deuteron ratios

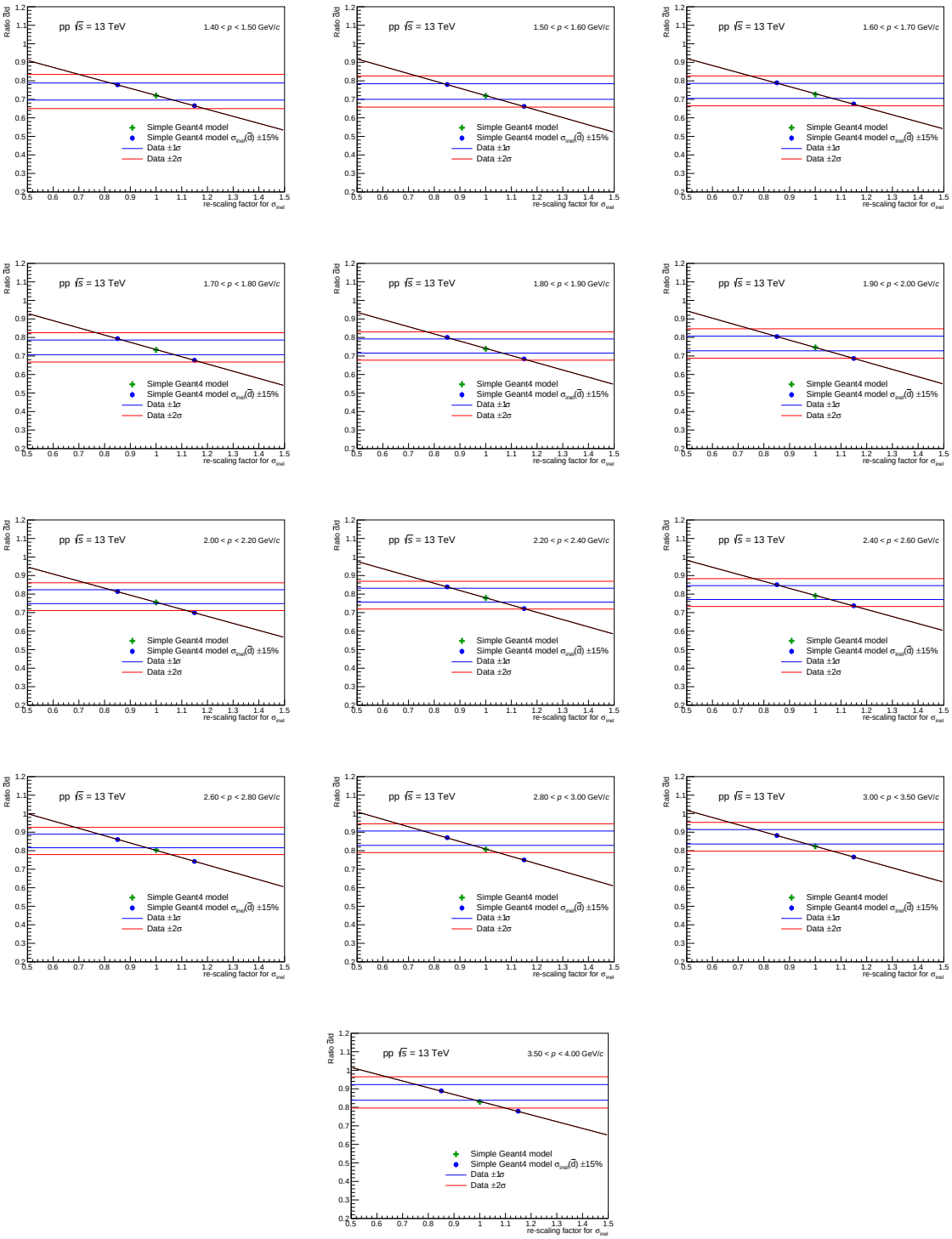

Figure C.2.: $\bar{\mathrm{d}}/\mathrm{d}$ ratio as a function of re-scaling factor applied to $\sigma_{\mathrm{inel}}(\bar{\mathrm{d}})$ in all analysed momentum bins.

Bibliography

[1] Edwin Hubble and Milton L Humason. The velocity-distance relation among extra-galactic nebulae. *The Astrophysical Journal*, 74:43, 1931.

[2] Fritz Zwicky. Die rotverschiebung von extragalaktischen nebeln. *Helvetica Physica Acta*, 6:110–127, 1933.

[3] Vera C Rubin, Norbert Thonnard, et al. Motion of the galaxy and the local group determined from the velocity anisotropy of distant sc i galaxies. ii-the analysis for the motion. *The Astronomical Journal*, 81:719–737, 1976.

[4] Planck Collaboration. Planck 2013 results. xvi. cosmological parameters. *Astronomy & Astrophysics*, 571:A16, 2014.

[5] Volker Springel, Simon DM White, Adrian Jenkins, et al. Simulating the joint evolution of quasars, galaxies and their large-scale distribution. *arXiv preprint astro-ph/0504097*, 2005.

[6] Lisa Randall and Weishuang Linda Xu. Searching for dark photon dark matter with cosmic ray antideuterons. *arXiv preprint arXiv:1910.14669*, 2019.

[7] Fiorenza Donato, Nicolao Fornengo, and Pierre Salati. Antideuterons as a signature of supersymmetric dark matter. *Physical Review D*, 62(4):043003, 2000.

[8] R Bird, T Aramaki, et al. Gaps: Searching for dark matter using antinuclei in cosmic rays. *arXiv preprint arXiv:1908.03154*, 2019.

[9] Luísa Arruda, Fernando Barao, and Rui Pereira. Particle identification with the ams-02 rich detector: search for dark matter with antideuterons. *arXiv preprint arXiv:0710.0993*, 2007.

[10] S. P. Denisov et al. Measurements of anti-deuteron absorption and stripping cross sections at the momentum 13.3 gev/c. *Nucl. Phys.*, B31:253–260, 1971.

[11] Freddy Binon, SP Denisov, et al. Absorption cross-sections of 25 gev/c antideuterons in li, c, al, cu and pb. *Physics Letters B*, 31:230–232, 1970.

[12] Shreyasi Acharya et al. Production of deuterons, tritons, he 3 nuclei, and their antinuclei in p p collisions at $\sqrt{s}$= 0.9, 2.76, and 7 tev. *Physical Review C*, 97(2):024615, 2018.

[13] Owen Chamberlain, Emilio Segrè, Clyde Wiegand, and Thomas Ypsilantis. Observation of antiprotons. *Physical Review*, 100(3):947, 1955.

[14] Thomas Massam, Th Muller, B Righini, M Schneegans, and Antonino Zichichi. Experimental observation of antideuteron production. *Il Nuovo Cimento A (1965-1970)*, 63(1):10–14, 1965.

[15] G Brautti, Giuseppe Fidecaro, T Massam, M Morpurgo, Th Muller, G Petrucci, B Rocco, P Schiavon, M Schneegans, and A Ziohichi. A high-intensity, partially separated, beam of antiprotons and k-mesons. *Il Nuovo Cimento (1955-1965)*, 38(4):1861–1874, 1965.

[16] C Adler et al. $\bar{\mathrm{d}}$ and $\overline{^3\mathrm{he}}$ production in $\sqrt{s_{\mathrm{NN}}}$=130 gev au+au collisions. *Physical Review Letters*, 87(26):262301, 2001.

[17] H Agakishiev et al. Observation of the antimatter helium-4 nucleus. *Nature*, 473(7347):353, 2011.

[18] Shreyasi Acharya et al. Production of (anti-)^{3}He and (anti-)^{3}H in p-Pb collisions at $\sqrt{s_{\mathrm{NN}}}$ = 5.02 TeV. 2019.

[19] Shreyasi Acharya et al. Production of he4 and anti-he4 in pb–pb collisions at snn= 2.76 tev at the lhc. *Nuclear Physics A*, 971:1–20, 2018.

[20] J Cleymans, S Kabana, I Kraus, H Oeschler, K Redlich, and N Sharma. Antimatter production in proton-proton and heavy-ion collisions at ultrarelativistic energies. *Physical Review C*, 84(5):054916, 2011.

[21] R Brun, F Bruyant, M Maire, A C McPherson, and P Zanarini. *GEANT 3: user's guide Geant 3.10, Geant 3.11; rev. version.* CERN, Geneva, 1987.

[22] S. Agostinelli et al. Geant4—a simulation toolkit. *Nuclear Instruments and Methods in Physics Research Section A: Accelerators, Spectrometers, Detectors and Associated Equipment*, 506(3):250 – 303, 2003.

[23] Rene Brun, L Urban, Federico Carminati, et al. Geant: Detector description and simulation tool. Technical report, CERN, 1993.

[24] AA Moiseev and JF Ormes. Inelastic cross section for antihelium on nuclei: an empirical formula for use in the experiments to search for cosmic antimatter. *Astroparticle Physics*, 6(3-4):379–386, 1997.

[25] V Uzhinsky, John Apostolakis, A Galoyan, G Folger, VM Grichine, VN Ivanchenko, and DH Wright. Antinucleus–nucleus cross sections implemented in geant4. *Physics Letters B*, 705(3):235–239, 2011.

[26] Esma Mobs. The cern accelerator complex - august 2018. complexe des accélérateurs du cern - août 2018, Aug 2018.

[27] ALICE Collaboration. Performance of the ALICE Experiment at the CERN LHC. *Int. J. Mod. Phys.*, A29:1430044, 2014.

[28] Arturo Tauro. Alice schematics, May 2017.

[29] The ALICE colaboration et al. The ALICE experiment at the CERN LHC. *JINST*, 3:S08002, 2008.

[30] ALICE collaboration et al. Alignment of the alice inner tracking system with cosmic-ray tracks. *Journal of Instrumentation*, 5(03):P03003, 2010.

[31] J. Alme, Y. Andres, et al. The alice tpc, a large 3-dimensional tracking device with fast readout for ultra-high multiplicity events. page 55, 01 2010.

[32] Alice Collaboration et al. The alice transition radiation detector: construction, operation, and performance. *Nuclear Instruments and Methods in Physics Research Section A: Accelerators, Spectrometers, Detectors and Associated Equipment*, 881:88–127, 2018.

[33] ALICE Collaboration. Multiplicity dependence of (anti-)deuteron production in pp collisions at $\sqrt{s} = 7$ TeV. *Phys. Lett.*, B794:50–63, 2019.

[34] ALICE Collaboration. Mid-rapidity anti-baryon to baryon ratios in pp collisions at $\sqrt{s}$ = 0.9, 2.76 and 7 TeV measured by ALICE. *Eur. Phys. J.*, C73:2496, 2013.

[35] Torbjörn Sjöstrand et al. An Introduction to PYTHIA 8.2. *Comput. Phys. Commun.*, 191:159–177, 2015.

[36] Stefan Roesler, Ralph Engel, and Johannes Ranft. The monte carlo event generator dpmjet-iii. In *Advanced Monte Carlo for radiation physics, particle transport simulation and applications*, pages 1033–1038. Springer, 2001.

List of Figures

List of Tables

Acknowledgements

I would like to thank everyone who supported me during my thesis.
First of all, I would like to thank Prof. Laura Fabbietti, who gave me the chance to work in the anti-matter working group and actively involved me in science.
Many thanks to my supervisor Dr. Ivan Vorobyev. I am grateful for his contributions to p–Pb analysis and to the development of the simple Geant4 model. He has taught me useful tools for data analysis, specially things related to ALICE. Thank you for the stimulating discussions and that you always invested a lot of time to answer my questions.
I thank the whole working group for providing a great working atmosphere and for giving help whenever needed.
Furthermore, I would like to thank all my friends for your patience.
Thank you Aylin for your advices, your support and your never ending patience.
Last but not least, I thank my family for the support during many years of physics study.
Ich danke meinen Großeltern, meiner Schwester Lina, meinem Vater und meiner Mutter, ohne euch wäre das alles nicht möglich gewesen.

Erklärung

Ich versichere hiermit, dass ich die von mir eingereichte Abschlussarbeit selbstständig verfasst und keine anderen als die angegebenen Quellen und Hilfsmittel benutzt habe.

Ort, Datum, Unterschrift